nature portfolio

https://doi.org/10.1038/s41586-026-10656-8

Supplementary information

De novo design of miniproteins targeting GPCRs

In the format provided by the authors and unedited

De novo design of miniproteins targeting GPCRs

Edin Muratspahić[1,2,#], David Feldman[1,2,3#], David E. Kim[1,2,4,#], Xiangli Qu[1,2,#], Ana-Maria Bratovianu[3,5,#], Paula Rivera-Sánchez[3,5,#], Jan Hendrik Voss[5], Emil P. T. Hertz[5], Mads Jeppesen[5], Federica Dimitri[3], Kensuke Sakamoto[6,7], Amrita Nallathambi[5], Pia Peceli[5], Jianjun Cao[8,9], Brian P. Cary[8,9], Matthew J. Belousoff[8,9], Peter Keov[8,9], Phuc N.H. Trinh[8,9], Qingchao Chen[10], Yue Ren[10], Justyn Fine[11,12], Sudha Mishra[13], Annu Dalal[13], Shachie Sinha[13], Ramanuj Banerjee[13], Manisankar Ganguly[13], Karthik Varappalayam Karuppusamy[14], Isaac Sappington[1,2], Thomas Schlichthaerle[1,2], Jason Z. Zhang[1,2], Arvind Pillai[1,2], Brian Coventry[1,2], Ljubica Mihaljević[1,2,4], Magnus Bauer[1,2], Susana Vázquez Torres[1,2], Amir Motmaen[1,2], Gyu Rie Lee[1,2,4], Long Tran[2,15], Xinru Wang[1,2], Inna Goreshnik[1,2], Dionne K. Vafeados[1,2], Justin E. Svendsen[16,17], Parisa Hosseinzadeh[16,17], Nicolai Lindegaard[18], Matthäus Brandt[18], Yann Waltenspühl[18], Kristine Deibler[18], Lukas Deweid[18], Anja Bennett[18], Jendrik Schöppe[18], Tiantang Dong[19], Xiaoli Yan[19], Luke Oostdyk[20], William Cao[20], Lakshmi Anantharaman[20], Johan J. Weisser[21], Jesper Frank Bastlund[21], Christoffer Bundgaard[21], Ayodeji A. Asuni[21], Justin G. English[1,2], Lance Stewart[1,2], Lauren Halloran[12,22,23], Jamie B. Spangler[12,22,23], André Lieber[14], Arun K. Shukla[13], Patrick M. Sexton[8,9], Bryan L. Roth[6,7], Brian E. Krumm[6,7], Denise Wootten[8,9], Christopher G. Tate[10], Christoffer Norn[1,2,3,5*], David Baker[1,2,4]

[1]Department of Biochemistry, University of Washington, Seattle, WA 98195, USA.
[2]Institute for Protein Design, University of Washington, Seattle, WA 98195, USA.
[3]BioInnovation Institute, DK-2200 Copenhagen N, Denmark.
[4]Howard Hughes Medical Institute, University of Washington, Seattle, WA 98195, USA.
[5]Skape Bio ApS, DK-2200 Copenhagen N, Denmark.
[6]Department of Pharmacology, School of Medicine, University of North Carolina at Chapel Hill, Chapel Hill, NC, USA.
[7]NIMH Psychoactive Drug Screening Program, University of North Carolina at Chapel Hill, Chapel Hill, NC, USA.
[8]Drug Discovery Biology, Monash Institute of Pharmaceutical Sciences, Monash University, Parkville 3052, VIC, Australia.
[9]ARC Centre for Cryo-electron Microscopy of Membrane Proteins, Monash Institute of Pharmaceutical Sciences, Monash University, Parkville 3052, VIC, Australia.
[10]MRC Laboratory of Molecular Biology, Francis Crick Avenue, Cambridge, CB2 0QH, UK.
[11]Program in Molecular Biophysics, Johns Hopkins University, Baltimore, MD 21208, USA.
[12]Translational Tissue Engineering Center, Johns Hopkins University, Baltimore, MD 21231, USA.
[13]Department of Biological Sciences and Bioengineering, Indian Institute of Technology, Kanpur 208016, India.
[14]University of Washington, Department of Medicine, Division of Medical Genetics, Seattle, WA 98195, USA.
[15]Department of Chemical Engineering, University of Washington, Seattle, WA 98195, USA.
[16]Department of Bioengineering, Knight Campus for Accelerating Scientific Impact, University of Oregon, Eugene, OR 97403, USA.
[17]Department of Chemistry and Biochemistry, University of Oregon, Eugene, OR 97403, USA.
[18]Novo Nordisk A/S, Novo Nordisk Park 1, 2760 Måløv, Denmark.
[19]Novo Nordisk Research Centre China, Changping District, Beijing 102206, China.
[20]LeadHunter Services, Eurofins DiscoverX, LLC, Fremont, CA94583, USA.
[21]H. Lundbeck A/S, Global Research, 9 Ottiliavej DK-2500 Copenhagen-Valby, Denmark.
[22]Department of Chemical and Biomolecular Engineering, Johns Hopkins University, Baltimore, MD 21218, USA.
[23]Department of Biomedical Engineering, Johns Hopkins University, Baltimore, MD 21218, USA.

[#]These authors contributed equally.
*Correspondence: edinm2@uw.edu, chris.norn@skape.bio

This PDF file includes:
Supplementary Figs. 1 - 69
Supplementary Tables 1 – 11
References

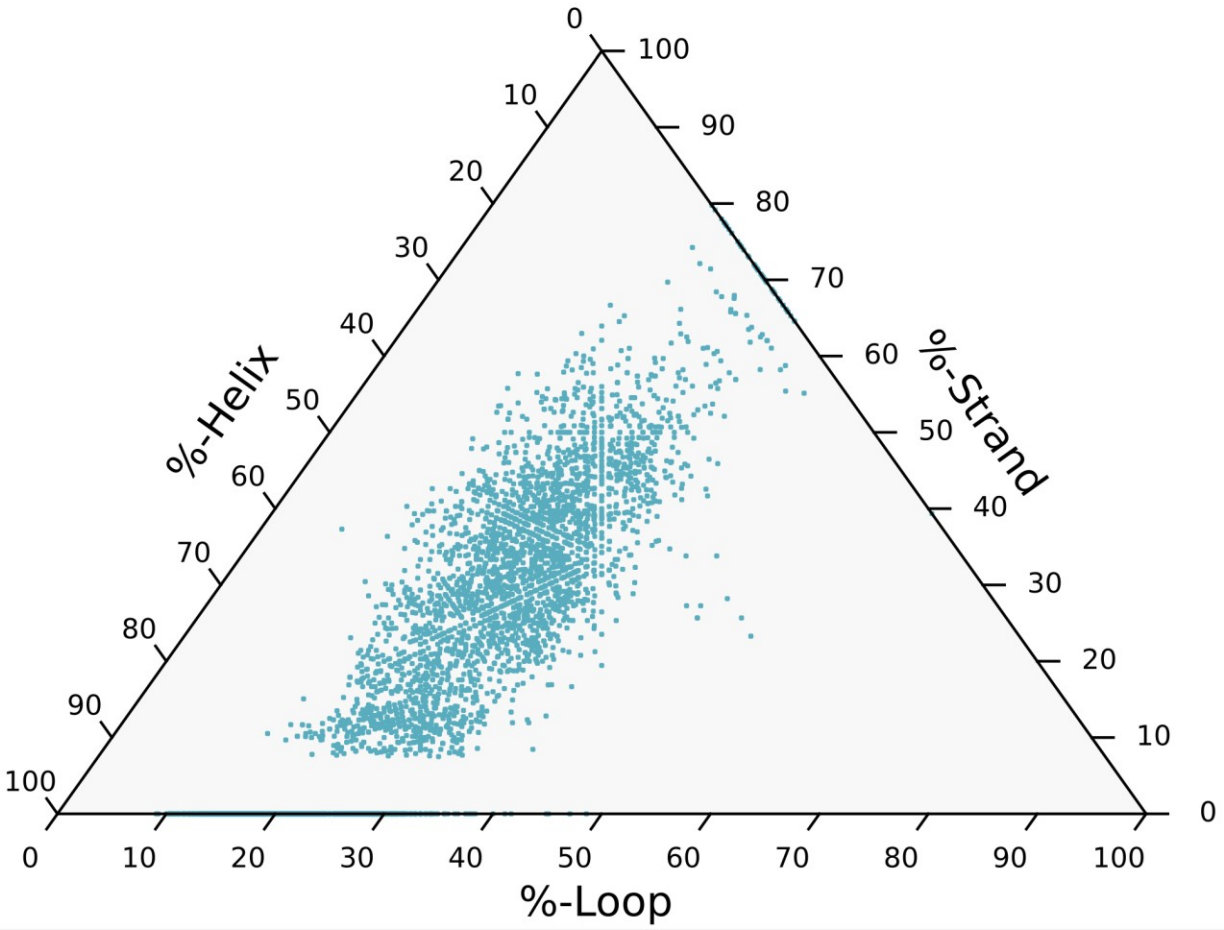

Supplementary Fig. 1. **Distribution of secondary structure content of metaproteome-derived miniprotein scaffold library.** The library is composed of diverse scaffolds comprising helices, loops and strands.

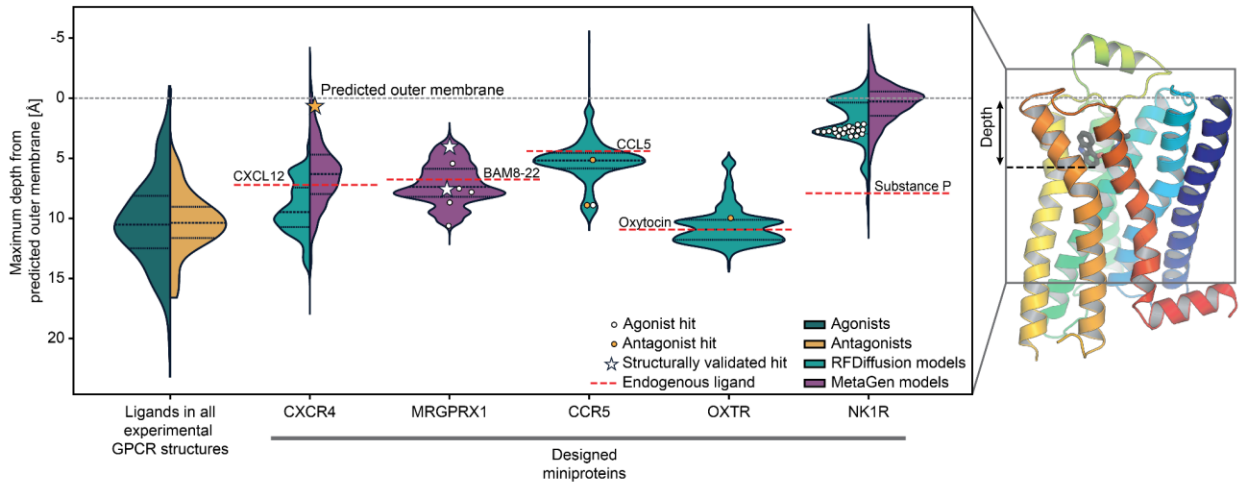

Supplementary Fig. 2. **Analysis of insertion depth of designs in orthosteric binding pocket of class A receptors.** Violin plots show the distribution of maximum depths reached by ligands and designs, measured as the deepest heavy atom (Å) relative to the predicted outer membrane boundary (OPM database). Depth is defined along the membrane normal, with larger values corresponding to deeper penetration into the receptor core (illustrated on right). Experimental receptor ligands include small molecules and peptides, while designs represent miniproteins targeting CXCR4, MRGPRX1, CCR5, OXTR, and NK1R. Colors distinguish agonists (dark green) and antagonists (gold) among receptor ligands, and RFdiffusion (cyan) versus MetaGen (purple) among designs. Identified experimental hits for miniprotein binders are shown as circles and structurally validated hits (by cryoEM) are shown as stars. Agonist stars and circles are colored white and antagonists are colored orange. Horizontal dotted lines within each violin indicate quartiles of the distributions. Red dashed lines show representative binding depths for known natural ligands (CXCL12, BAM (8-22), CCL5, oxytocin).

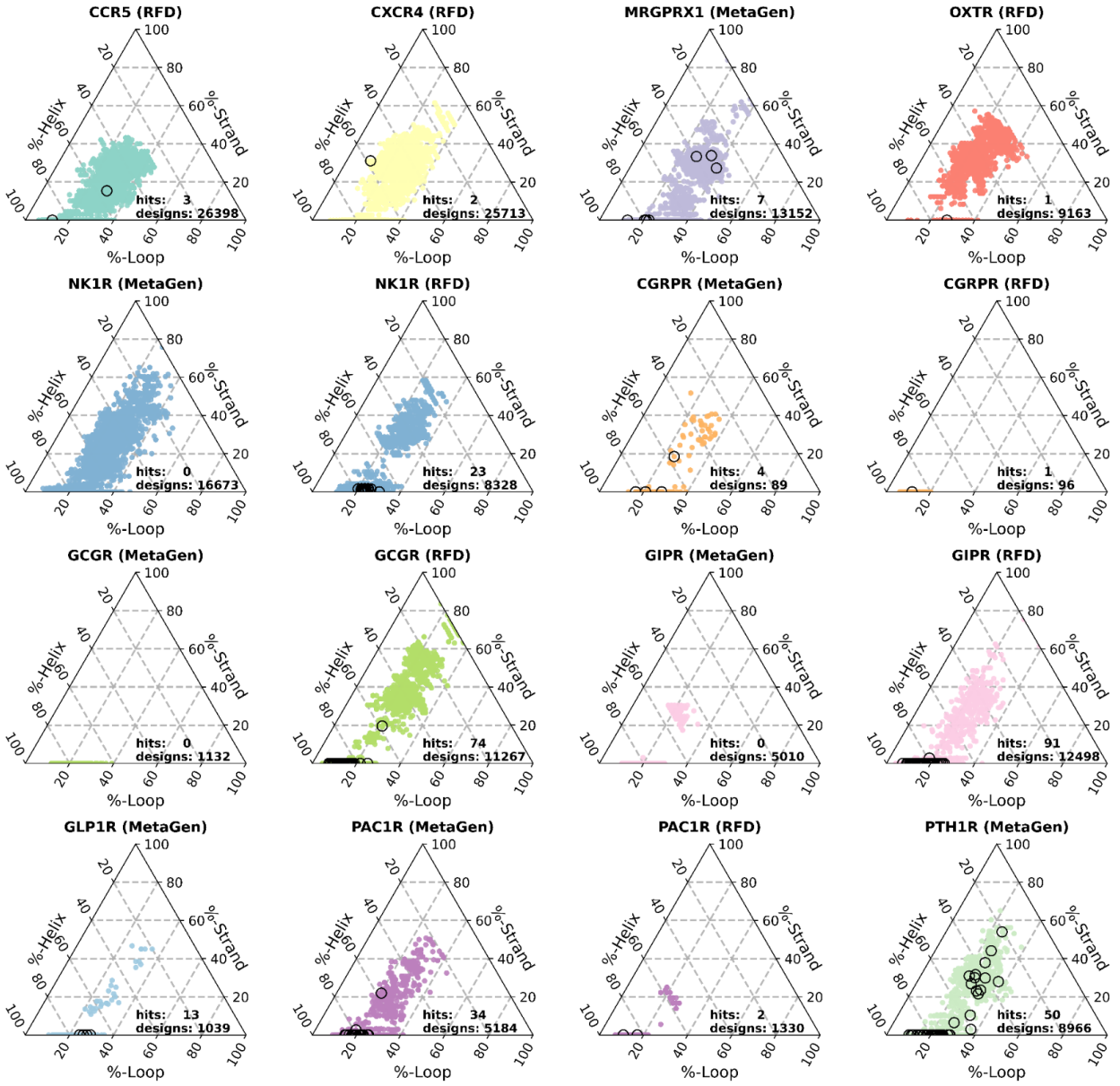

Supplementary Fig. 3. Structural topologies of designed miniproteins.
Ternary plots show the secondary-structure composition (% helix, % strand, % loop) of computationally designed miniproteins generated with MetaGen or RFdiffusion (RFD) Colored points represent designs selected for experimental testing, and black circles denote successful hits. Hit identification came from functional assays for CXCR4, CCR5, MRGPRX1, OXTR and CGRPR, from OPS-RD for PTH1R, and SPR for GIPR, GCGR, NK1R and PAC1R. The total number of designs in the ordered library and the resulting hits are indicated in each plot.

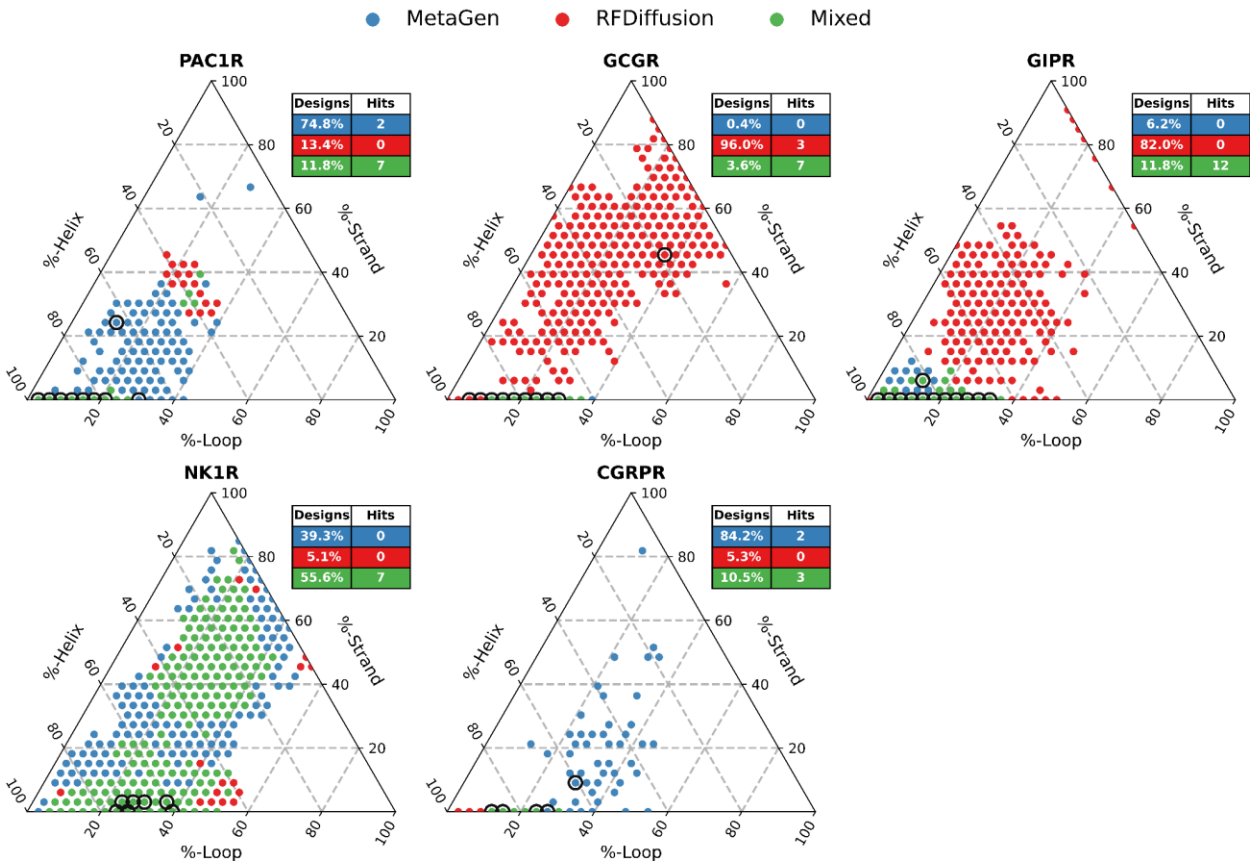

Supplementary Fig. 4. Interface topology coverage for RFdiffusion and MetaGen designs. For the six targets where both RFdiffusion and MetaGen design campaigns were performed (PAC1R, GCGR, GIPR, NK1R, and CGRPR), ternary plots show the binned secondary-structure composition of each design, expressed as percent helix, strand, and loop. Each point corresponds to one occupied bin in composition space, discretized on a 33×33×33 triangular grid. Bins populated exclusively by MetaGen designs are shown in blue, bins populated exclusively by RFdiffusion designs are shown in red, and bins containing designs from both methods are shown in green ("Mixed"). The inset table in each panel reports the percentage of occupied bins covered by MetaGen-only, RFdiffusion-only, or mixed designs, together with the number of bins containing at least one experimentally identified hit. Corresponding hits are indicated with black circles in the grid. Notably, experimentally identified hits are distributed across distinct regions of secondary-structure composition space, indicating that MetaGen and RFdiffusion not only differ in overall coverage but also generate successful binders with different interface topologies. Hits were defined as in **Supplementary Fig. 3**.

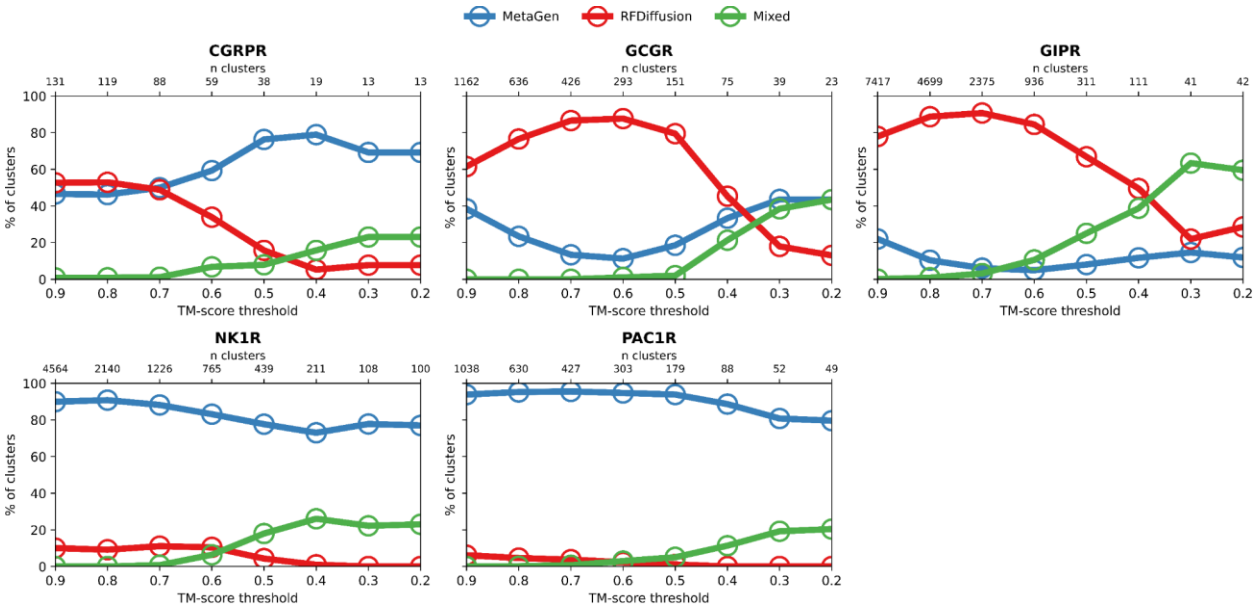

Supplementary Fig. 5. Structural space explored by MetaGen and RFdiffusion. For the six targets where both RFdiffusion and MetaGen design campaigns were performed (PAC1R, GCGR, GIPR, NK1R, and CGRPR)**,** the percentage of structural clusters composed exclusively of MetaGen designs (blue), exclusively of RFdiffusion designs (red), or containing a mixture of both methods (green) is shown as a function of the TM-score clustering threshold. Clustering was performed independently for each target protein using Foldseek[1]. Higher TM-score thresholds correspond to finer structural distinctions (more clusters), whereas lower thresholds merge increasingly diverse structures. The number of clusters at each threshold is shown above each panel. The progressive increase in mixed clusters at lower thresholds indicates convergence of MetaGen and RFdiffusion designs toward shared structural motifs as structural similarity criteria are relaxed; however, a substantial fraction of clusters remain method-specific, suggesting that MetaGen and RFdiffusion also explore distinct regions of structural space.

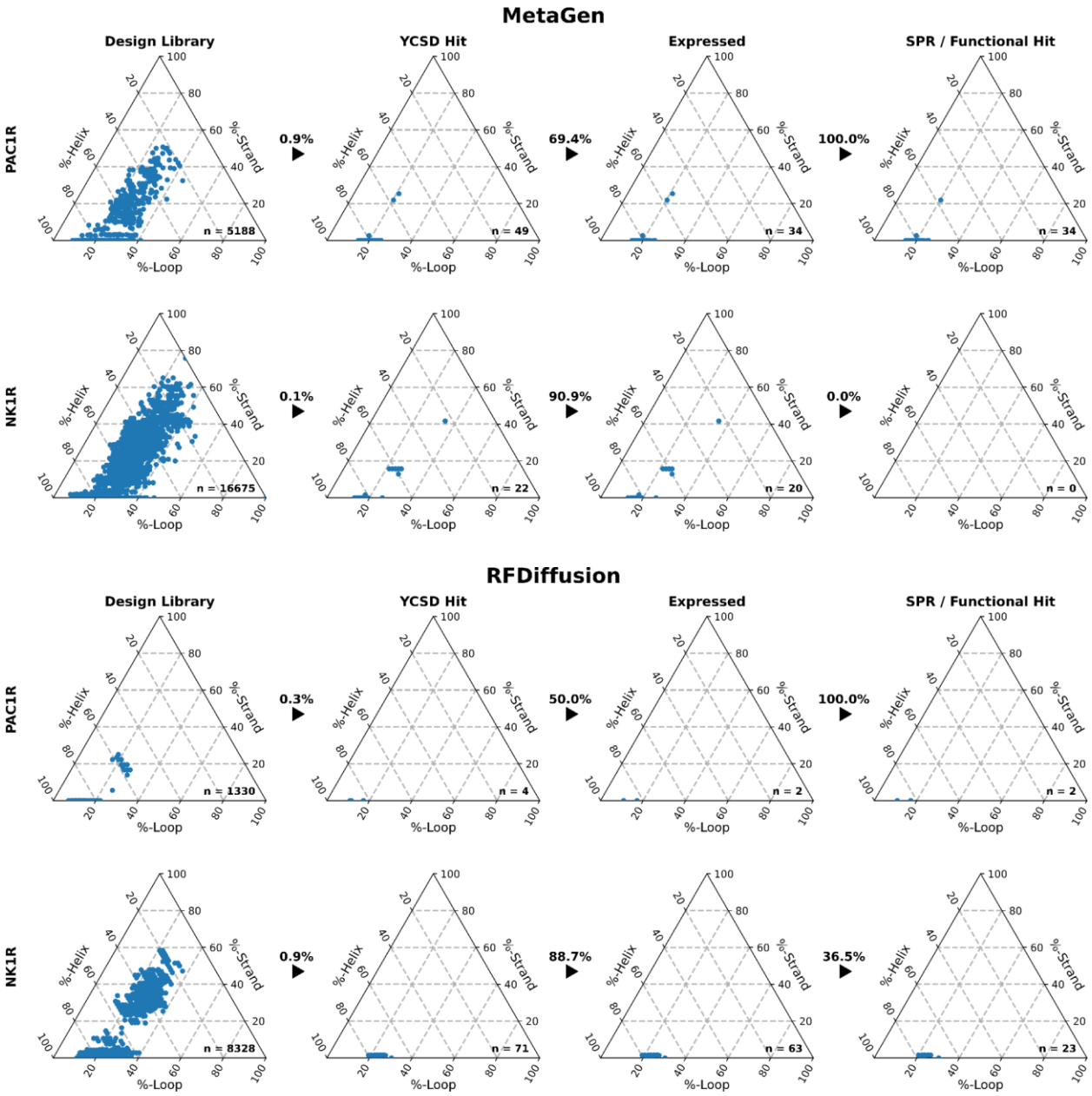

Supplementary Fig. 6. Comparison of experimental success rates for MetaGen- and RFdiffusion-designed miniproteins across matched campaigns.

MetaGen (top) and RFdiffusion (bottom) campaigns were compared across two targets (PAC1R and NK1R) under closely matched conditions. Rows correspond to targets, and columns to successive stages: full library, YCSD hits, expression, and downstream validation by SPR (PAC1R) or functional screening (NK1R). Ternary plots show secondary-structure composition (helix, strand, loop), with retained designs in blue; n indicates designs evaluated and arrows the fraction advanced. MetaGen showed higher yeast-display success and more successful PAC1R binders despite similar expression levels and SPR hit rates, whereas RFdiffusion outperformed MetaGen for NK1R and was the only method to yield functional hits, indicating the methods provide complementary strengths that broaden design diversity and increase the likelihood of identifying functional binders across targets.

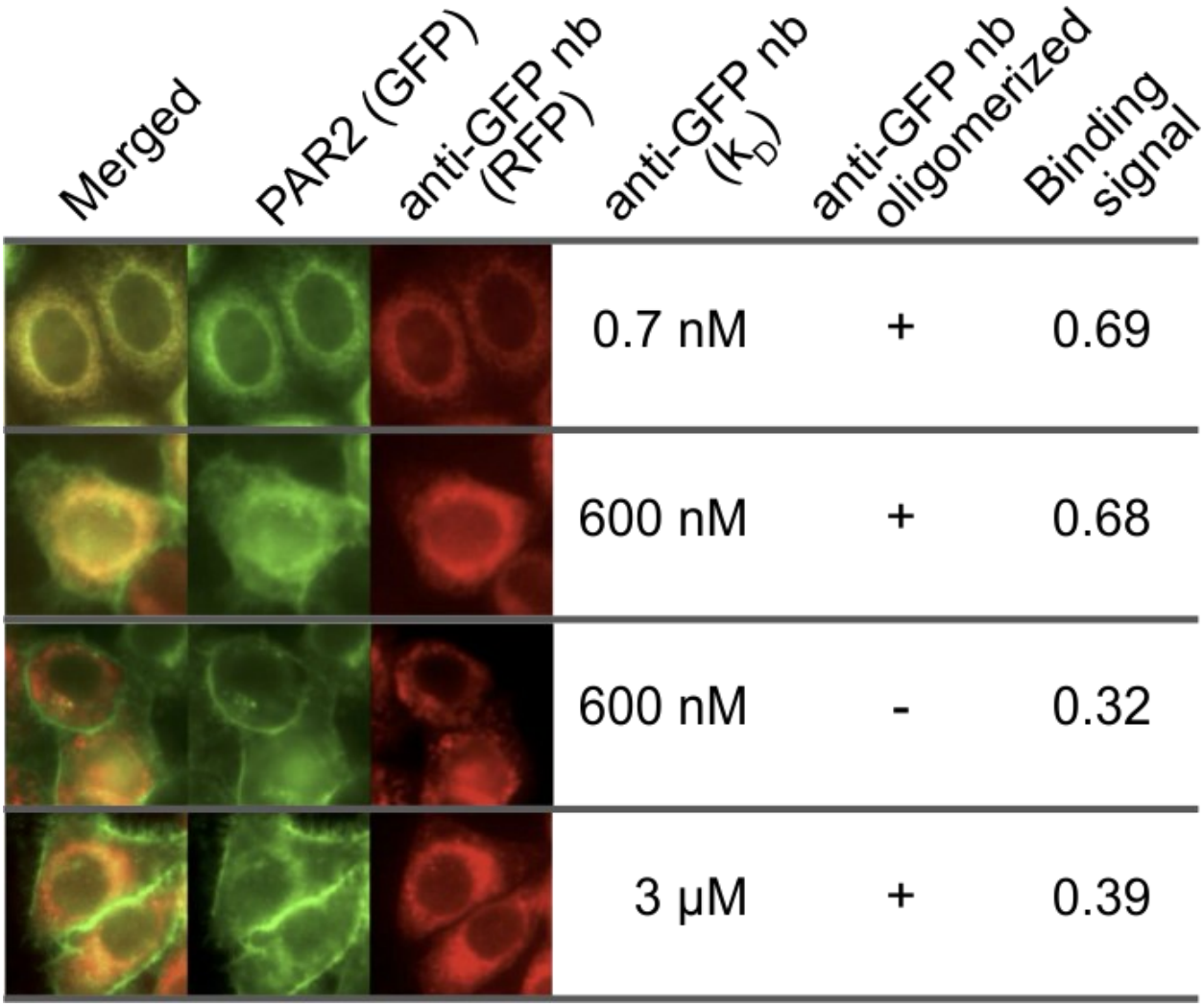

Supplementary Fig. 7. OPS-RD. Using nanobodies with known affinities targeting a GFP-fused protease-activated receptor 2 (PAR2), the binding signal (GFP-RFP pixel cross-correlation) is proportional with the binding affinity, can be enhanced using oligomerized binding constructs with increased avidity. Data are shown from a single experiment (n=1).

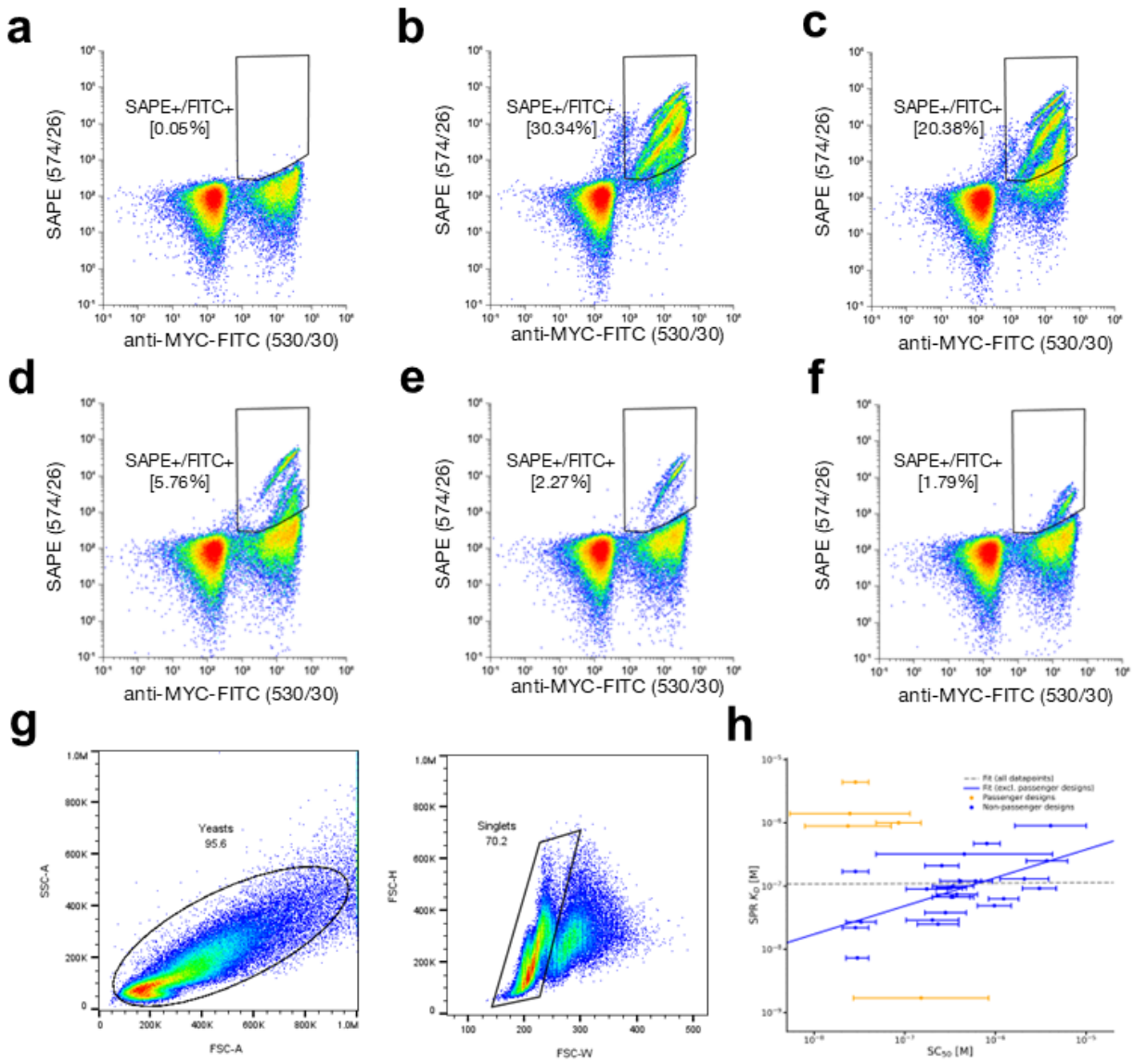

Supplementary Fig. 8. Yeast display of PAC1R binders using soluble ECD and data analysis. Representative flow cytometry plots of binders are shown. X-axis represents binder display and Y-axis target PAC1R binding. **a** Designed library of binders without the target PAC1R extracellular domain (ECD) represents a negative control. Yeast cells expressing binders on their surface were incubated with **b** 1 μM, **c** 100 nM, **d** 10 nM, **e** 1 nM or **f** 100 pM of PAC1R ECD. Data are shown from the fourth round of sorting. **g** Gating strategy; forward scatter (FSC-A) versus side scatter (SSC-A) plot with gate (black circle) was used for population identification. FSC-W versus FSC-H plot was applied to exclude doublets and isolate singlets. Negative control **a** was used to set a gate for measuring target binding **b-f**. **h** Identification and exclusion of passenger designs (yeast clones likely harboring multiple plasmids per cell) markedly improved agreement between yeast display–derived SC_{50} values and SPR K_D measurements, increasing the log-log Pearson correlation coefficient from 0.006 to 0.607. Each data point represents the yeast-derived SC_{50}, with horizontal bars indicating the 99.8% confidence intervals. Designs suspected to originate from passenger plasmids (low SC_{50}RE values) are highlighted separately and excluded from the correlation analysis.

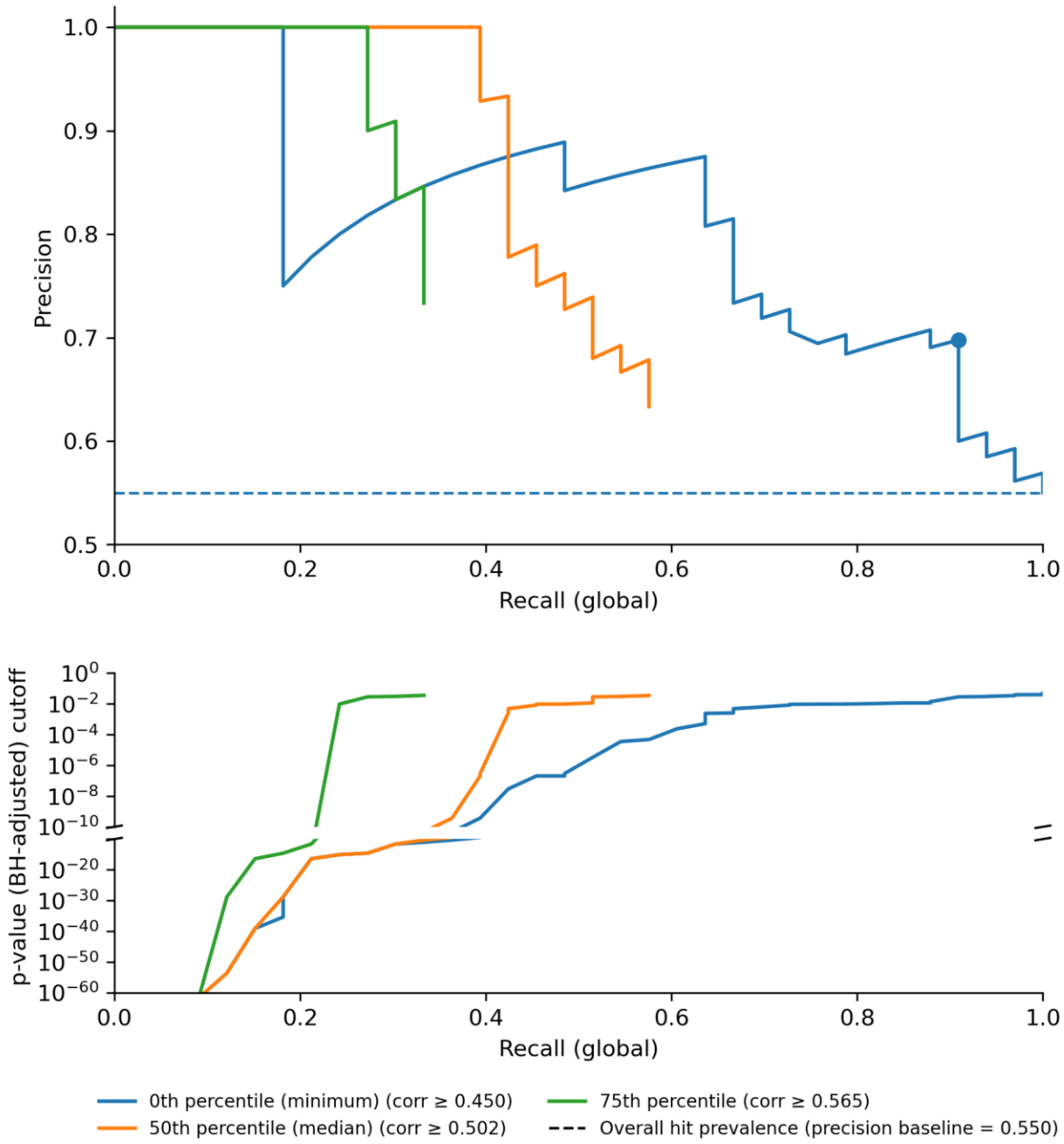

Supplementary Fig. 9. OPS-RD threshold tuning improves confirmation while trading off global recall.

Top, precision–recall curves for PAC1R binder designs using OPS-RD, where designs are ranked by BH-adjusted one-sided K–S p-value (derived from corr(GFP,RFP) distributions) and curves are shown for corr(GFP,RFP) thresholds at the 0th percentile (minimum, all designs), 50th percentile (median) and 75th percentile. Recall is reported as global recall (true positives recovered relative to the total number of SPR-confirmed binders in the evaluated set). The dashed line indicates the overall hit prevalence (precision baseline). The dot on the 0th-percentile curve marks the operating point that maximizes F1, corresponding to a BH-adjusted p-value cutoff of 0.014. Bottom, BH-adjusted p-value cutoff required to achieve a given

global recall for the same corr(GFP,RFP) thresholds. Detailed analysis is provided in the PAC1R dataset (Data availability).

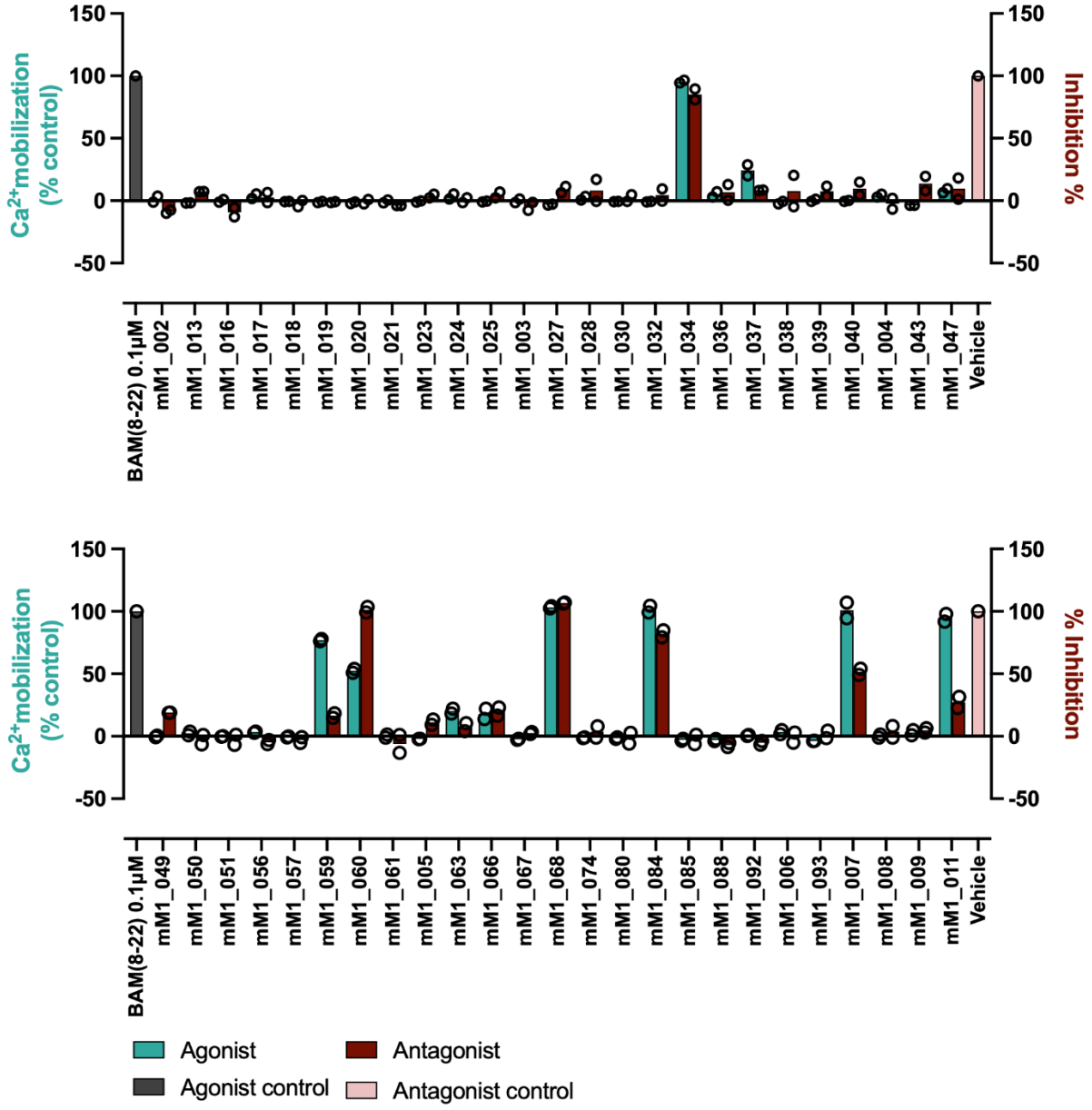

Supplementary Fig. 10. Calcium mobilization assay of binders at the MRGPRX1. The ability of binders designed by MetaGen approach to activate or inactivate the MRGPRX1 was examined in a calcium mobilization assay in agonist and antagonist mode. The native BAM 8-22 peptide served as agonist in both agonist and antagonist mode. Vehicle (buffer) served as agonist negative control and antagonist positive control. Binders that display both agonistic and antagonistic activity are false positive antagonists, due to desensitization of calcium channels in the assay. Data are shown as mean, n=2 technical replicates from a single experiment.

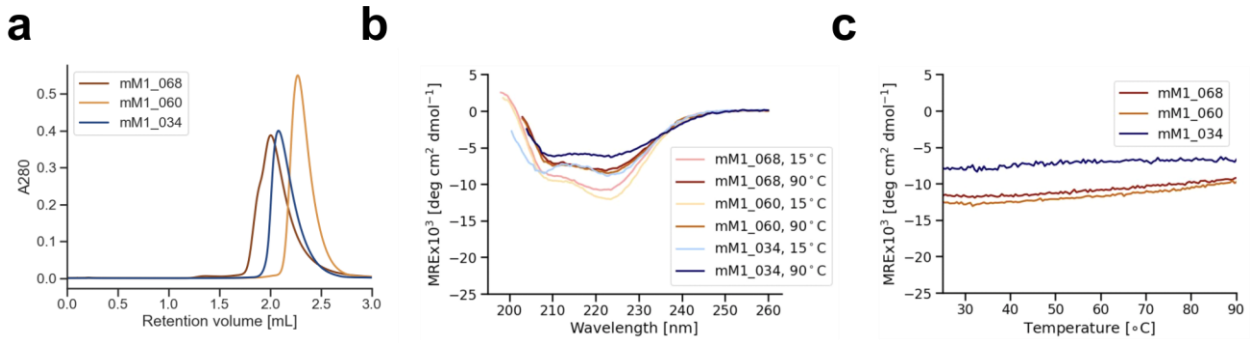

Supplementary Fig. 11. Biophysical characterization of MRGPRX1 binders. **a** Size-exclusion chromatography (SEC) traces, **b** circular dichroism (CD) spectra and **c** melting curves of MetaGen mM1_034, mM1_060 and mM1_064 binders targeting MRGPRX1.

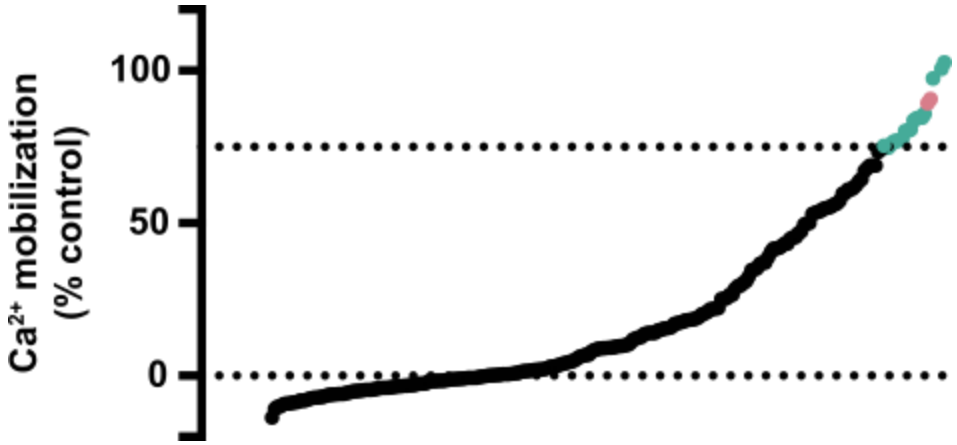

Supplementary Fig. 12. Agonist screen of optimized MRGPRX1 hits. Binders were optimized *via* structure-guided site saturation mutagenesis (SSM) and their ability to activate MRGPRX1 was evaluated in a calcium mobilization assay in CHO-K1 cells overexpressing MRGPRX1. Data were normalized to 100% = 1 µM BAM 8-22, 0% = buffer controls. Data are shown as mean, n=2 biological replicates.

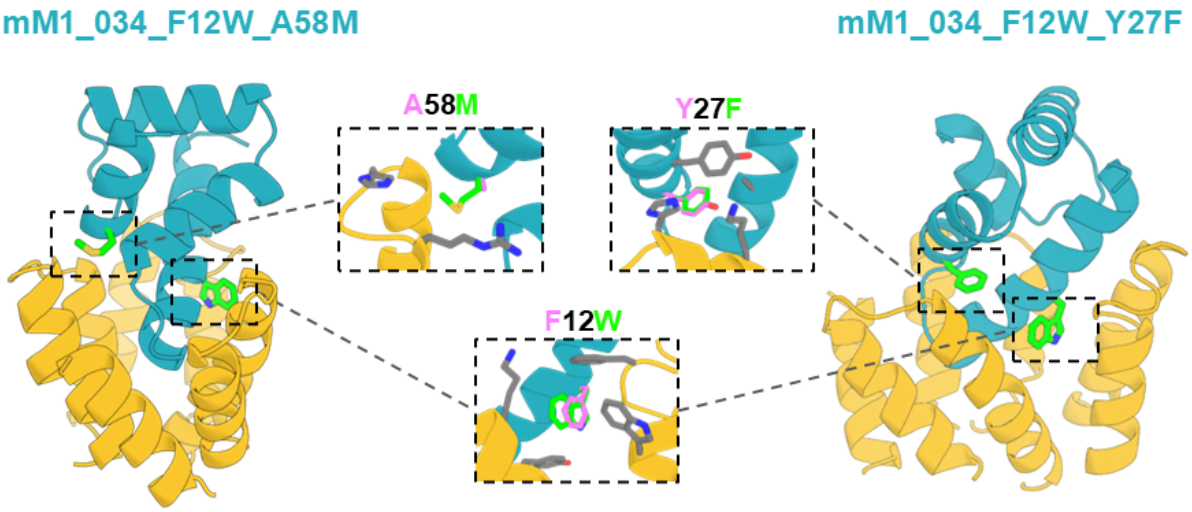

Supplementary Fig. 13. Computational models of optimized MRGPRX1 agonists. Computational design models of mM1_034_F12W_A58M and mM1_034_F12W_Y27F miniprotein agonists (blue) bound to the receptor (yellow). Mutations are highlighted in green. Mutations of F at the position 12 by Y as well as mutations of A at the position 58 by M and of Y at the position 27 by F led to significant improvement of the binder potency compared to the parent miniprotein mM1_034.

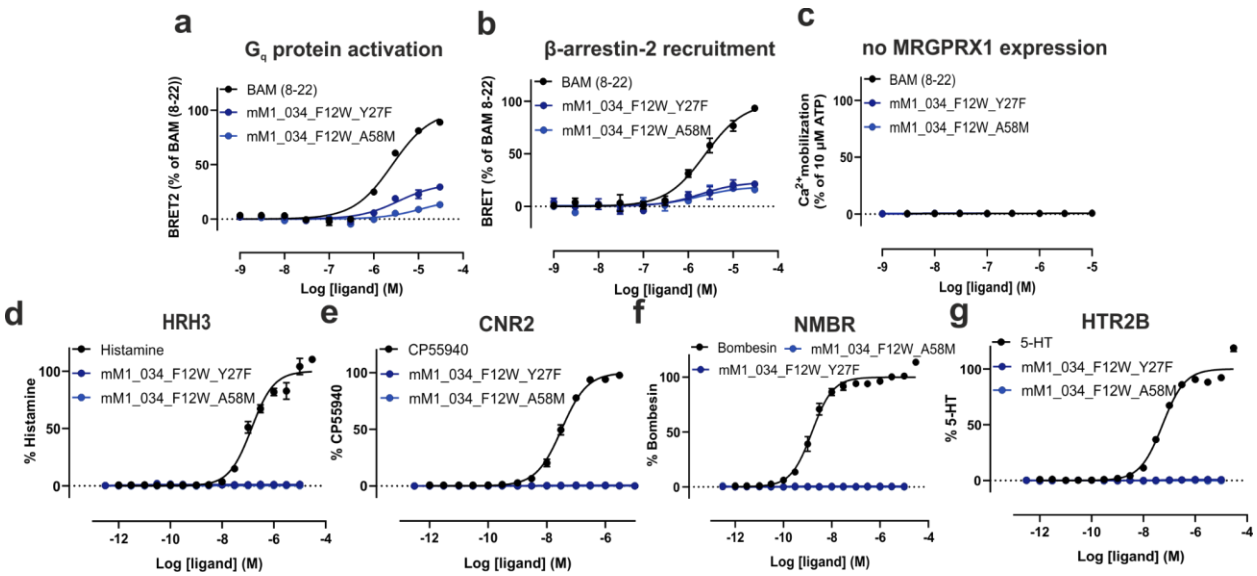

Supplementary Fig. 14. Pharmacology of improved MRGPRX1 agonists. a The ability of potency-improved agonists mM1_034_F12W_Y27F and mM1_034_F12_A58M to activate MRGPRX1 was evaluated in **a** G_q-protein and **b** β-arrestin 2 recruitment assays. The EC_{50} values of mM1_034_F12W_Y27F and mM1_034_F12_A58M were 4.2 ± 1.3 μM and 20 ± 11 μM in a G_q-protein assay and 1.8 ± 0.3 μM and 1.3 ± 0.9 μM in a β-arrestin-2 recruitment assay, respectively. Data are shown as mean ± s.e.m., n=3 biological replicates. **c** Calcium mobilization assay to confirm MRGPRX1-dependent effects of miniproteins. Miniproteins do not cause calcium mobilization in CHO cells without MRGPRX1. Data are shown as mean and are normalized to 10 μM of ATP (n=2, biological replicates). The BRET assays probe unamplified, proximal signaling events and therefore provide a more accurate measure of potency and intrinsic efficacy. The weaker potency and efficacy observed in BRET assays for miniproteins do not contradict the calcium results; instead, they reflect expected pharmacology for agonists at G_q protein-coupled coupled receptors such as MRGPRX1. These findings are in line with previous studies reporting similar pharmacological profiles of agonists at other GPCRs[2-4]. Follow-up selectivity experiments of mM1_034_F12W_Y27F and mM1_034_F12_A58M against hit receptors in the 320-GPCR selectivity screen, **d** H3R, **e** CNR2, **f** NMBR and **g** HTR2B. The EC_{50} values of the reference agonists were as follows: H3R - histamine - 176 ± 28 nM, CNR2 - CP55940 - 30.8 ± 3.8 nM, NMBR - Bombesin - 1.64 ± 0.44 nM, HTR2B - 5-HT - 54.2 ± 0.1 nM. Data are shown as mean ± s.e.m., n=3 biological replicates.

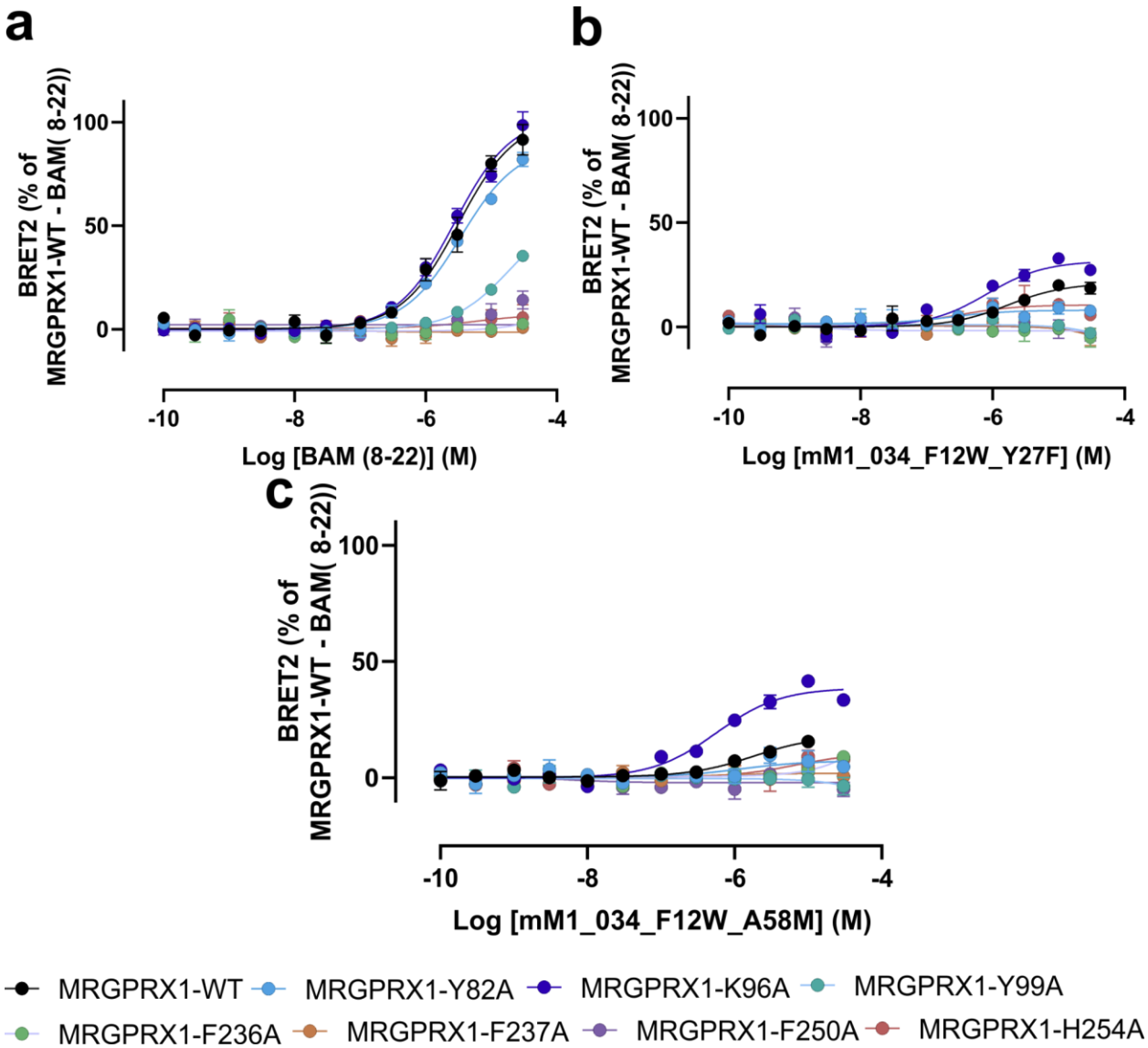

Supplementary Fig. 15. MRGPRX1 mutagenesis. Key MRGPRX1 residues critical for activity of BAM (8-22) and miniproteins were mutated to alanine and the ability of ligands to stimulate receptor signaling was measured in a TRUPATH assay. Data are mean ± s.e.m., n=3 biological replicates.

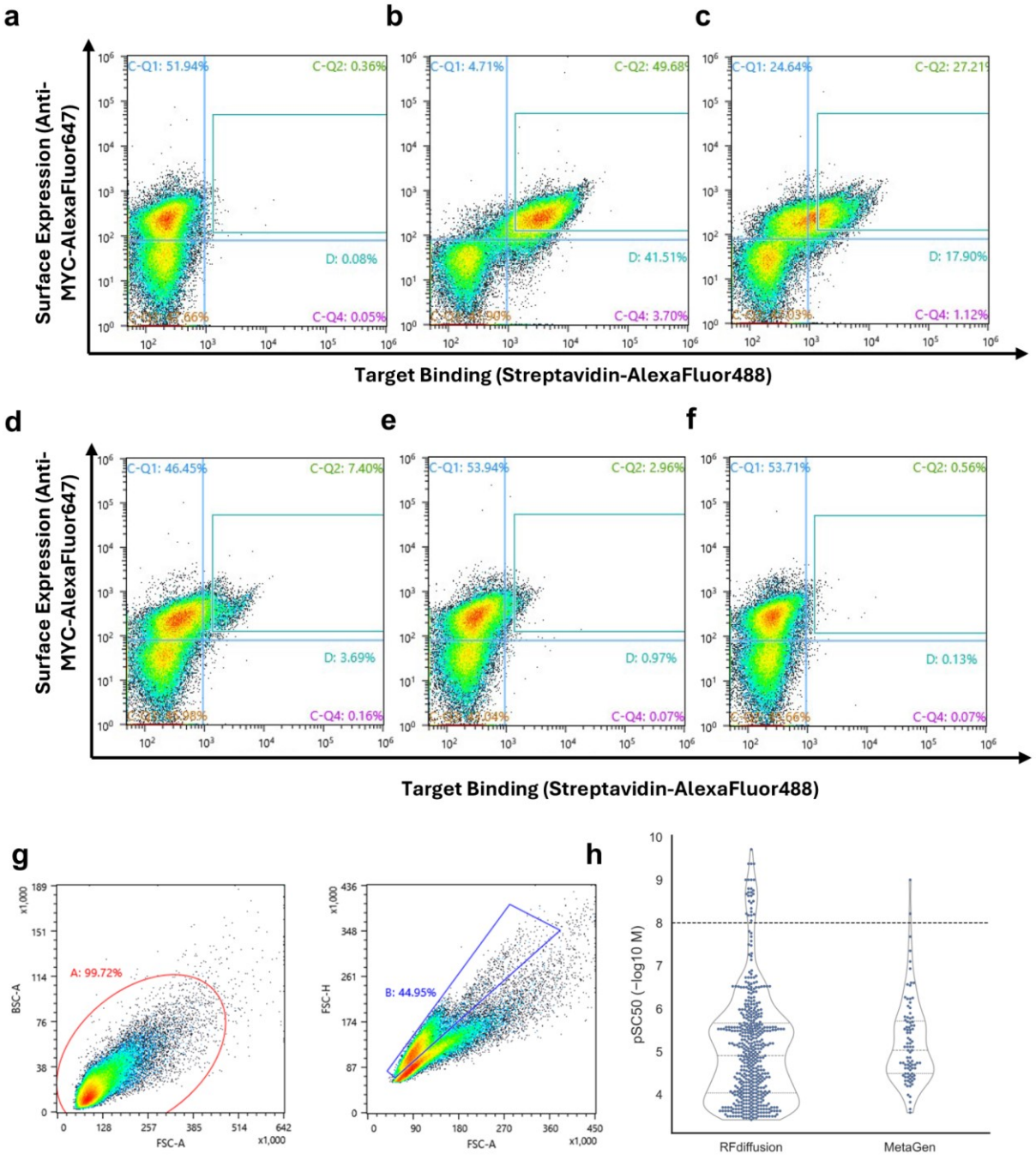

Supplementary Fig. 16. Yeast display of RFdiffusion and MetaGen binders using soluble NK1R in detergents. Representative flow cytometry plots of binders are shown. X-axis represents binder display and Y-axis target NK1R binding. **a** Designed library of binders without the soluble target NK1R represents a negative control. Yeast cells expressing binders on their surface were incubated with **b** 1000 nM, **c** 100 nM, **d** 10 nM, **e** 1 nM and **f** 0.1 nM of detergent-stabilized NK1R. Data are shown from the fourth round of sorting. **g** Gating strategy; forward scatter (FSC-A) versus side scatter (BSC-A) plot with gate (red circle) was used for population identification. FSC-H versus FSC-A plot was applied to exclude doublets and isolate singlets. Negative control **a** was used to set a gate for measuring target binding **b-f**. **h** Distribution of yeast display-derived pSC_{50} values across pooled NK1R designs by strategy. pSC_{50} values were

computed from SC_{50} measurements obtained by yeast display (−log10 M), and the dotted horizontal line corresponds to 10 nM (pSC50 = 8).

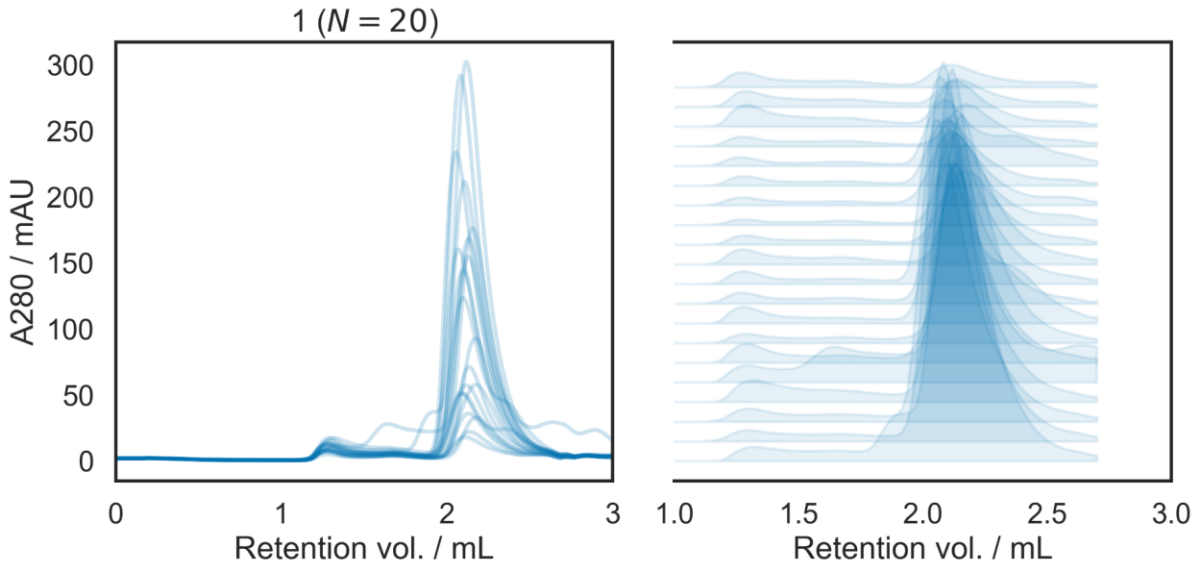

Supplementary Fig. 17. Biophysical characteristics of RFdiffusion-designed NK1R agonists. Size-exclusion chromatography (SEC) traces of RFdiffusion-designed NK1R agonists.

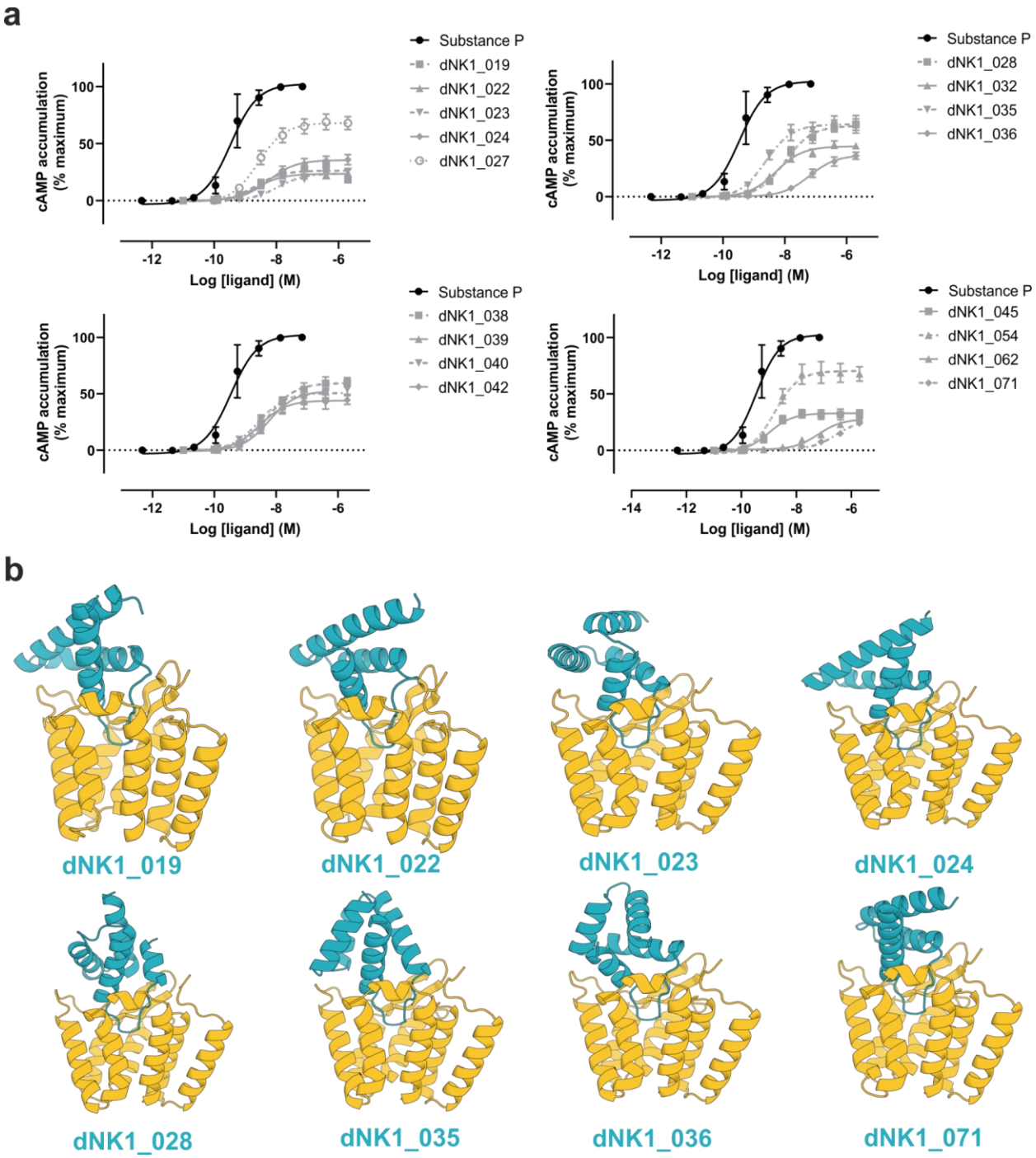

Supplementary Fig. 18. Backbone diversity of RFdiffusion-designed NK1R miniprotein agonists and pharmacological characterization. a Agonistic activity of RFdiffusion-designed miniproteins was measured using a cAMP assay in CHO cells stably expressing NK1R. Substance P served as a positive control. Data are shown as mean ± s.e.m., n=3 biological replicates, except for dNK1_071, mean, n=2 biological replicates. **b** Computational design models of agonists (blue) bound to NK1R (yellow, PDB ID: 7P02).

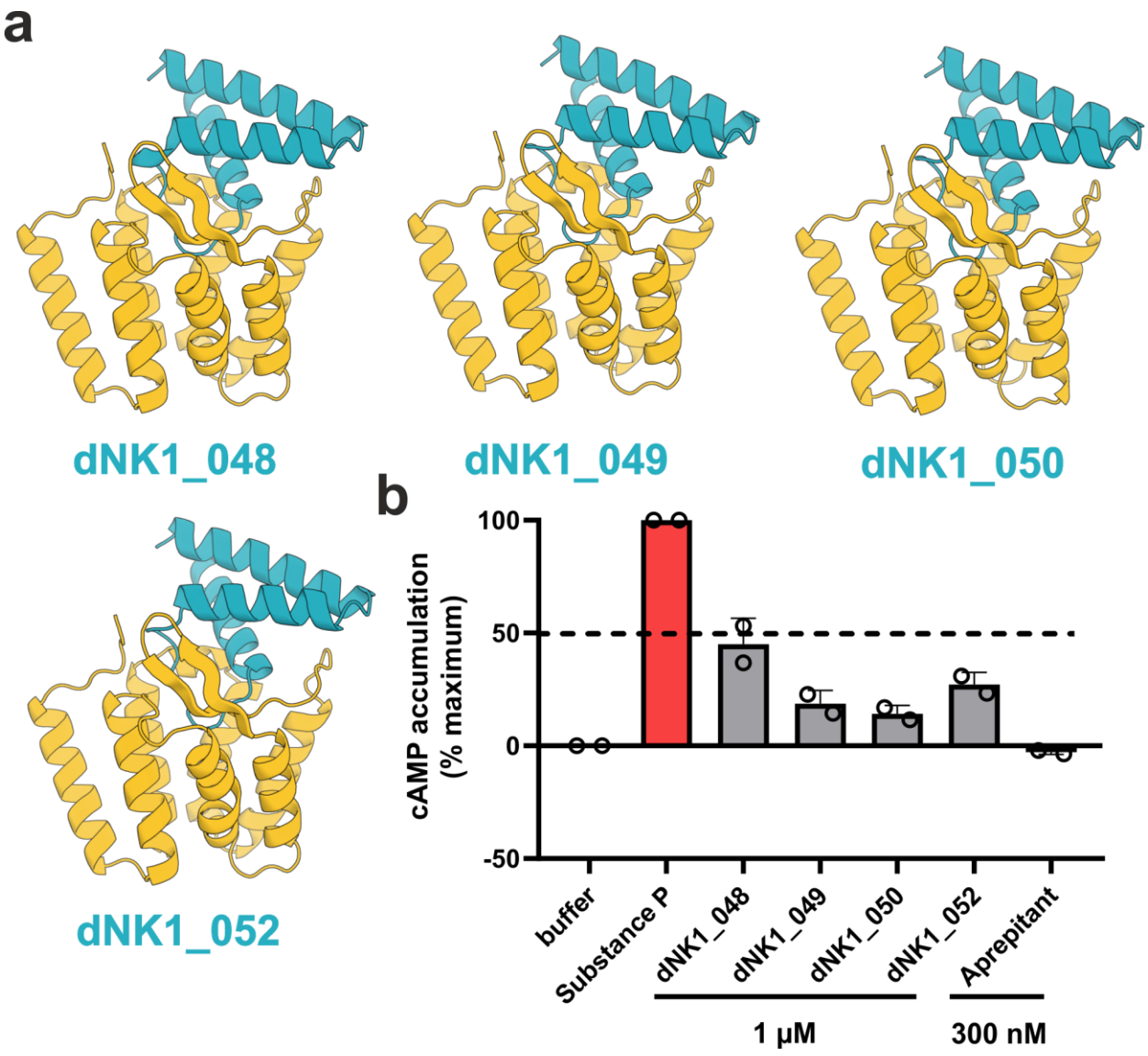

Supplementary Fig. 19. Backbone diversity of RFdiffusion-designed NK1R miniprotein antagonists and pharmacological characterization. a Computational design models of antagonists (blue) bound to NK1R (yellow, PDB ID: 7P02). Miniprotein antagonists share the same backbone yet distinct sequences. **b** Antagonistic activity of RFdiffusion-designed miniproteins was measured using a cAMP assay in CHO cells stably expressing NK1R. Aprepitant served as positive control. Data are shown as mean, n=2 biological replicates.

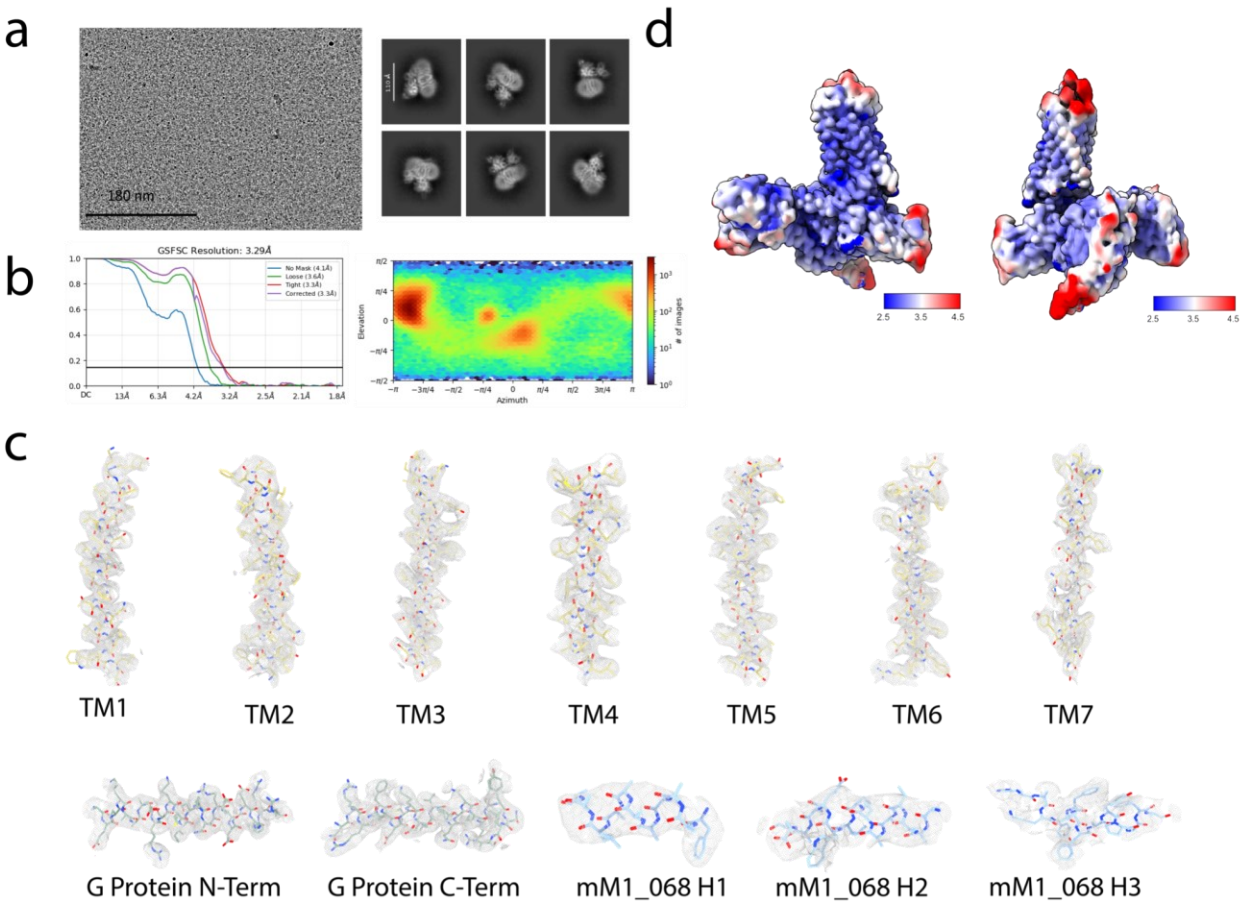

Supplementary Fig. 20. Cryo-EM analysis for MRGPRX1:MiniG$_q$:b1g2 bound to mM1_068. a Select motion corrected cryo-EM micrograph MRGPRX1:MiniG$_q$:b1g2:mM1_068 particles imaged at a nominal magnification of 45,000 and select two-dimensional class averages. **b** 2D plot of the gold standard Fourier shell correlation (GSFSC) and orientational distribution heat map obtained during refinement using Cryosparc. **c** Local cryo-EM density maps of TM1-7, G protein and mM1_068. **d** Local resolution heat-map was calculated using the Local Resolution Estimation within Cryosparc.

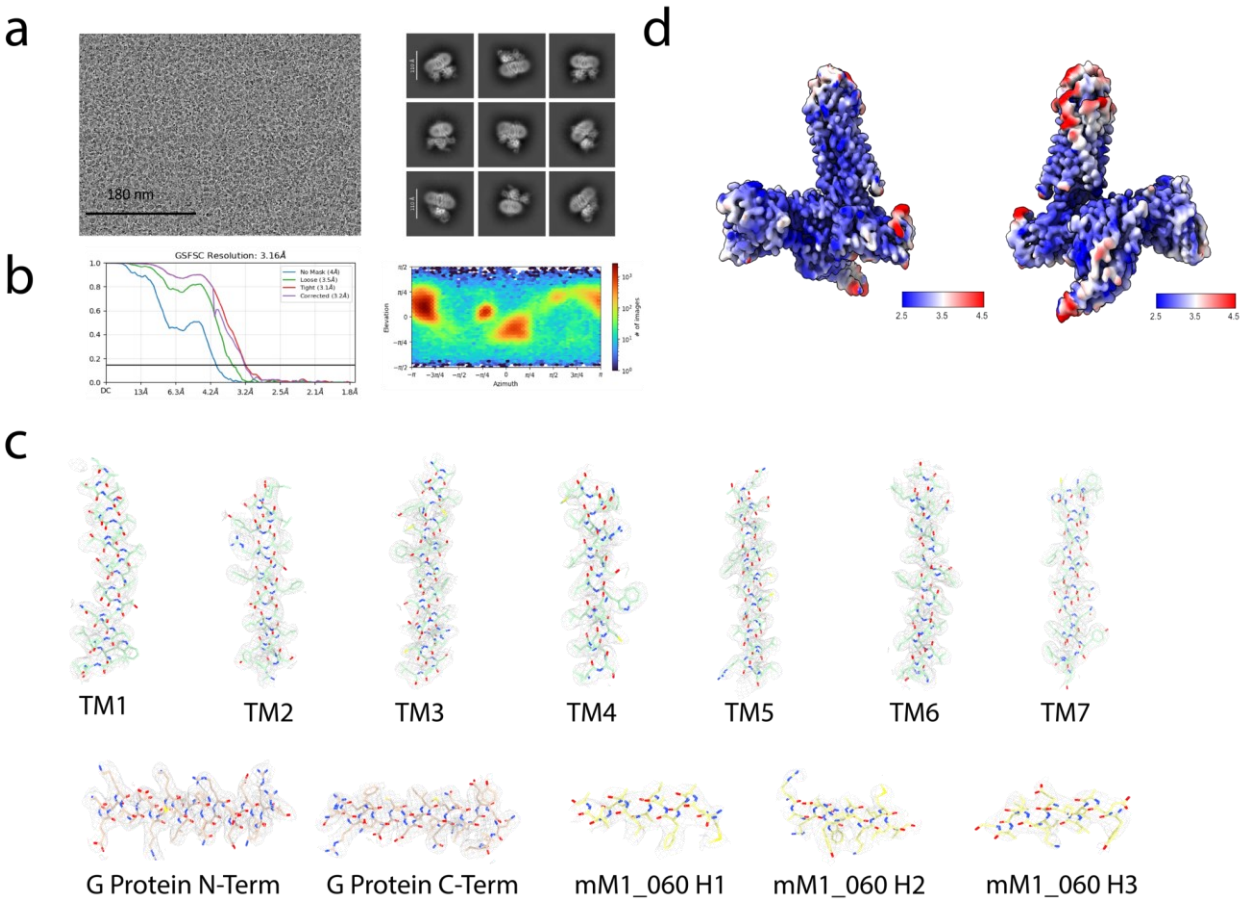

Supplementary Fig. 21. Cryo-EM analysis for hMRGPRX1:MiniG_q:b1g2 bound to mM1_060. a Select motion corrected cryo-EM micrograph hMRGPRX1:MiniG_q:b1g2:mM1_060 particles imaged at a nominal magnification of 45,000 and select two-dimensional class averages. **b** 2D plot of the gold standard Fourier shell correlation (GSFSC) and orientational distribution heat map obtained during refinement using Cryosparc. **c** Local cryo-EM density maps of TM1-7, G protein and mM1_068. **d** Local resolution heat-map was calculated using the Local Resolution Estimation within Cryosparc.

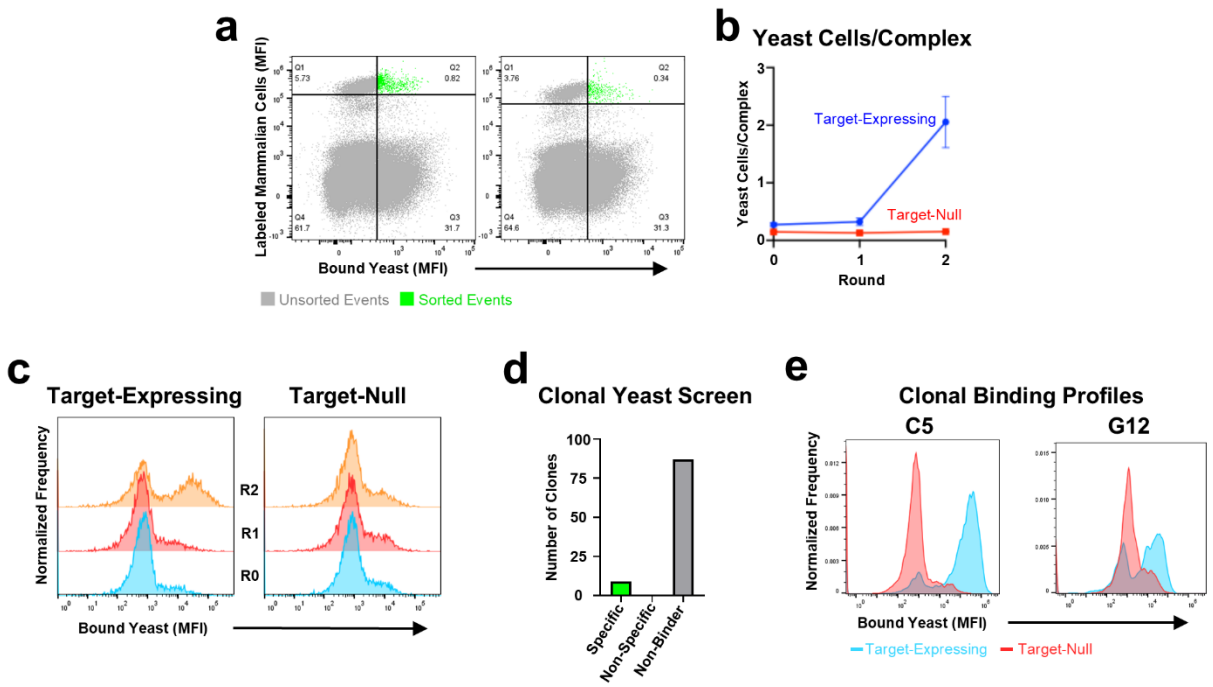

Supplementary Fig. 22. Hybrid adherent/suspension cell-based selection for the discovery of protein binders against CXCR4.

a Gating strategy to select for target-specific yeast clones. Sorted events are highlighted in green, with flow cytometry plots from round 1 (left) and 2 (right) shown. The x-axis depicts bound yeast (as measured by c-myc tag detection) and the y-axis depicts labeled mammalian cells (as measured by CellTraceTM dye detection). Sorting gates were selected based on double positive events. **b** Yeast cells/complex metric of yeast populations at each round of selection. Yeast cells/complex represents enrichment following incubation with either CXCR4+ (target-expressing, blue) or CXCR4- (target-null, red) HEK293T cells. **c** Flow cytometry histograms of the results shown in **b**, depicting yeast binding within the mammalian cell population to target-expressing or target-null cells. **d** Quantification of the results shown in **b**. 96 selected clones after two rounds of biofloating selection. Clones were classified as specific, non-specific, or non-binder representing miniproteins bound to target-expressing cells only, both target-expressing and target-null cells, or neither, respectively. Among the specific clones, there were two unique sequences, dCX_001, which was represented eight times, and dCX_003, which was represented once. **e** Clonal binding profiles for the two unique target-specific clones that were isolated from the library.

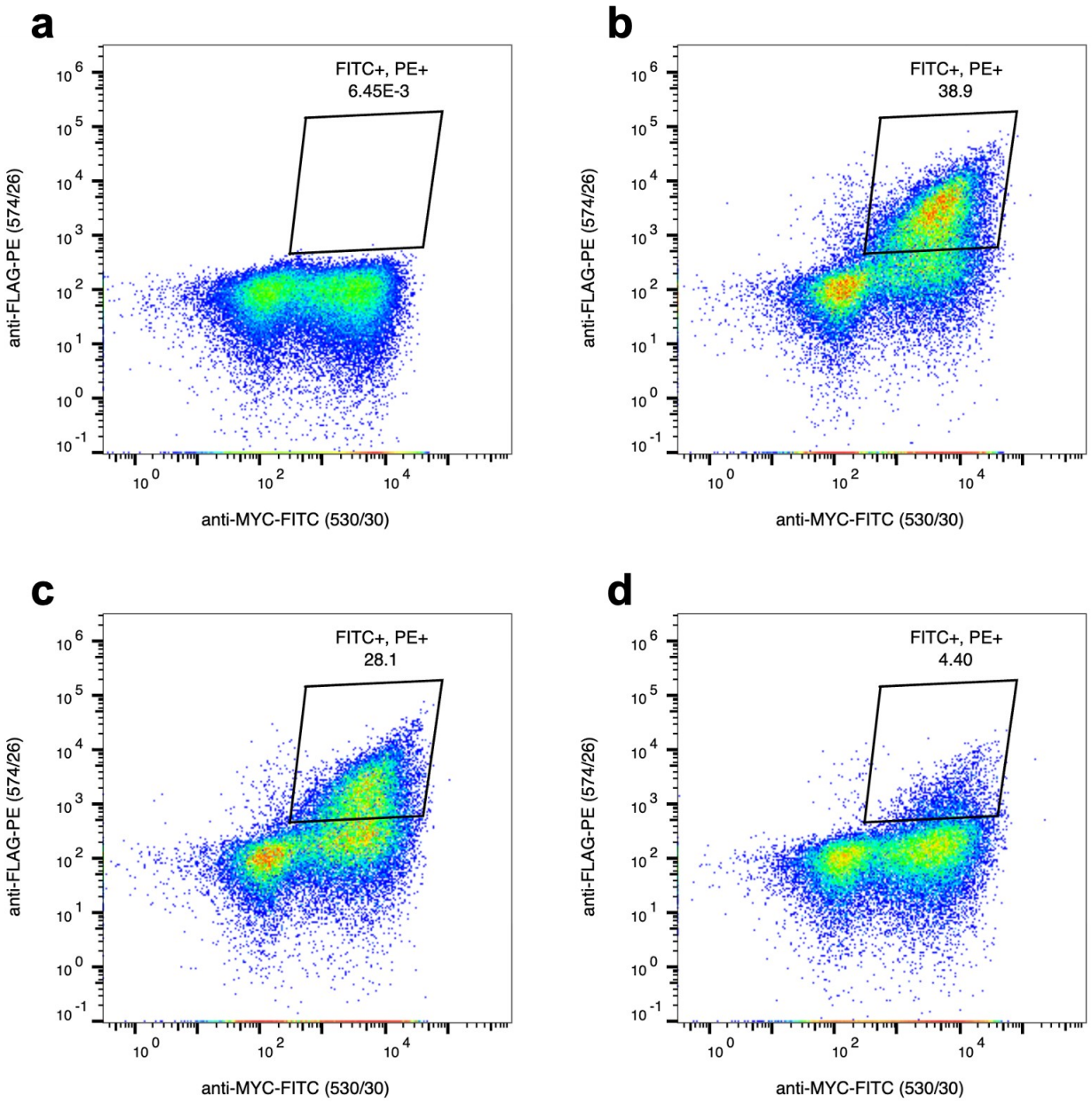

Supplementary Fig. 23. Yeast display of binders using CXCR4 nanodisc. Representative flow cytometry plots of binders are shown. X-axis represents binder display and Y-axis target CXCR4 binding. **a** Designed library of binders without the target CXCR4 nanodisc represents a negative control. Yeast cells expressing binders on their surface were incubated with **b** 100 nM **c** 10 nM or **d** 1 nM of CXCR4 nanodisc. Data are shown from the third round of sorting. Gating strategy described in **Supplementary Fig. 8g** was used to measure target binding **b-d**.

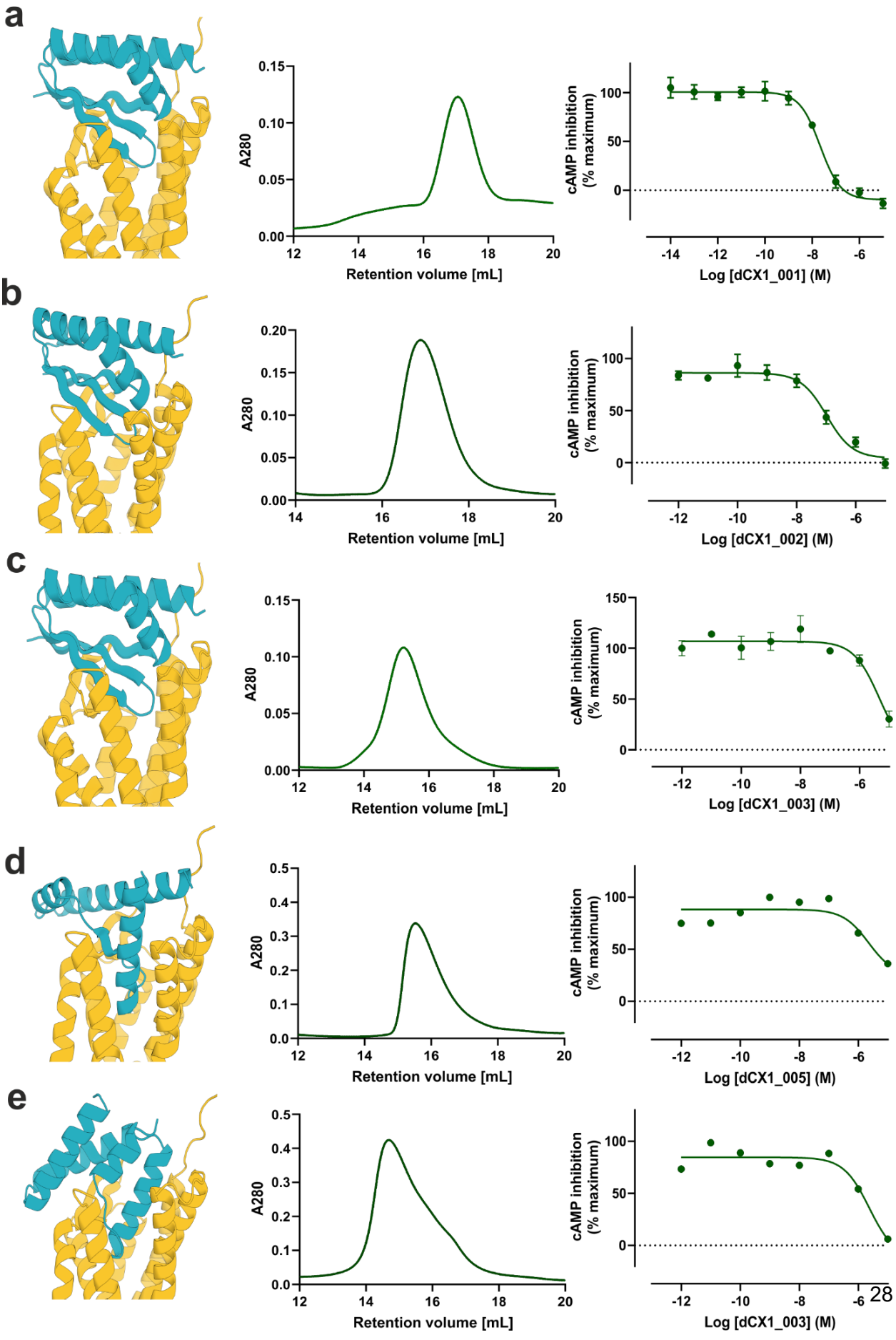
a
b
c
d
e
A280
Retention volume [mL]
cAMP inhibition (% maximum)
Log [dCX1_001] (M)
Log [dCX1_002] (M)
Log [dCX1_003] (M)
Log [dCX1_005] (M)

Supplementary Fig. 24. Characterization of CXCR4 binders identified by yeast display and nanodisc-stabilized CXCR4. Computational design models (blue) bound to the CXCR4 (yellow, PDB ID: 4RWS), size-exclusion chromatography (SEC) traces (middle) and concentration-response curves to derive IC_{50} values of **a** dCX1_001, **b** dCX1_002, **c** dCX1_003, **d** dCX1_004 and **e** dCX1_005 antagonists. Concentration-response curves were obtained in a cAMP assay in CHO cells stably expressing CXCR4. Data are shown as mean ± s.e.m. for dCX1_001 (n=4, biological replicates), dCX1_002 (n=3, biological replicates) and dCX1_003 (n=4, biological replicates) and mean for dCX1_004 (n=2, biological replicates) and dCX1_005 (n=2, biological replicates). The IC_{50} values for dCX1_001 and dCX1_002 were 24 ± 5 nM and 120 ± 30 nM, respectively, whereas IC_{50} values for dCX1_003, dCX1_004 and dCX1_005 were in the micromolar range.

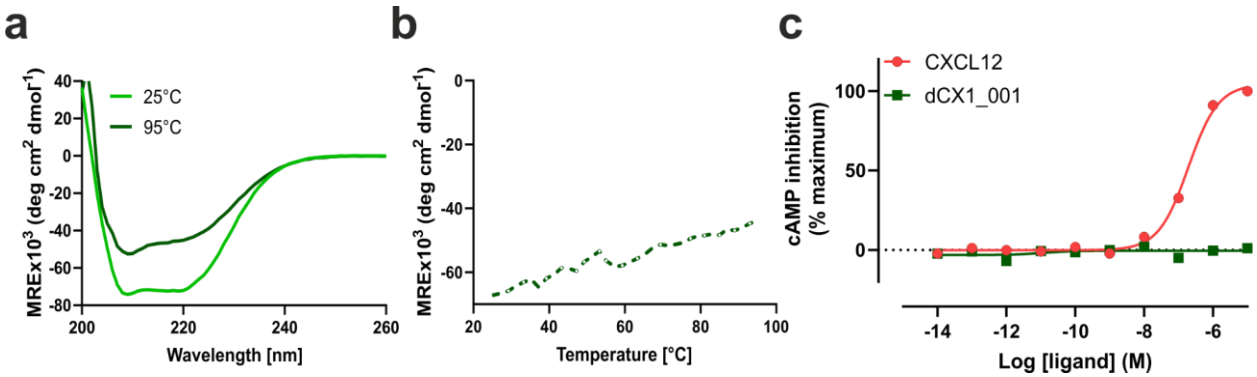

Supplementary Fig. 25. Biophysical characterization and pharmacology of the dCX1_001 miniprotein. a Circular dichroism (CD) spectra and **b** melting curves of the dCX1_001 binder. **c** dCX1_001 binder exhibited no agonistic activity in a cAMP assay using CHO cells stably expressing CXCR4 (mean, n=2 biological replicates).

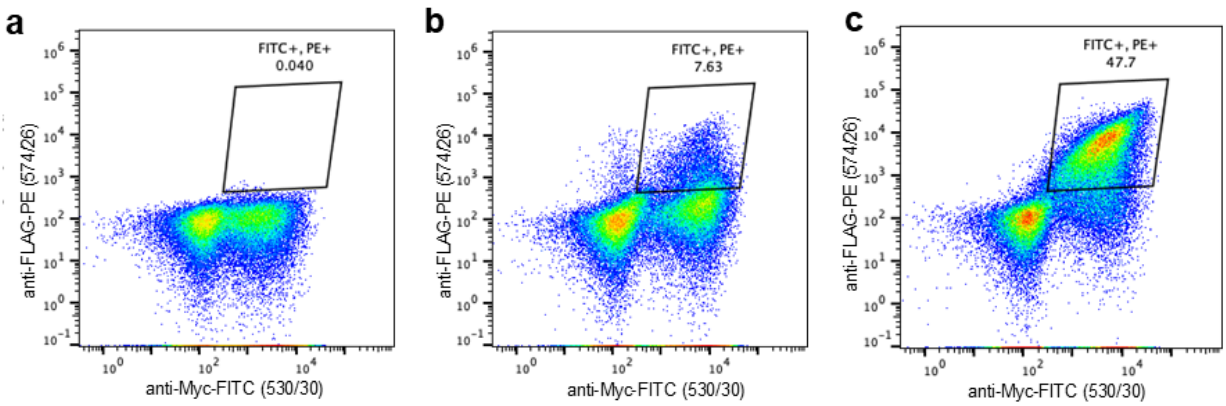

Supplementary Fig. 26. Yeast display of binders using CCR5 nanodisc. Representative flow cytometry plots of binders are shown. X-axis represents binder display and y-axis target CCR5 binding. **a** Designed library of binders without the target CCR5 nanodisc represents a negative control. Yeast cells expressing binders on their surface were incubated with **b** 500 nM (sort 1) or **c** 500 nM (sort 3). Gating strategy described in **Supplementary Fig. 8g** was used to measure target binding **b-c**.

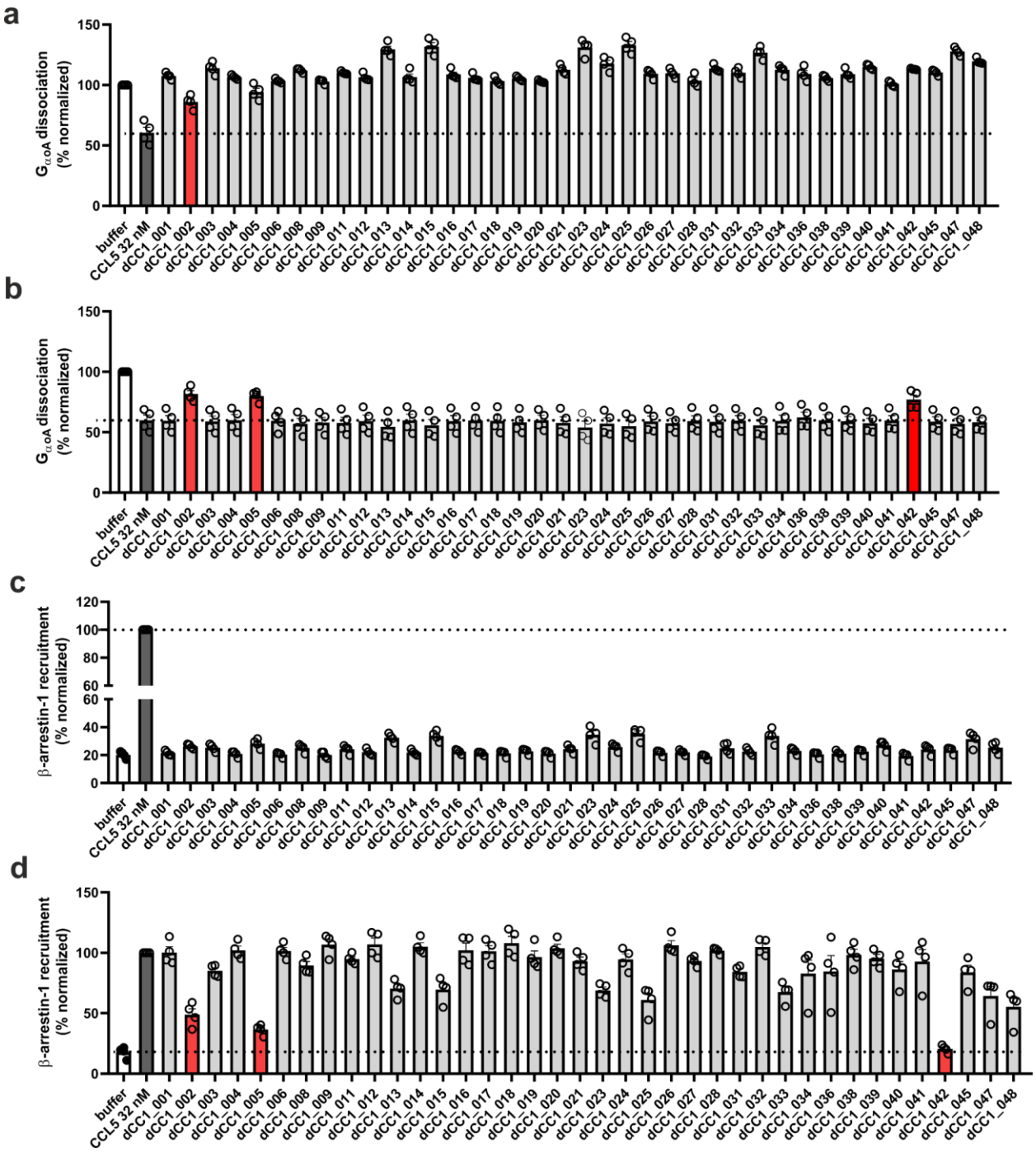

Supplementary Fig. 27. Screening of CCR5 binders. A single concentration of CCR5 binders was tested in **a** (agonist mode), **b** (antagonist mode) $G_{\alpha oA}$-protein dissociation and **c** (agonist mode), **d** (antagonist mode) β-arrestin-1 recruitment assays. Data are shown as mean ± s.e.m., n=4 biological replicates.

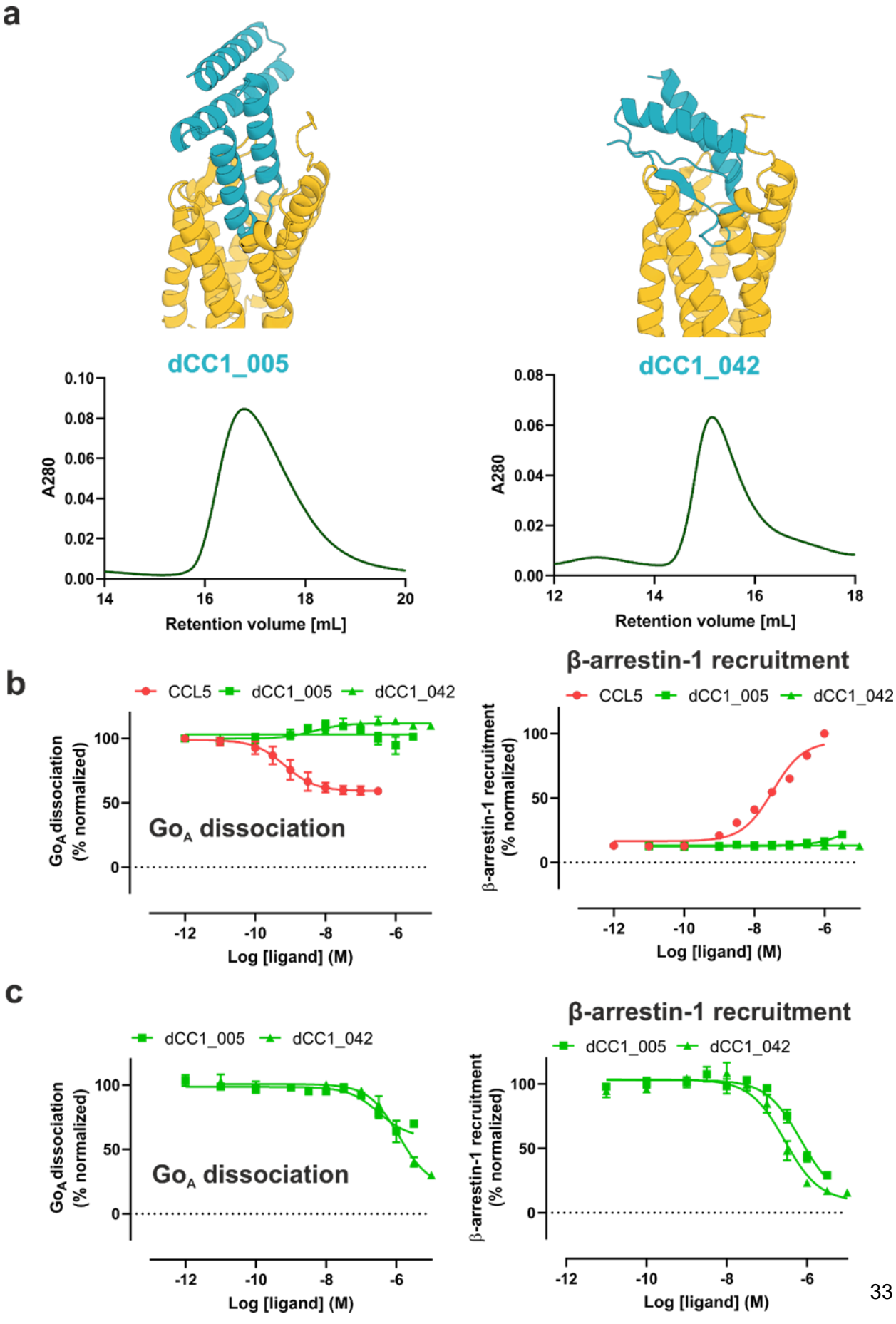
a
dCC1_005
dCC1_042
A280
Retention volume [mL]
b
CCL5
dCC1_005
dCC1_042
Go_A dissociation
(% normalized)
Go_A dissociation
β-arrestin-1 recruitment
β-arrestin-1 recruitment
(% normalized)
Log [ligand] (M)
c
dCC1_005
dCC1_042
Go_A dissociation
β-arrestin-1 recruitment
Log [ligand] (M)

Supplementary Fig. 28. Concentration-response curves of CCR5 antagonist hits. a Computational design models (blue) of dCC1_005 and dCC1_042 antagonists bound to CCR5 receptor (yellow, PDB ID: 5UIW) and their respective size-exclusion chromatography (SEC) traces. **b** No agonistic activity of dCC1_005 and dCC1_042 was detected in Go_A dissociation and β-arrestin-1 recruitment assays. **c** Antagonistic activity of dCC1_005 and dCC1_042 was confirmed in Go_A dissociation and β-arrestin-1 recruitment assays. HEK293T cells transiently expressing CCR5 were pre-incubated with varying concentrations of binders dCC1_005 and dCC1_042 followed by receptor stimulation with an EC_{80} concentration of CCL5. The IC_{50} values for dCC1_05 and dCC1_042 in Go_A dissociation assay were in the low micromolar range while in the β-arrestin-1 recruitment assay their IC_{50} values were 791 ± 162 nM (mean ± s.e.m., n=3 biological replicates) and 286 ± 38 nM (mean ± s.e.m., n=3 biological replicates), respectively.

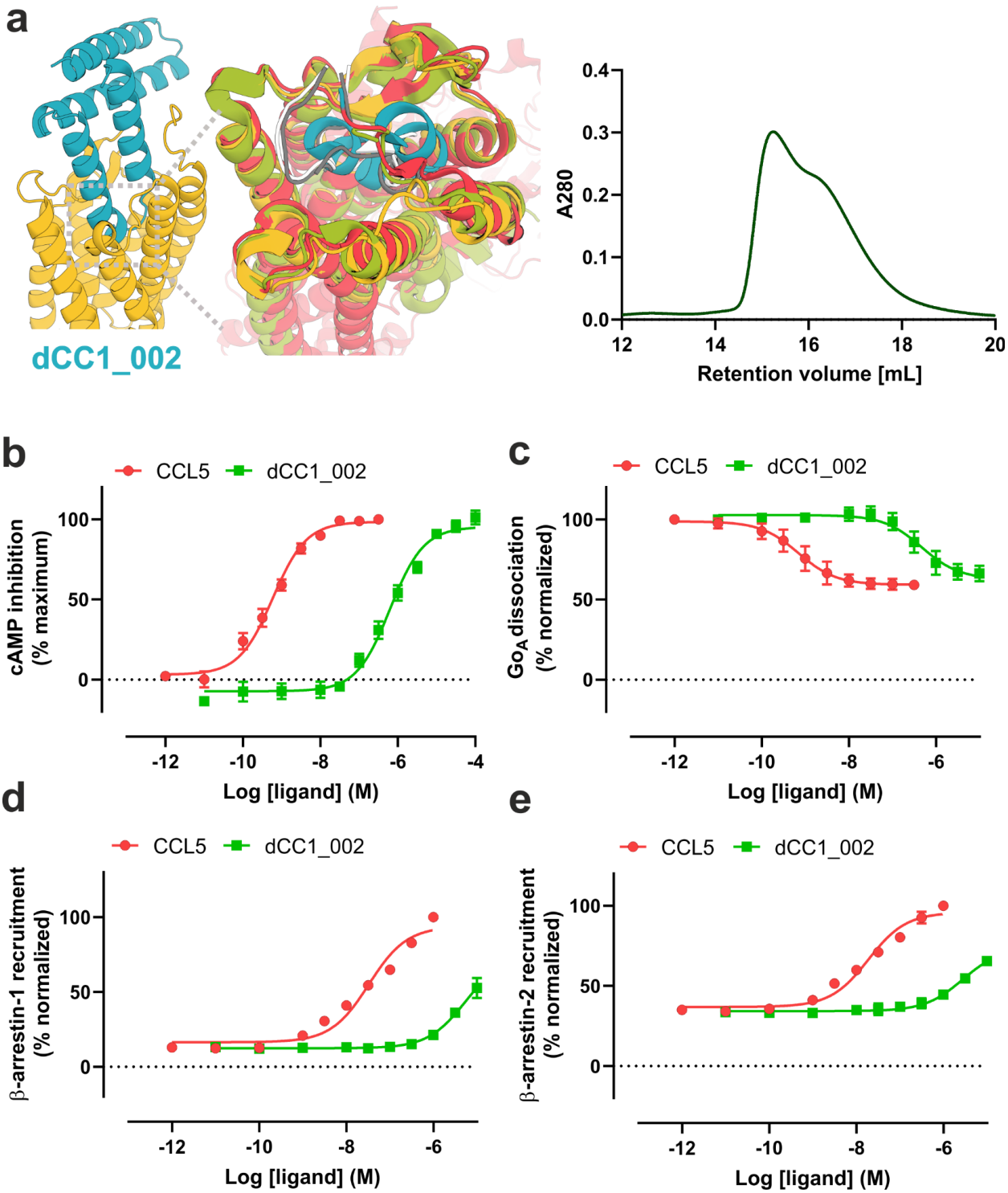

Supplementary Fig. 29. Structural comparison, SEC profile, and pharmacology of the CCR5 agonist dCC1_002. a Computational design model (blue) of dCC1_002 bound to CCR5 receptor (yellow, PDB ID: 5UIW, left). (inset) dCC1_002 engages receptor residues within the canonical binding pocket that are also contacted by agonists (PDB ID: 7F1Q, RANTES in white, CCR5 in red) as well as the antagonist 5P7-CCL5 (PDB ID: 5UIW, 5P7-CCL5 in grey, CCR5 in green). These residues are functionally important, as their mutation reduces potency and efficacy of native chemokines, and likely contribute to the agonistic

activity of dCC1_002. The structural comparison highlights that active- and inactive-state for CCR5 structures are highly similar at the binding site, with largely overlapping residue positions. Thus, while dCC1_002 was designed against an inactive-state template, it can still engage key agonist-associated contacts, suggesting that functional outcome depends on subtle differences in receptor geometry. Size-exclusion chromatography (SEC) trace of dCC1_002 (right). Agonistic activity of dCC1_002 was measured in **b** cAMP, **c** Go_A dissociation, **d** β-arrestin-1 and **e** β-arrestin-2 recruitment assays in HEK293T cells transiently expressing CCR5. Data are shown as mean ± s.e.m., n=3 biological replicates (Go_A dissociation, β-arrestin-1 and β-arrestin-2) and n=6 biological replicates (cAMP).

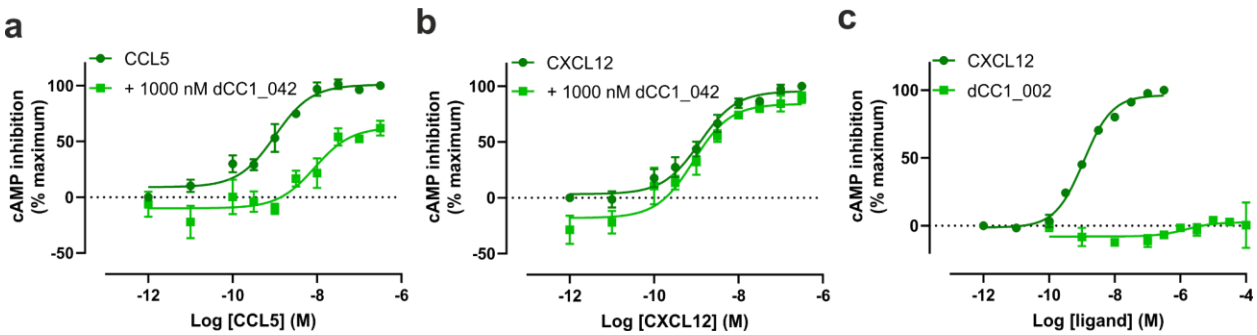

Supplementary Fig. 30. Selectivity profile of CCR5-targeting dCC1_042 antagonist and dCC1_002 agonist miniproteins. A single concentration of 1000 nM of dCC1_042 antagonist was co-incubated with varying concentrations of CCL5 or CXCL12 at **a** CCR5 or **b** CXCR4 in a cAMP assay. No antagonistic activity of the dCC1_042 antagonist was detected at CXCR4. **c** No agonistic activity of dCC1_002 miniprotein was observed at CXCR4 in a cAMP assay. Data are shown as mean ± s.e.m., n=3 biological replicates.

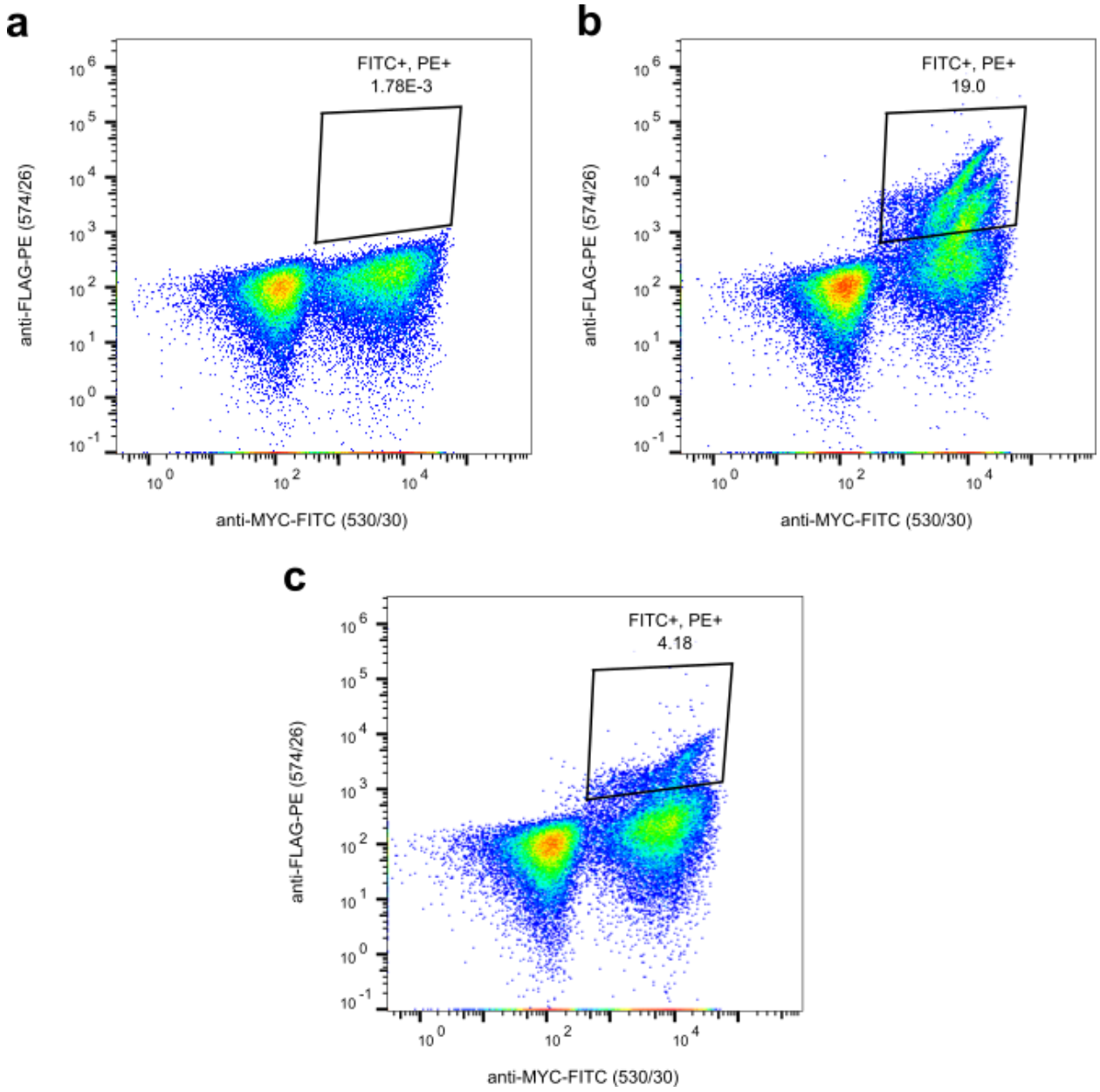

Supplementary Fig. 31. Yeast display of OXTR binders using nanodisc-stabilized OXTR and yeast display. Representative flow cytometry plots of binders are shown. x-Axis represents binder display and y-axis target OXTR binding. **a** Designed library of binders without the target OXTR represents a negative control. Yeast cells expressing binders on their surface were incubated with **b** 1000 nM or **c** 100 nM of OXTR. Data are shown from the fourth round of sorting. Gating strategy described in **Supplementary Fig. 8g** was used to measure target binding **b**, **c**.

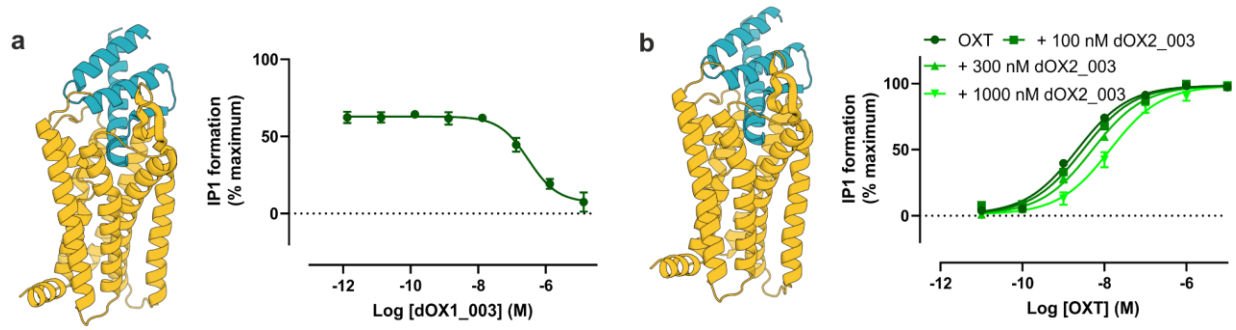

Supplementary Fig. 32. Pharmacology of OXTR-targeting binders. a Concentration-response curves of dOX1_003 antagonist in a functional IP1 assay to derive its IC_{50} of 330 ± 80 nM. Data shown are mean ± s.e.m, n=4 biological replicates. **b** Concentration-response curves of oxytocin (OXT) are concentration-dependently right shifted by dOX2_003 binder at HEK293 cells stably expressing OXTR. Data fit to the Gaddam-Schild equation in Prism to determine functional estimates for dOX1_003 are pA_2 of 6.7 ± 0.1 (251 nM) and a slope of 1.22 ± 0.38. Data shown are mean ± s.e.m, n=4 biological replicates. Computational design models are shown in blue and the 3D structure of the OXTR in yellow.

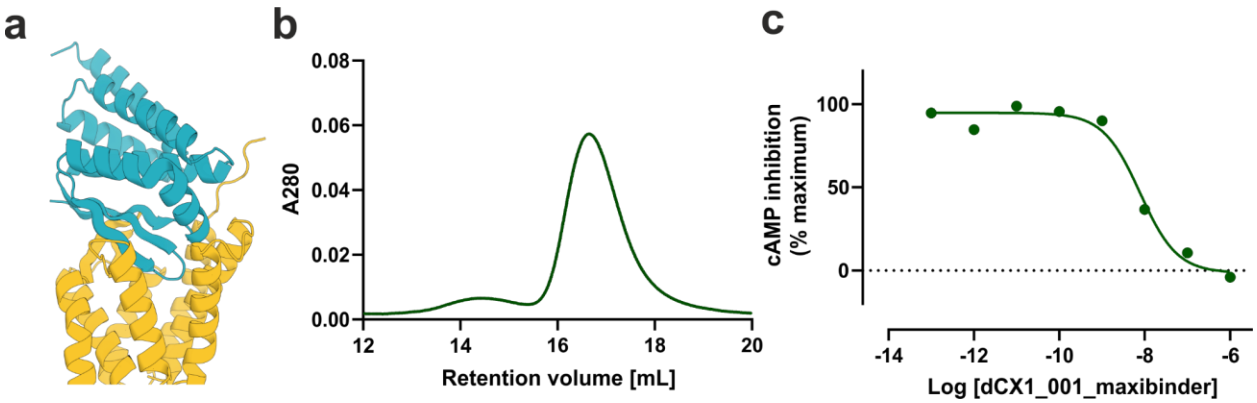

Supplementary Fig. 33. Characteristics of the dCX1_001_maxibinder targeting CXCR4. a Computational design model, **b** size-exclusion chromatography (SEC) and **c** concentration-response curve to determine IC_{50} value of the dCX1_001_maxibinder targeting CXCR4. The dCX1_001 antagonist was rigidly fused to *de novo* helical repeat (DHR) scaffolds to increase its size and yield maxibinder for cryo-EM structural determination (IC_{50} value = 9.4 nM, mean, n=2 biological replicates).

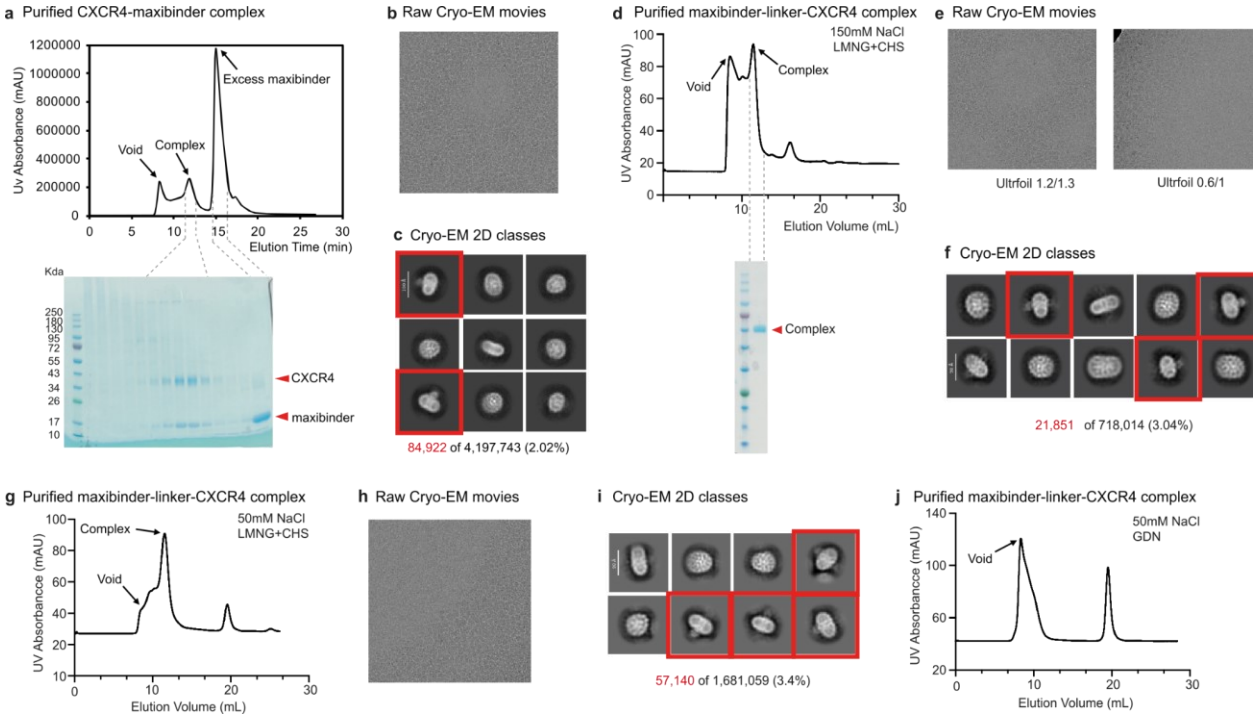

Supplementary Fig. 34. Purification and cryo-EM analysis of CXCR4 dCX1_001 maxibinder complexes. a FSEC profile and SDS–PAGE of the CXCR4-dCX1_001 maxibinder complex. dCX1_001 antagonist was rigidly fused to *de novo* helical repeat (DHR) scaffolds to increase its size (maxibinder). **b** Representative cryo-EM micrograph of the CXCR4-dCX1_001 maxibinder complex. **c** Representative 2D class averages of the CXCR4-maxibinder complex. **d** FSEC profile and SDS–PAGE of the maxibinder-linker-CXCR4 complex purified in LMNG/CHS with 150 mM NaCl. **e** Representative Cryo-EM micrograph of the maxibinder-linker-CXCR4 complex on different grids. **f** Representative 2D class averages of the maxibinder-linker-CXCR4 complex purified in LMNG/CHS with 150 mM NaCl. **g** FSEC profile of the maxibinder-linker-CXCR4 complex purified in LMNG/CHS with 50 mM NaCl. **h** Representative Cryo-EM micrograph of the complex purified in 50 mM NaCl. **i** Representative 2D class averages of the complex purified in 50 mM NaCl. **j** FSEC profile of the maxibinder-linker-CXCR4 complex purified in GDN with 150 mM NaCl.

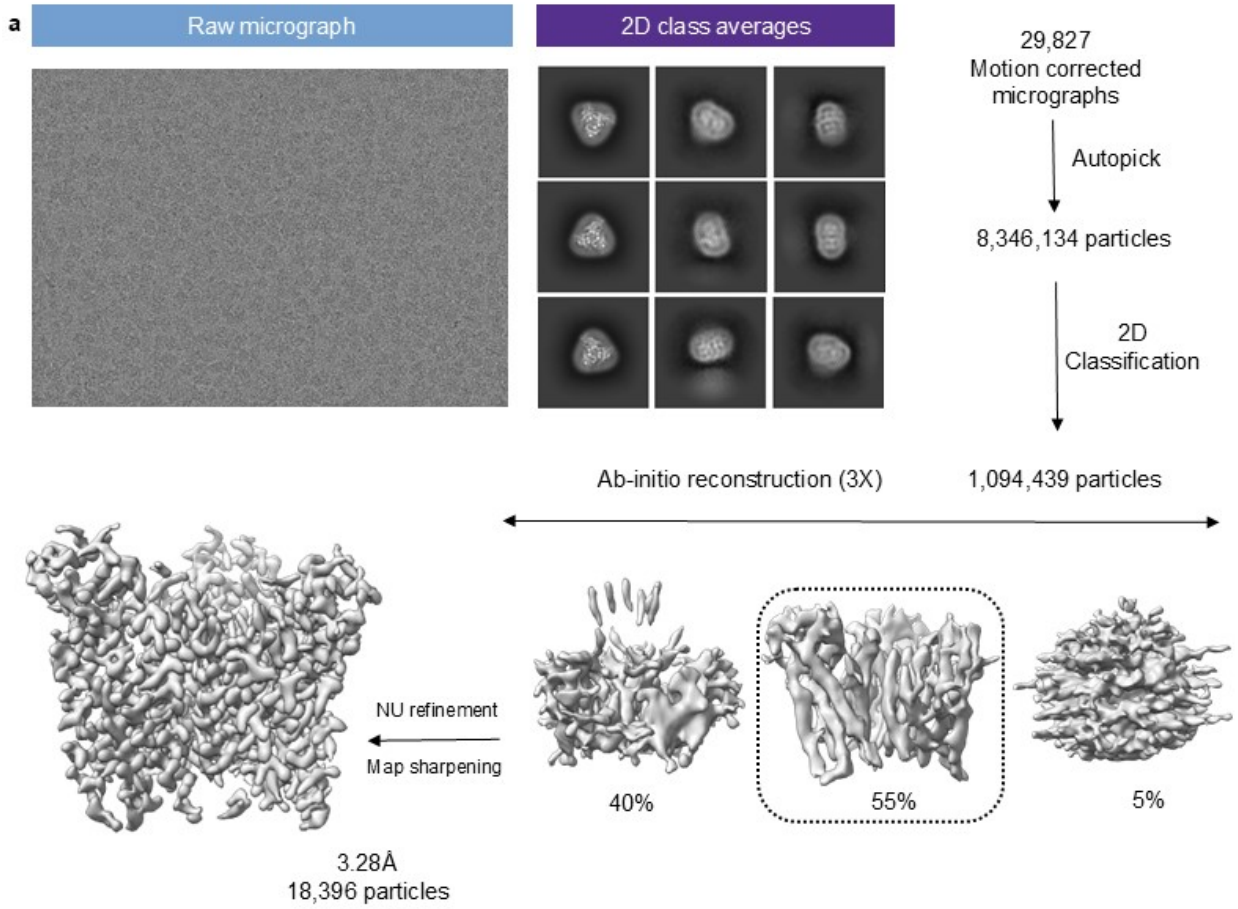

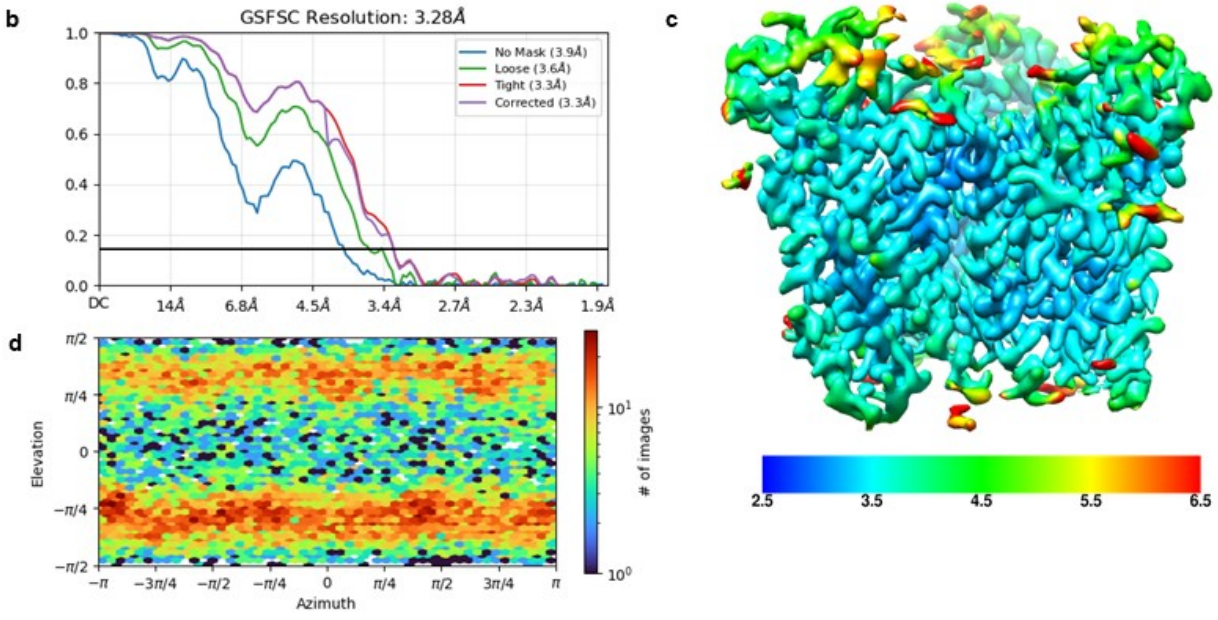

Supplementary Fig. 35: Cryo-EM data processing workflow of dCX001-CXCR4. a Schematic

representation of the cryo-EM data processing workflow. **b** Gold standard fourier shell correlation curve (GSFSC) at 0.143 threshold. **c** Local resolution map of the 3D reconstruction (front view). **d** Angular distribution of the particles used for final reconstruction.

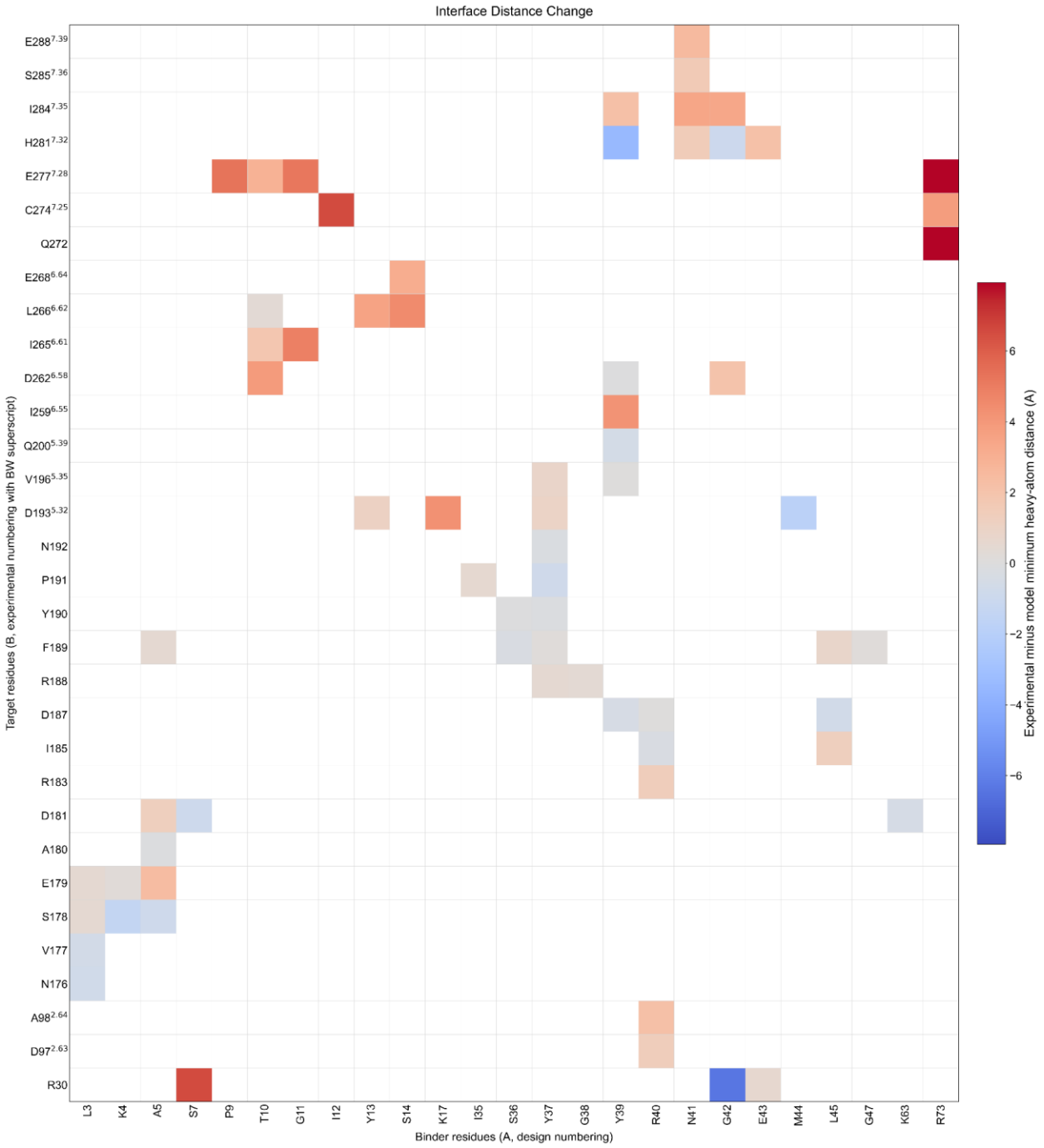

Supplementary Fig. 36. Residue-pair distance changes between the dCX1_001 design model and the solved CXCR4 complex. Heatmap shows Δd = d_experimental - d_model for mapped binder-target residue pairs, where d is the minimum heavy-atom distance between the two residues. Positive values indicate residue pairs that are farther apart in the solved structure than in the design model, whereas negative values indicate pairs that are closer. White cells denote residue pairs for which both distances are ≥4 Å and are therefore not shown. Binder residues are shown on the x axis in design numbering. CXCR4 residues are shown on the y axis in experimental numbering, with Ballesteros-Weinstein numbers indicated as superscripts for transmembrane residues; residues 77-80 are excluded. Although the pocket-inserting loop is shifted relative to the design model, many intended contacts remain close to their designed

geometry: among 77 comparable design contacts, 36, 46 and 55 differ by <1, <2 and <3 Å, respectively; within the loop-centred subset, 24 of 38, 30 of 38 and 35 of 38 contacts differ by <1, <2 and <3 Å, respectively.

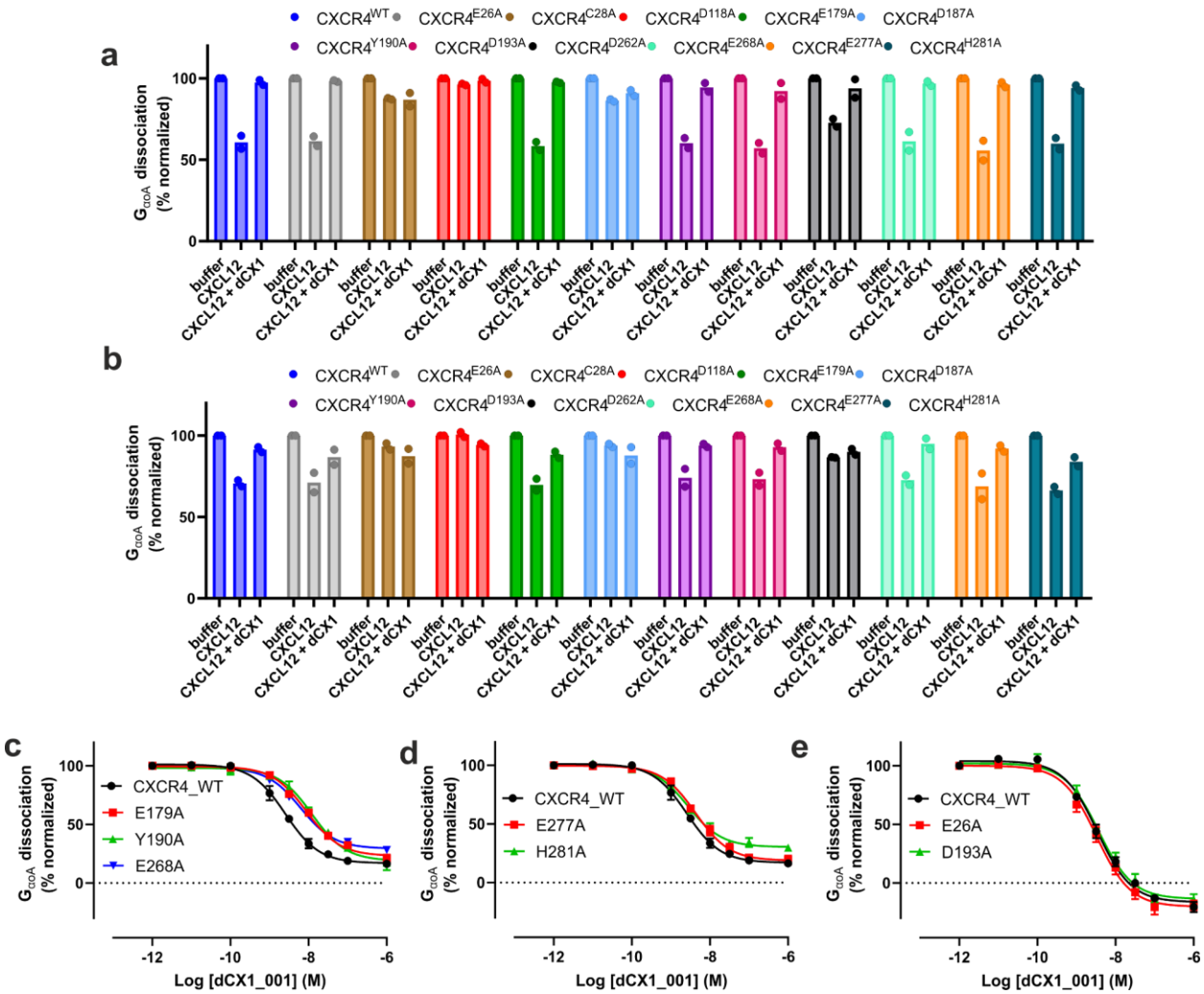

Supplementary Fig. 37. CXCR4 mutagenesis. Cells were pre-incubated with 1000 nM of dCX1_001 for 30 min and subsequently stimulated with **a** 100 nM or **b** 10 nM CXCL12 to assess G_{oA} dissociation response. Data are shown as mean, n=2 biological replicates. **c-d** Concentration-response curves were generated for selected CXCR4 mutations in $G_{\alpha oA}$ dissociation assay. Varying concentrations of dCX1_001 were pre-incubated followed by receptor stimulation with an EC_{80} of CXCL12. Seven CXCR4 mutations were selected based on retained $G_{\alpha oA}$ dissociation in response to CXCL12 stimulation, namely $E26A^{N\text{-}terminus}$, $E179A^{ECL2}$, $Y190A^{ECL2}$, $D193A^{5.32}$, $E268A^{6.64}$, $E277A^{7.28}$, and $H281A^{7.32}$. Data are shown as mean ± s.e.m., n=3 biological replicates.

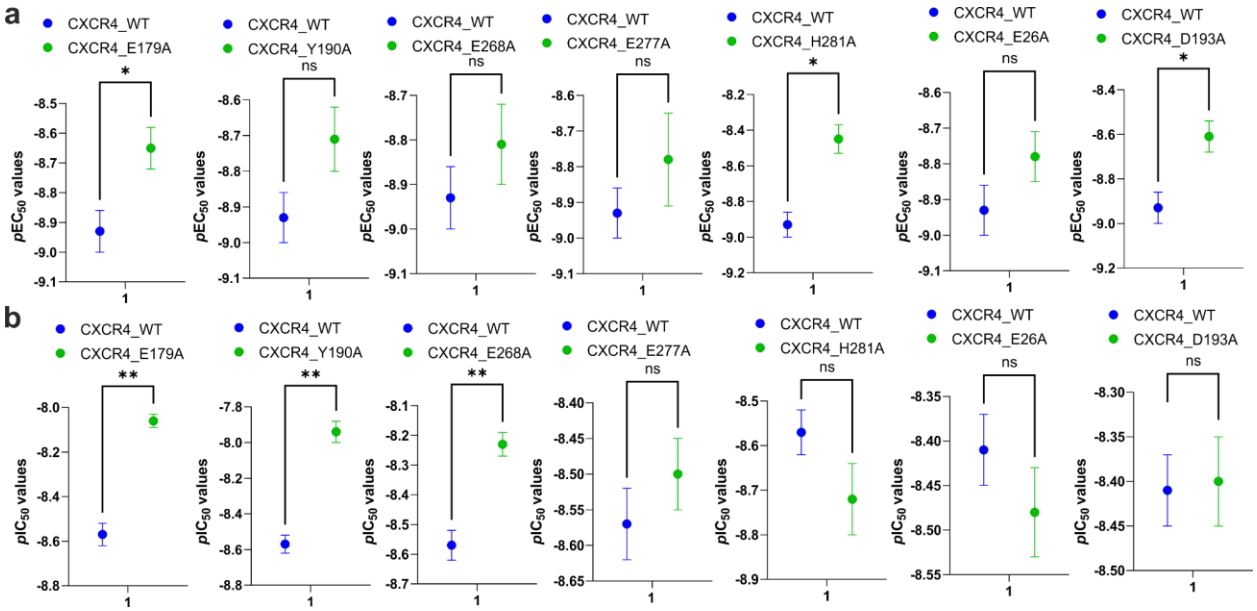

Supplementary Fig. 38. Statistical analysis of CXCR4 mutagenesis. a The pEC_{50} (CXCL12) and **b** pIC_{50} values (dCX1_001). Data represent mean ± s.e.m., n =3 biological replicates. Statistical analysis was performed using a two-sided unpaired t test with Welch's correction. Asterisks denote significant values, *$p \leq 0.05$, **$p \leq 0.01$, ns = not significant. Exact p values and detailed statistical analysis are provided in the Source data.

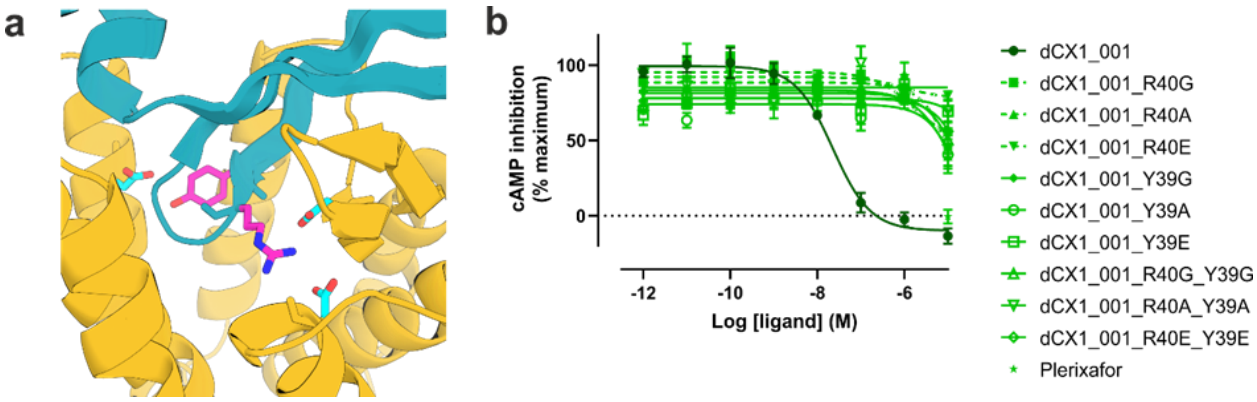

Supplementary Fig. 39. cAMP assay of dCX1_001 mutants at CXCR4. a dCX1_001 residues (pink) that engage receptor residues (blue) within the orthosteric binding pocket were used to generate single and double mutants. Binder residues were mutated to glycine (G), alanine (A) or aspartate (E). **b** The cAMP response was measured in CHO cells stably expressing CXCR4. Data are shown as mean ± s.e.m., n=3 biological replicates (plerixafor), n=4 biological replicates (dCX1_001), n=5 biological replicates (mutated dCX1_001 miniproteins). The concentration-response curve of dCX1_001 was replotted from **Supplementary Fig. 24a** for comparison.

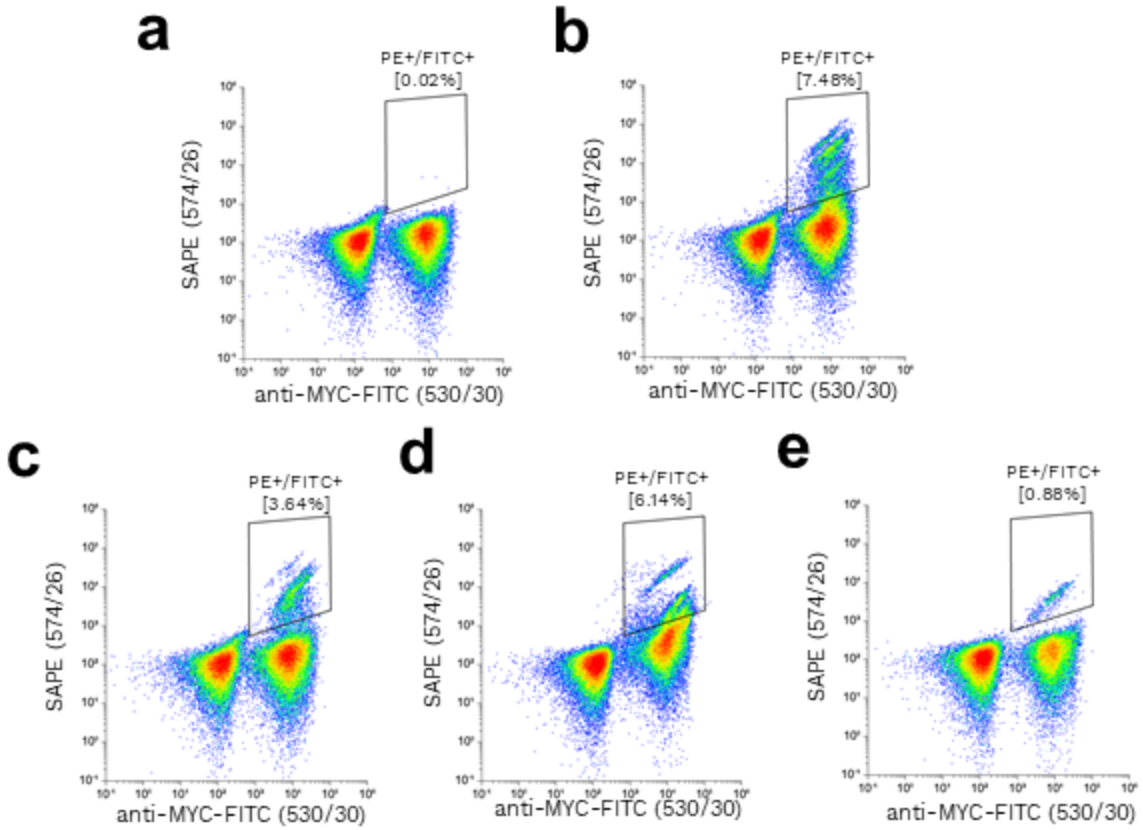

Supplementary Fig. 40. Yeast display of GLP1R MetaGen binders using soluble ECD. Representative flow cytometry plots of binders are shown. x-Axis represents binder display and y-axis target GLP1R binding. **a** Designed library of binders without the target GLP1R extracellular domain (ECD) represents a negative control. Yeast cells expressing binders on their surface were incubated with **b** 10 nM **c** 1 nM **d** 100 pM or **e** 10 pM of GLP1R ECD. Data are shown from the third and fourth round of sorting. Gating strategy described in **Supplementary Fig. 8g** was used to measure target binding **b-e**.

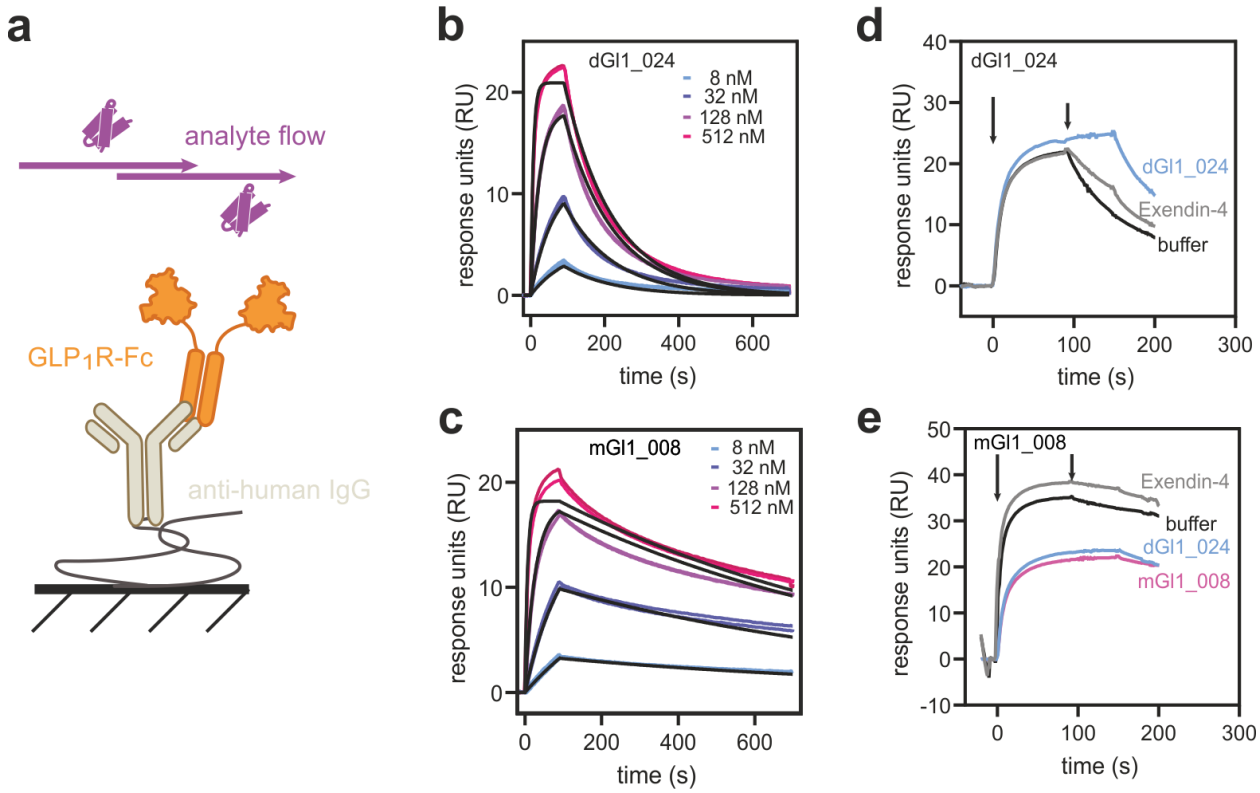

Supplementary Fig. 41. **Binding profiles of GLP1R miniprotein binders**. **a** Schematic of surface plasmon resonance (SPR) experimental setup with anti-human IgG surface capturing GLP1R ECD-Fc chimera fusion and *de novo* binders titrated as analyte. SPR binding sensorgrams (coloured curves) & 1:1 fits (black lines) for **b** dGI1_024 and **c** mGI1_008 binding to GLP1R-ECD at increasing concentrations. Dissociation constants (K_D) were 27 nM ± 6.3 nM and 5.3 nM ± 1.8 nM for dGI1_024 and mGI1_008, respectively (mean ± s.e.m., n=3 independent experiments). Duplicates and fits from one independent experiment are shown. Competition binding experiments of **d** dGI1_024 and **e** mGI1_008 to validate overlapping bin with an endogenous ligand. Injection of first dGI1_024 or mGI1_008 at t = 0s indicated by black arrow followed by immediate injection of second analyte at t = 90 s, both injection events indicated by black arrows.

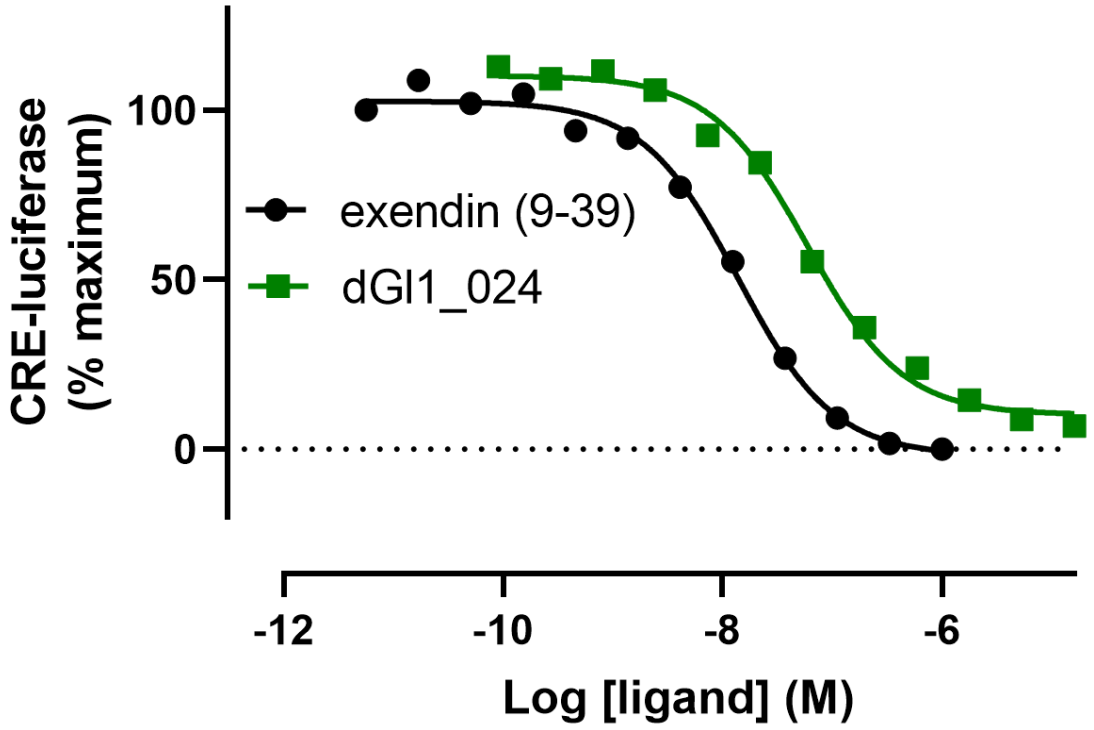

Supplementary Fig. 42. Pharmacological characterization of RFdiffusion-designed dGI1_024 antagonist of GLP1R. Antagonism of dGI1_024 at the GLP1R was tested using the reporter cell line BHK21/GLP1R/Cre-luc. Cells were treated with varying concentrations of the miniprotein prior to treatment with 15 pM of semaglutide, a GLP1R agonist. The binder antagonized GLP1R signaling with IC_{50} values of 61 ± 20 nM. Exendin 9-39 was used as positive control and had an IC_{50} 13.9 nM. Data are shown as mean, n=2 biological replicates.

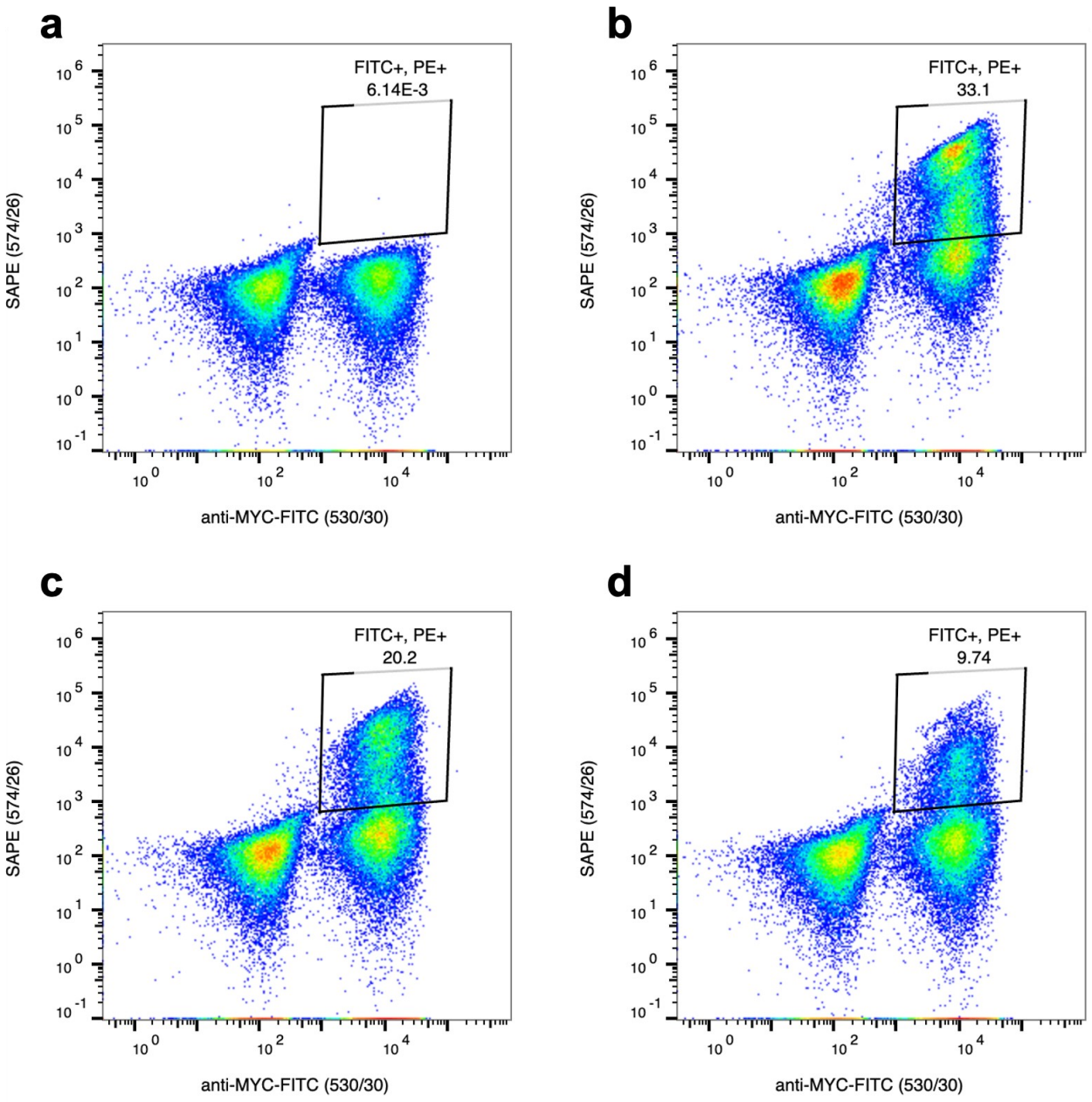

Supplementary Fig. 43. Yeast display of GIPR binders using soluble ECD. Representative flow cytometry plots of binders are shown. X-axis represents binder display and Y-axis target GIPR binding. **a** Designed library of binders without the target GIPR extracellular domain (ECD) represents a negative control. Yeast cells expressing binders on their surface were incubated with **b** 100 nM **c** 10 nM or **d** 1 nM of GIPR ECD. Data are shown from the third round of sorting.

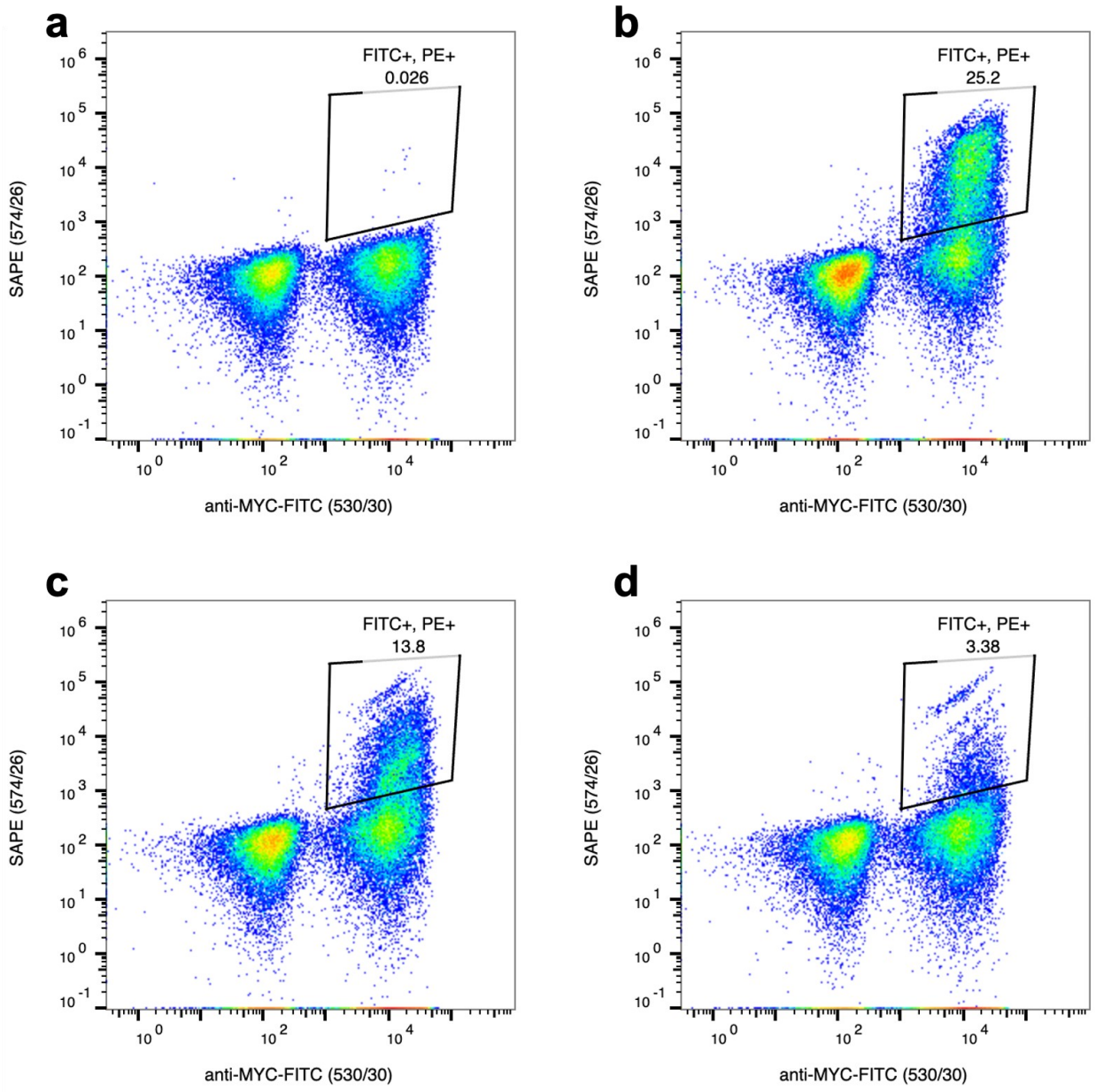

Supplementary Fig. 44. Yeast display of GCGR binders using soluble ECD. Representative flow cytometry plots of binders are shown. X-axis represents binder display and Y-axis target GCGR binding. **a** Designed library of binders without the target GCGR extracellular domain (ECD) represents a negative control. Yeast cells expressing binders on their surface were incubated with **b** 100 nM **c** 10 nM or **d** 1 nM of GCGR ECD. Data are shown from the third round of sorting.

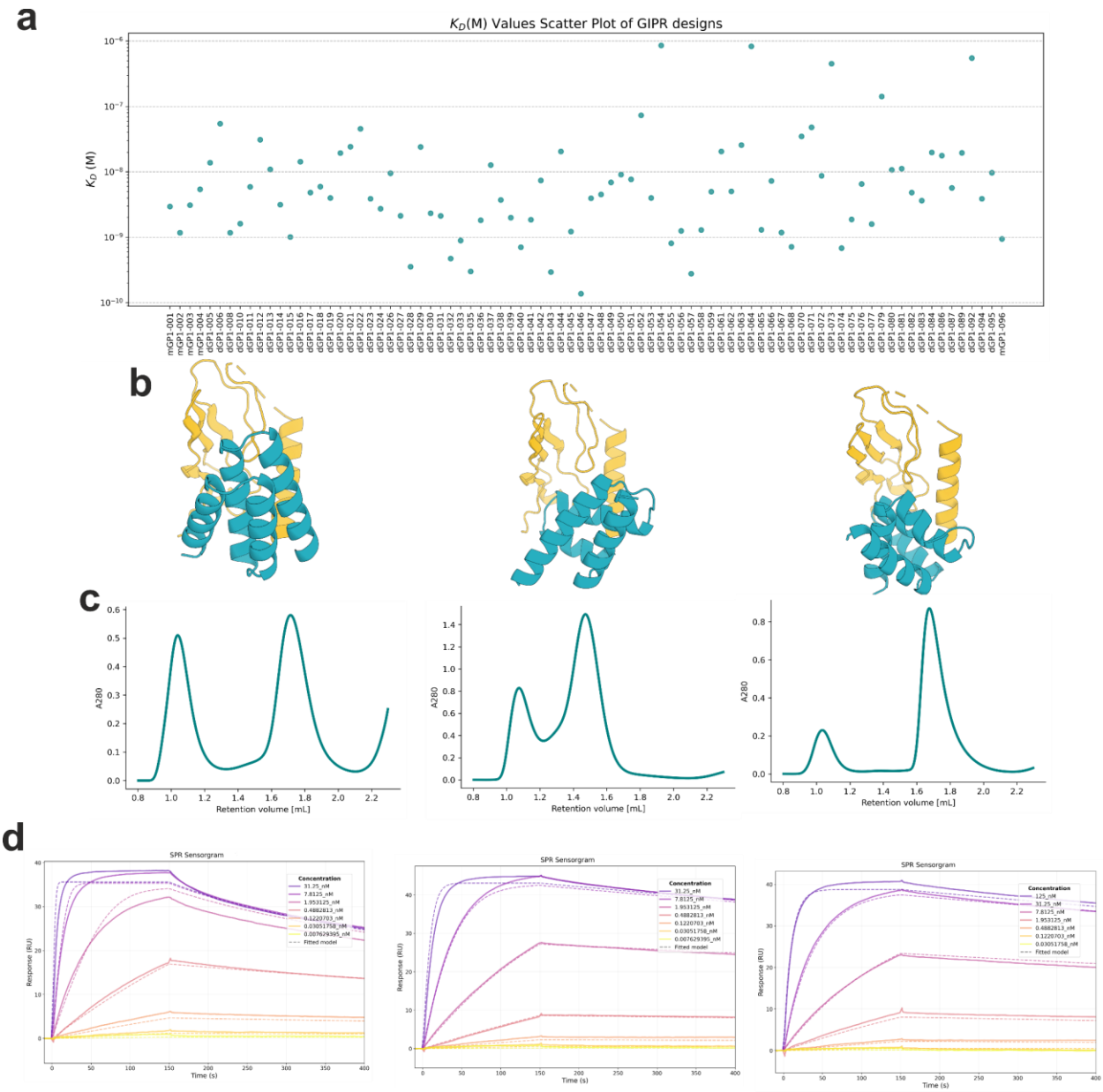

Supplementary Fig. 45. **Binding and biophysical characterization of GIPR binders**. **a** 96 GIPR designs from yeast library screening were purified. Binding kinetics of binders were measured using SPR. The resulting equilibrium dissociation constants (K_D(M)) are plotted. **b** Computational design models, **c** SEC traces and **d** sensorgrams of the three most potent binders dGP1_015 (left), dGP1_035 (middle) and dGP1_040 (right), respectively, identified in a functional cAMP assay.

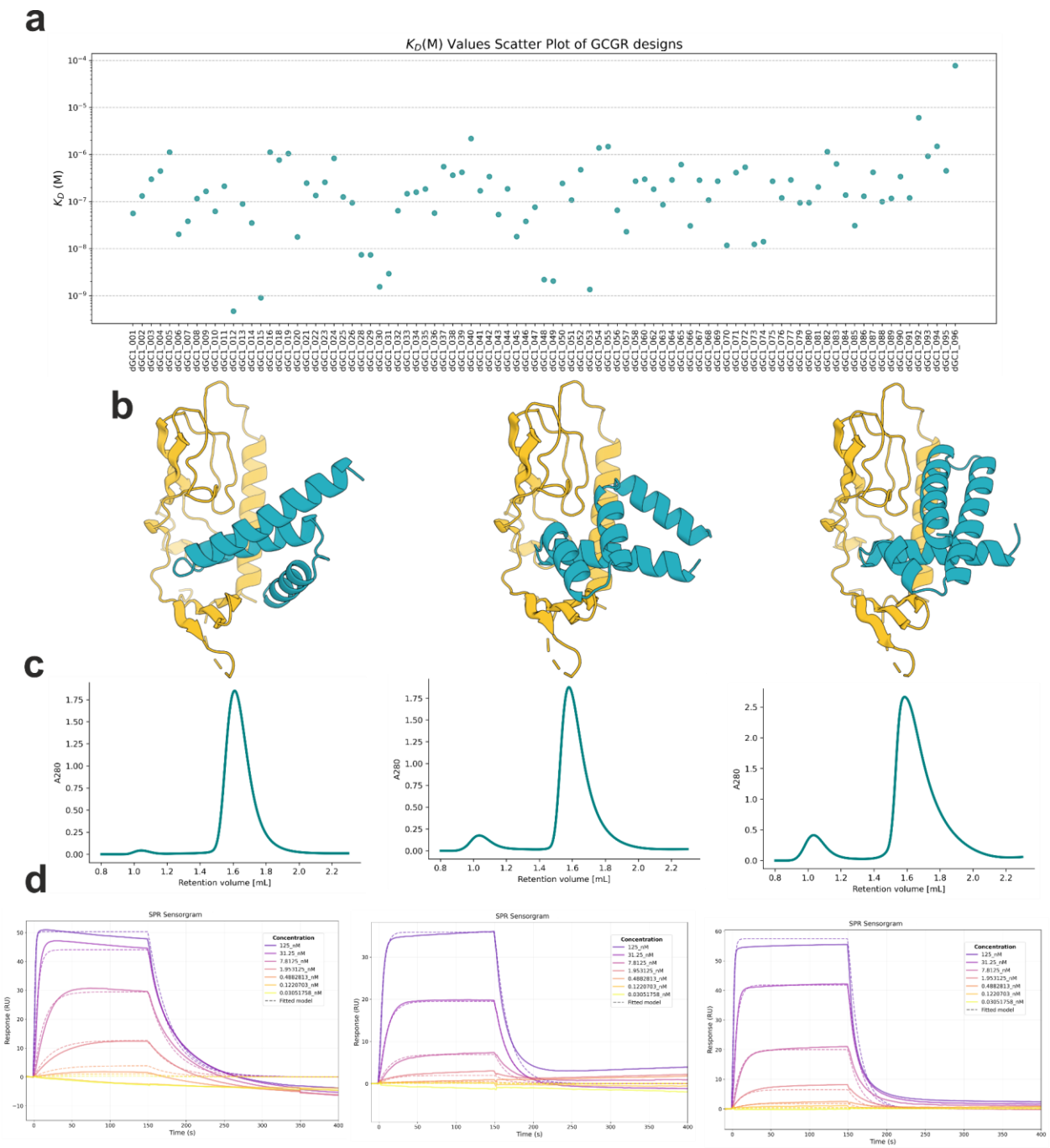

Supplementary Fig. 46. **Binding and biophysical characterization of GCGR binders**. **a** 96 GCGR designs from yeast library screening were purified. Binding kinetics of binders were measured using SPR. The resulting equilibrium dissociation constants (K_D(M)) are plotted. **b** Computational design models, **c** SEC traces and **d** sensorgrams of representative binders dGC1_012 (left), dGC1_015 (middle) and dGC1_053 (right), respectively, showing strong binding affinity.

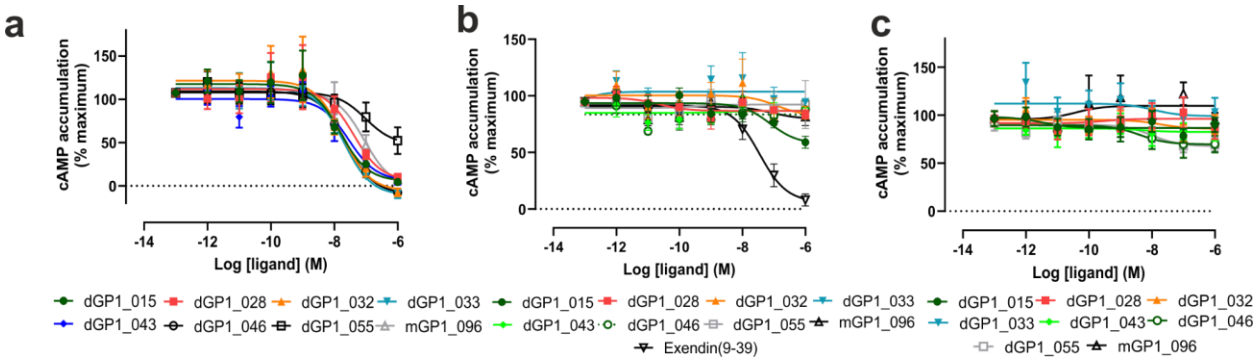

Supplementary Fig. 47. Selectivity of GIPR binders at GLP1R and GCGR. The ability of GIPR binders to inhibit GIP (1-42)-, GLP-1 (7-36 NH_2)- or glucagon-induced signaling at **a** GIPR, **b** GLP1R or **c** GCGR was measured in a cAMP assay. Data are shown as mean ± s.e.m., n=4 biological replicates (GIPR, GLP1R) and n=6 biological replicates (GCGR). Exendin (9-39) served as a positive control for GLP1R and had an IC_{50} of 49 ± 31 nM (mean ± s.e.m., n=4 biological replicates).

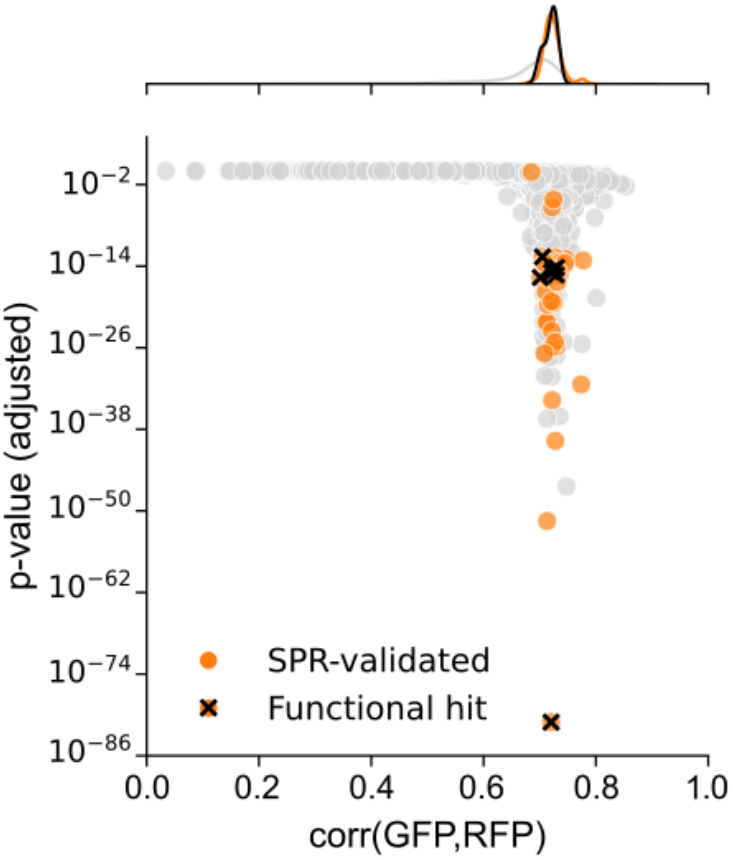

Supplementary Fig. 48. Identification of PTH1R binders using OPS-RD high-throughput screen. 9,062 8,966 miniprotein binders were designed as antagonists targeting the ECD of PTH1R and screened using OPS-RD. The GFP-RFP pixel cross-correlation (corr(GFP,RFP)) induced in cells with the same design was compared to the cross-correlation distribution across all imaged cells, and P values were computed using a (one-sided) Kolmogorov–Smirnov (K-S) test. Raw P values were adjusted using the Benjamini-Hochberg procedure to control the false discovery rate. Detailed analysis is provided in the PTH1R dataset (Data availability). A subset of hits was validated for binding by SPR (highlighted in orange) and further tested for function (hits highlighted by crosses).

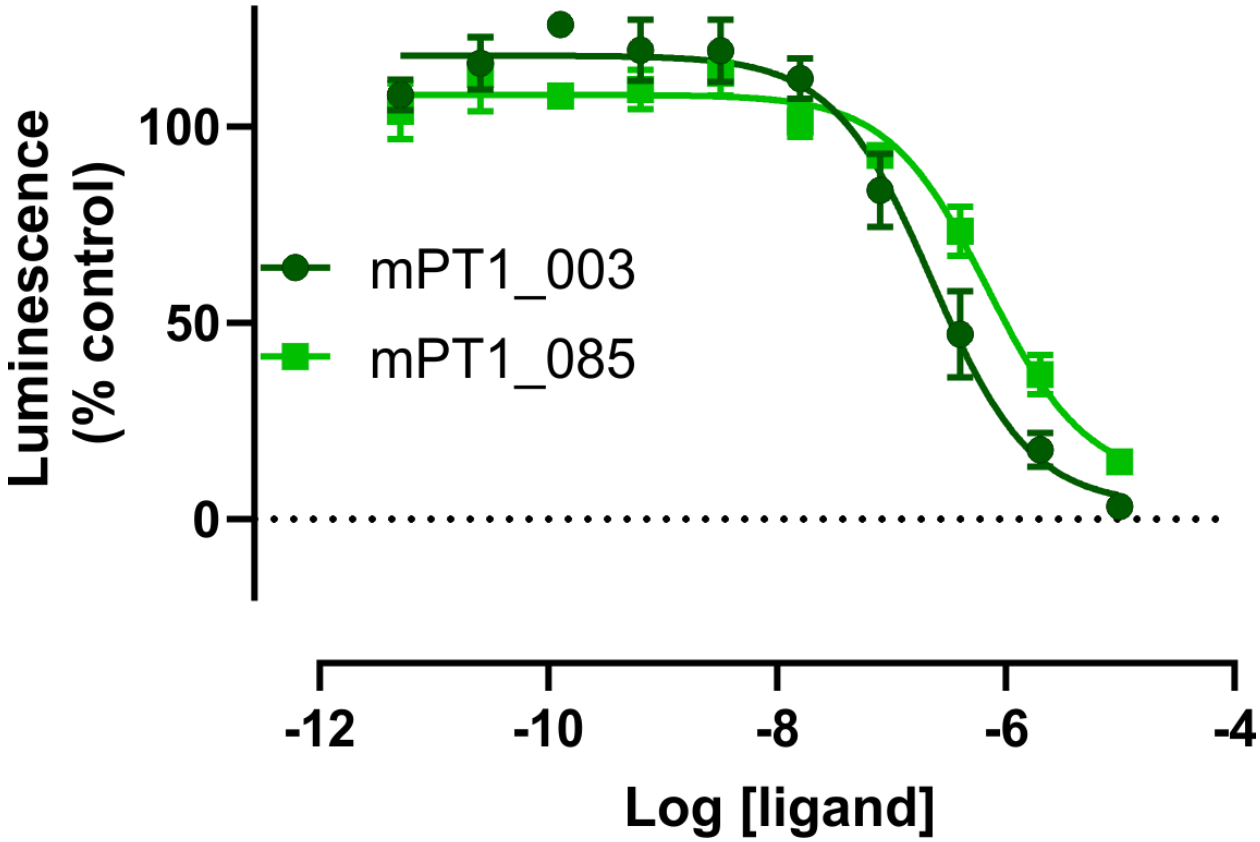

Supplementary Fig. 49. Antagonism of PTH1R binders in a β-arrestin-2 recruitment assay. To derive IC_{50} values of the most potent PTH1R miniproteins a β-arrestin-2 recruitment assay was performed. The IC_{50} values for mPT1_003 and mPT1_085 were 280 ± 110 nM and 810 ± 250 nM, respectively. Data are shown as mean ± s.e.m., n=3 biological replicates.

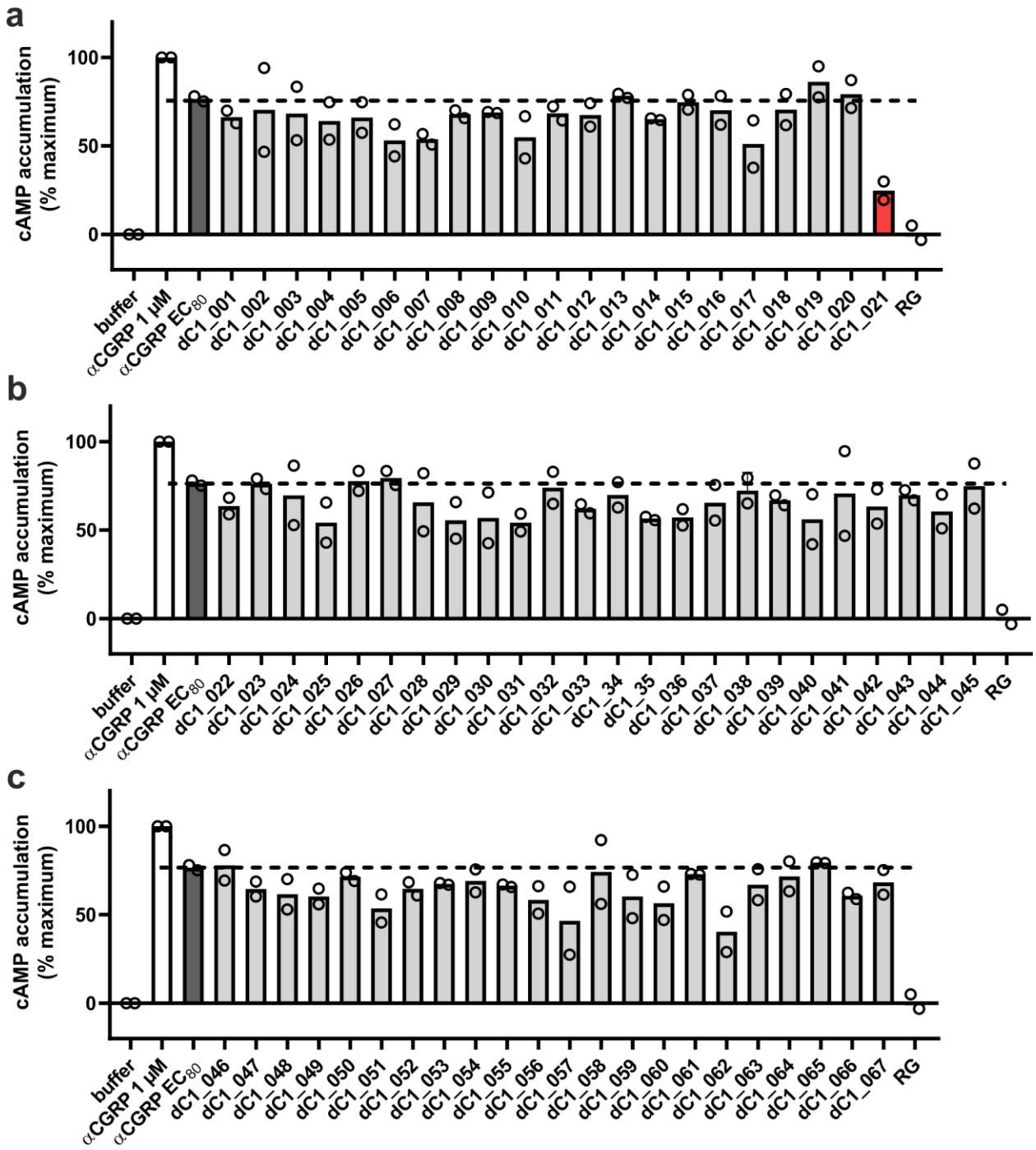

Supplementary Fig. 50: One-point cAMP assay of RFdiffusion-designed miniprotein binders at the CGRPR. a-c Binders were tested at a concentration of 1-10 μM. The identified hit is highlighted in red. Rimegepant (RG) served as a positive control (10 μM). Data are shown as mean, n=2 biological replicates.

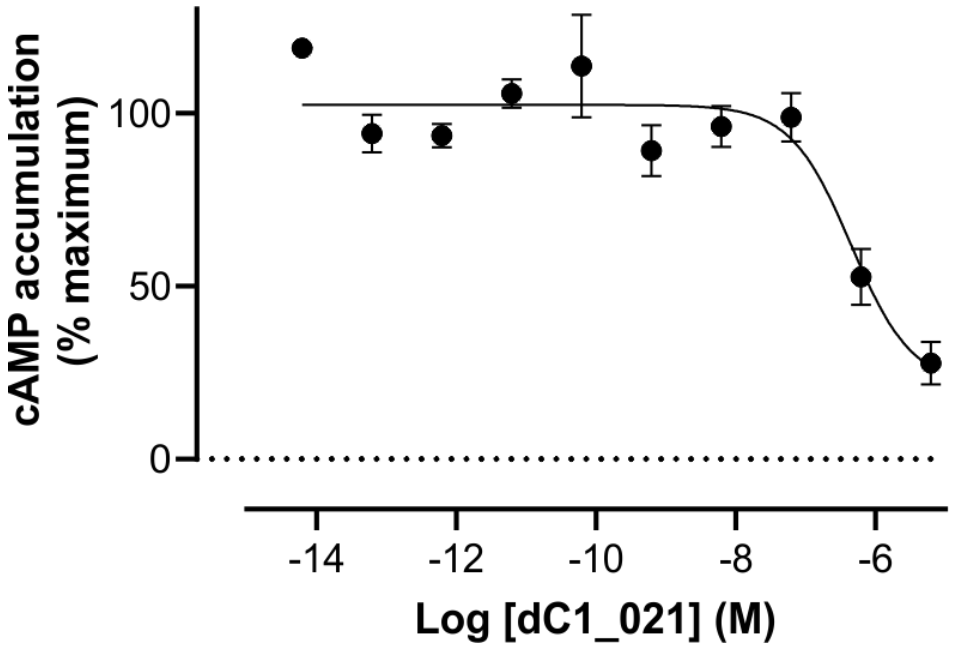

Supplementary Fig. 51. cAMP assay of dC1_021 at the CGRPR. The concentration-response curve of dC1_021 was generated in the presence of an EC_{80} value of αCGRP and increasing concentrations of the binder. The IC_{50} value of the binder was 440 ± 40 nM. Data are shown as mean ± s.e.m., n=3 biological replicates.

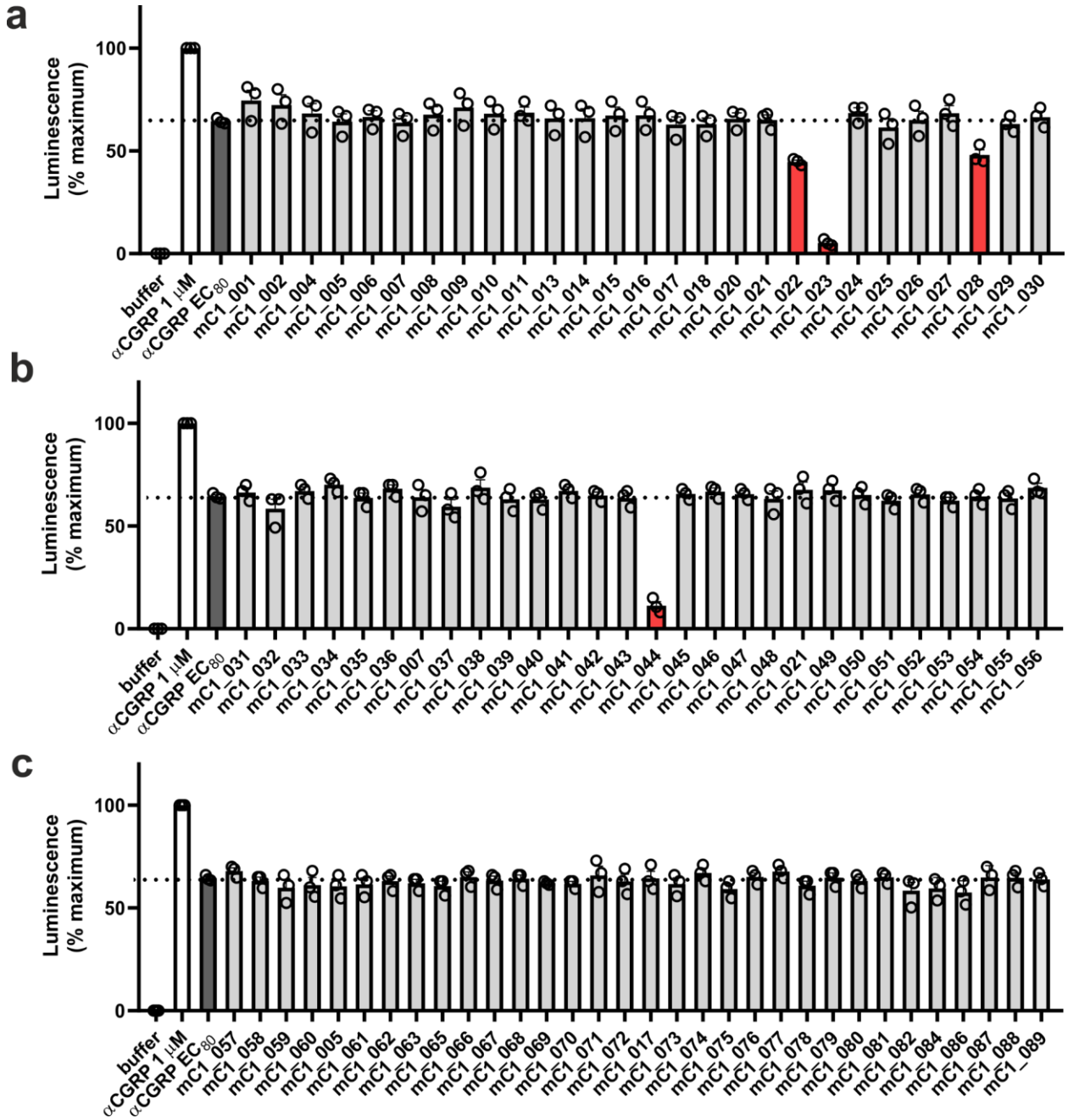

Supplementary Fig. 52. One-point luciferase assay of miniprotein binders at the CGRPR designed by MetaGen approach. a-c Binders were tested at a concentration of 1-10 μM. Hits with the most pronounced potency are highlighted in red. Data are shown as mean ± s.e.m., n=3 biological replicates..

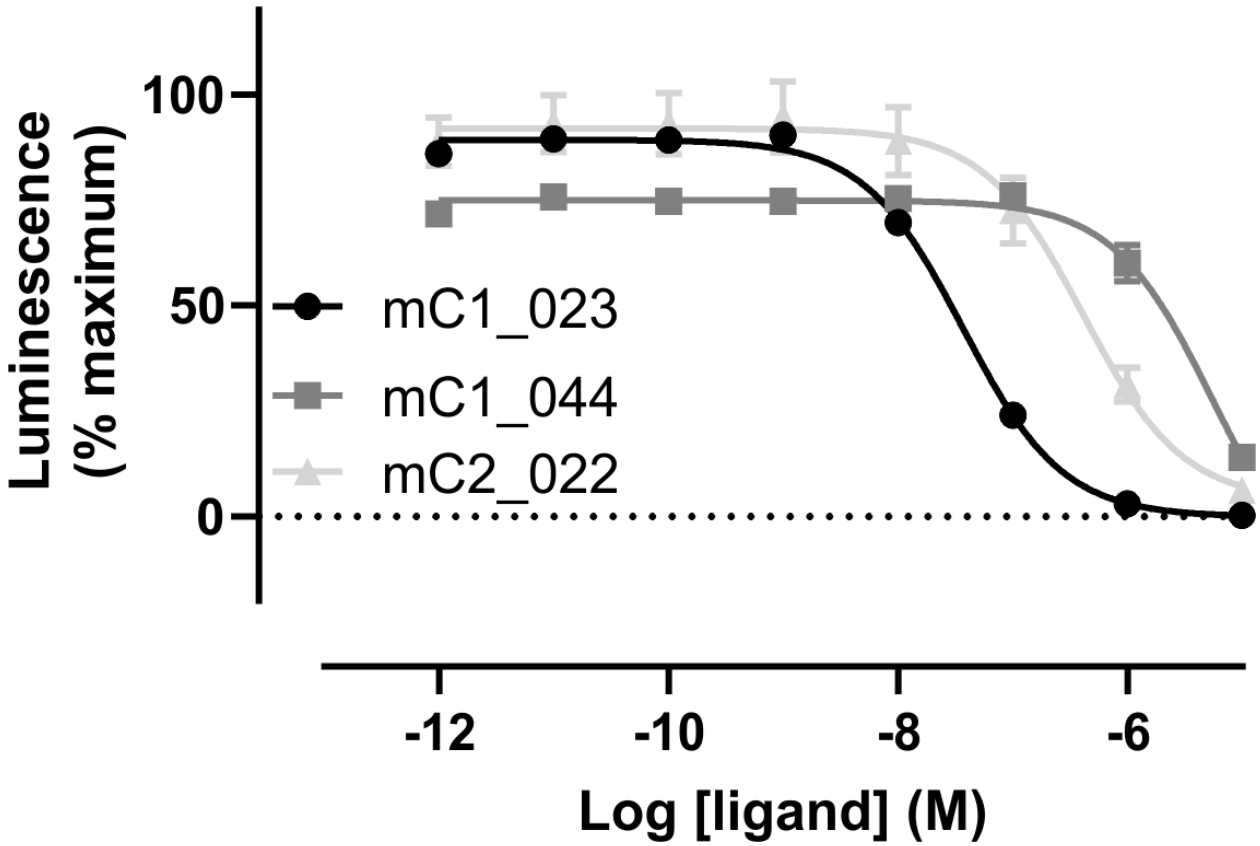

Supplementary Fig. 53. Concentration-response curves of miniprotein binders to the CGRPR designed by MetaGen. Concentration-response curves of mC1_023, mC1_044 and mC2_022 were generated by measuring luciferase activity in the presence of an EC_{80} concentration of αCGRP following pre-incubation with increasing concentrations of miniproteins in CHO-K1/Cre-Luc/CGRPR cells. The IC_{50} values for mC1_023 and mC2_022 are 37 ± 2 nM and 420 ± 60 nM whereas mC1_044 had an IC_{50} value in the low micromolar range. Data are shown as mean ± s.e.m., n=4 biological replicates (mC1_023), n=3 biological replicates (mC1_044) and n=4 biological replicates (mC2_022).

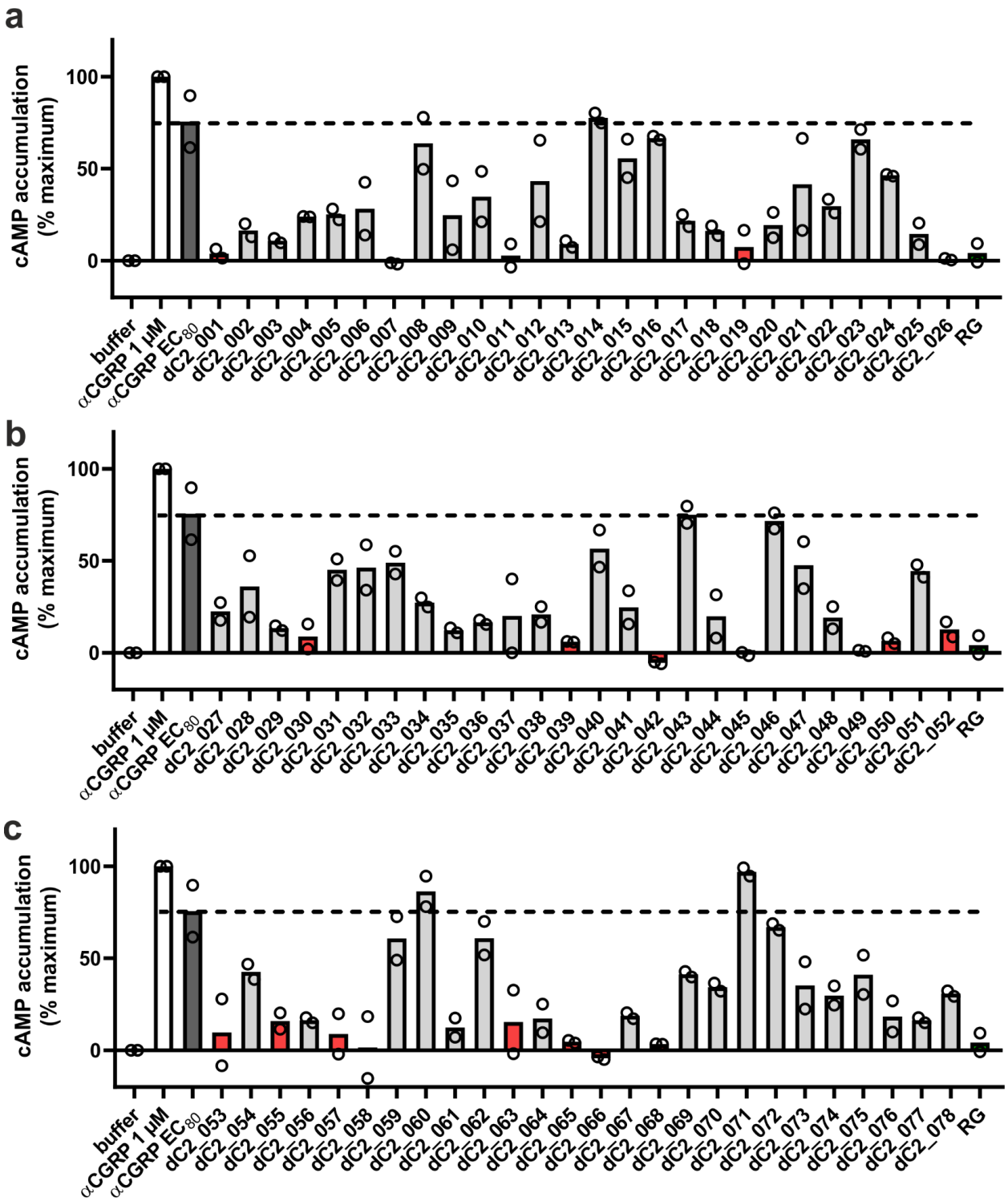

Supplementary Fig. 54. One-point cAMP assay of miniprotein binders at the CGRPR following partial diffusion. a-c Binders were tested at a concentration of 1-10 μM. Hits with the most pronounced potency are highlighted in red. Rimegepant (RG) served as a positive control (10 μM). Data are shown as mean, n=2 biological replicates.

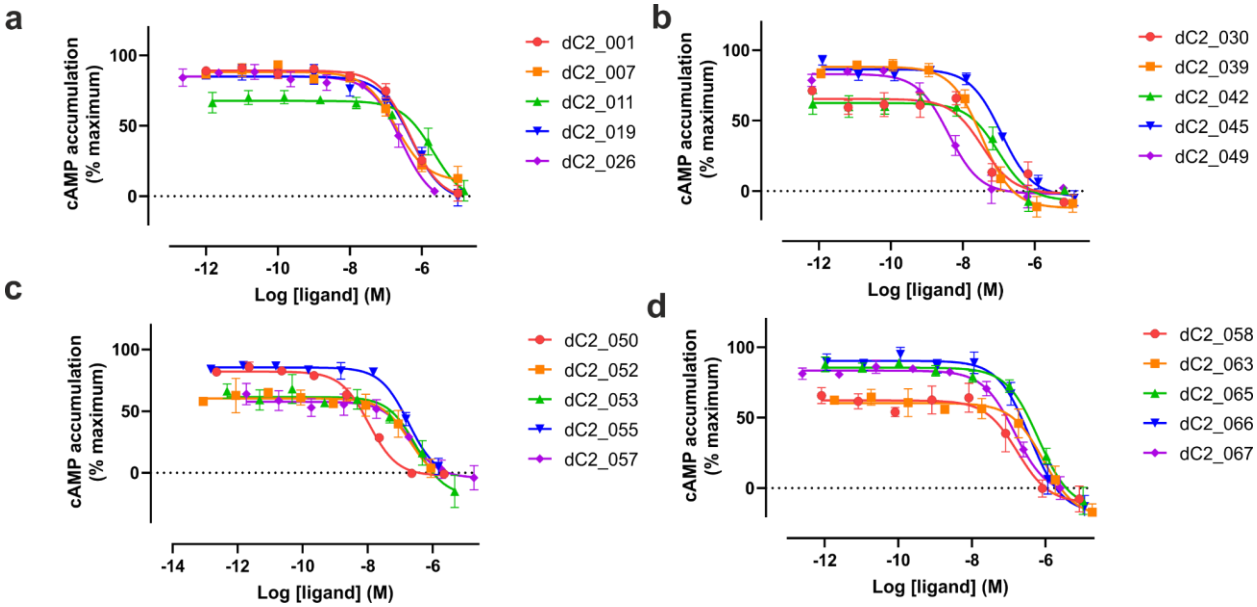

Supplementary Fig. 55. Concentration-response curves of miniprotein binders at the CGRPR following partial diffusion. a-d Antagonism by miniprotein binders was determined by co-incubation with an EC_{80} of αCGRP and measuring cAMP accumulation. Data are shown as mean ± s.e.m., n=3 or n=4 biological replicates (see Source data for exact n values).

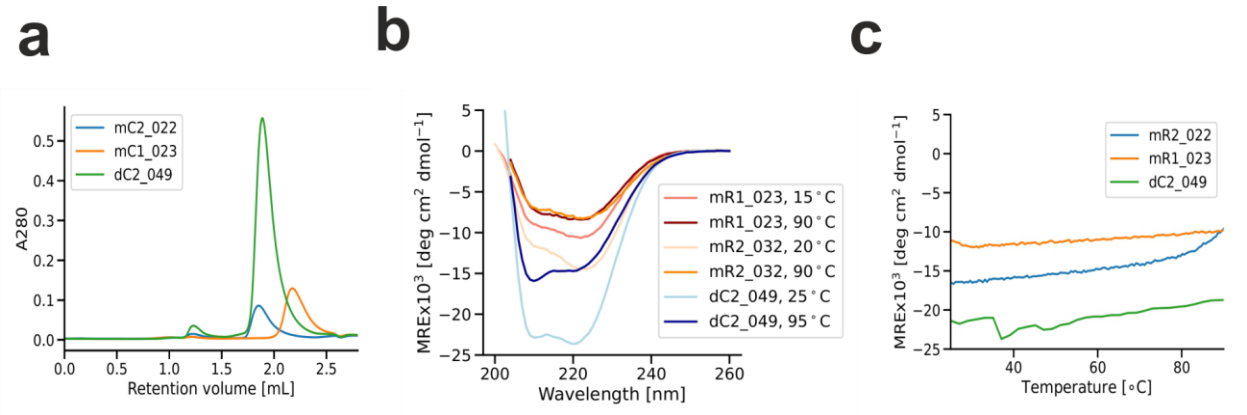

Supplementary Fig. 56. Biophysical characterization of mC1_023, mC2_022 and dC2_049 binders at the CGRPR. a Size-exclusion chromatography (SEC) traces, **b** circular dichroism (CD) spectra and **c** melting curves of MetaGen mC1_023 and mC2_022 and RFdiffusion dC2_049 binders at the CGRPR.

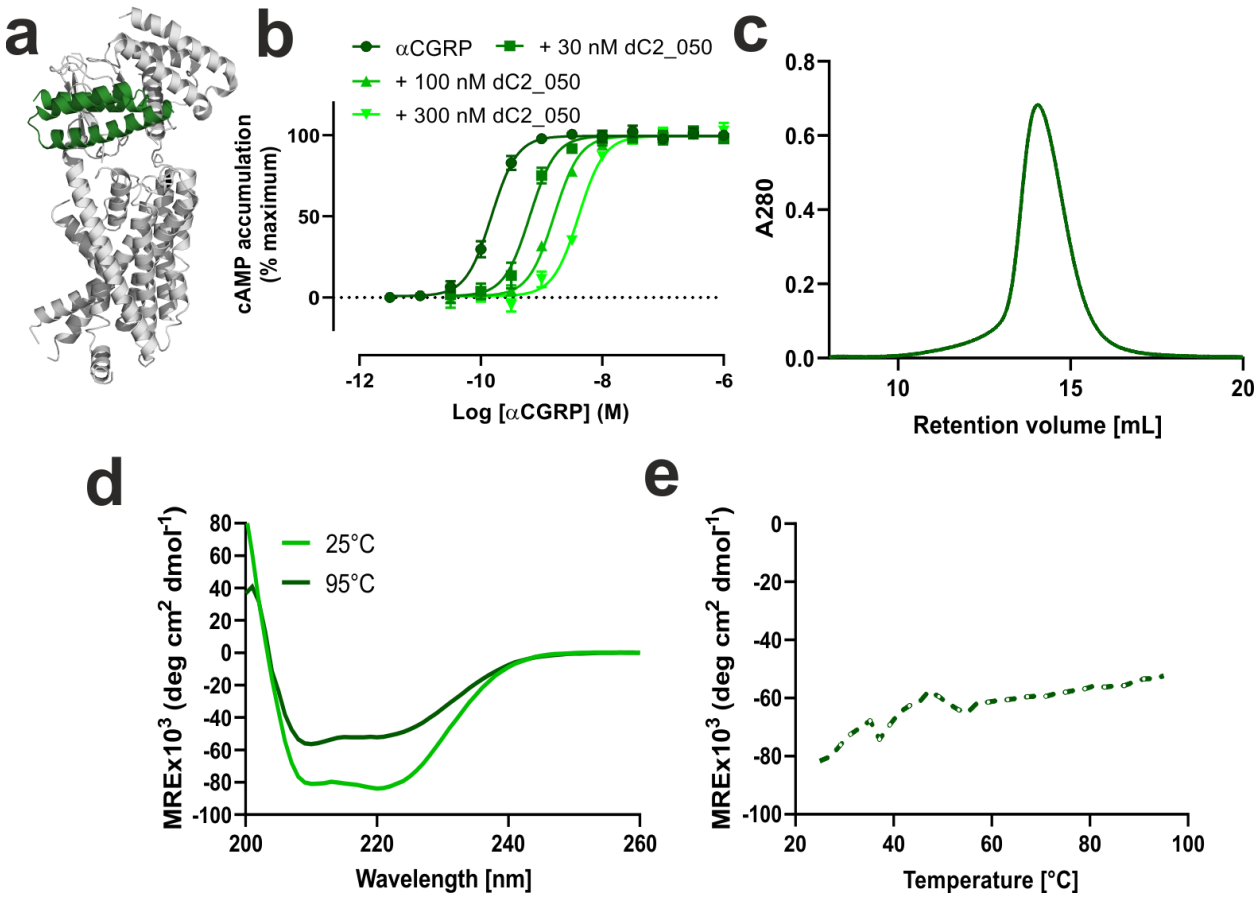

Supplementary Fig. 57. Biophysical characterization and pharmacology of the dC2_050 binder at the CGRPR. a Computational design model (green) of dC2_050 bound to the CGRPR receptor (gray, PDB ID: 6E3Y). **b** Concentration response curves of αCGRP in the presence of increasing concentrations of dC2_050 binder. The calculated pA_2 value is 8.1 ± 0.1 (7.9 nM) and the slope is 0.90 ± 0.05 with R2 = 0.98. Data are shown as mean ± s.e.m., n=4 biological replicates. **c** Size-exclusion chromatography (SEC) traces**, d** circular-dichroism (CD) spectra and **e** melting curve of dC2_050 binder.

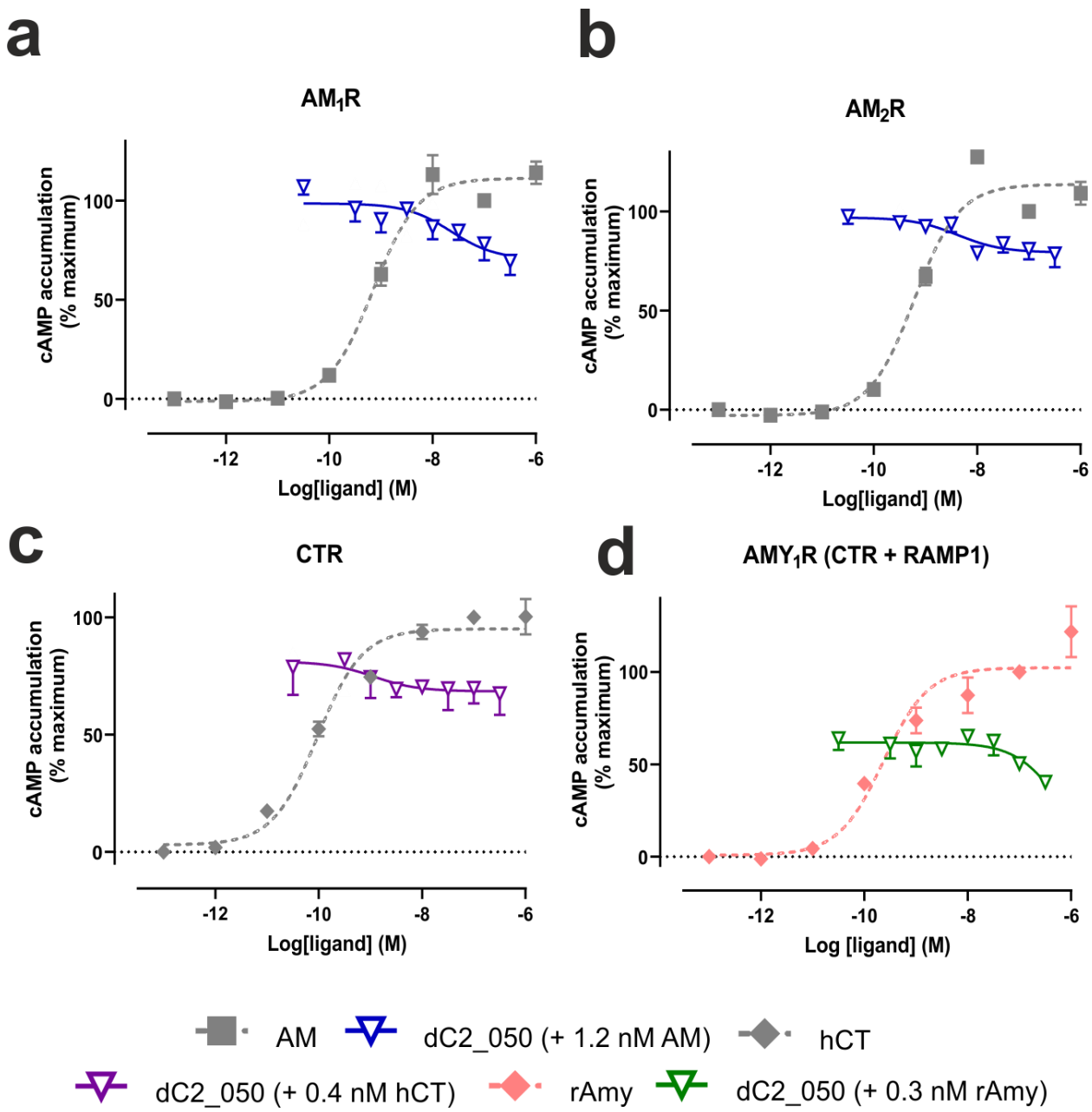

Supplementary Fig. 58. Selectivity profile of dC2_050 binder. dC2_050 binder displays little or no antagonism of cognate peptide agonists at **a** AM_1R, **b** AM_2R, **c** CTR and **d** AMY_1R transiently expressed in COS-7 cells. Data shown are mean ± s.e.m., n=4 biological replicates.

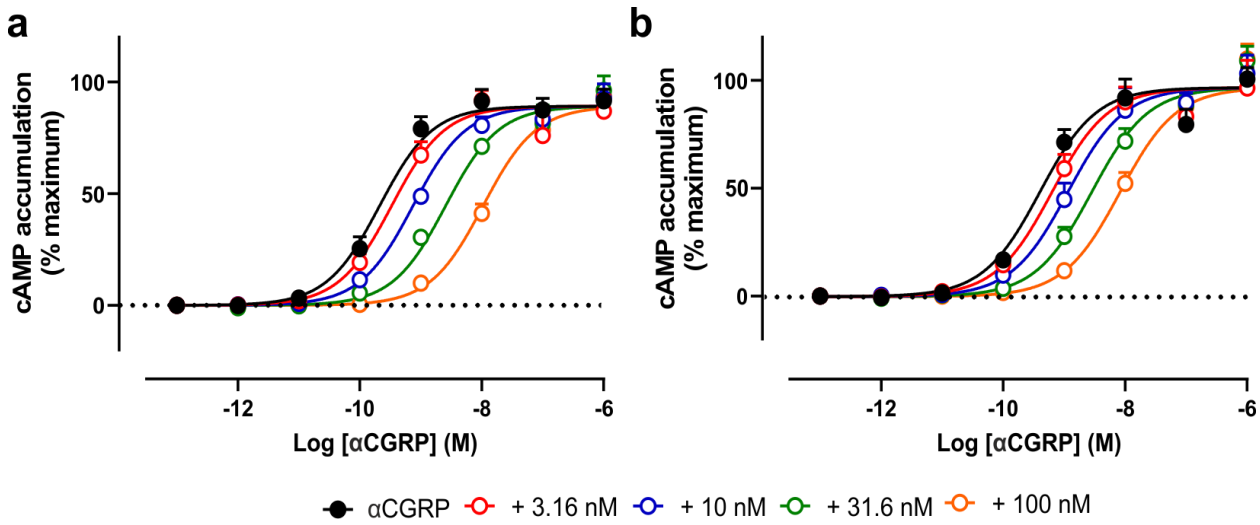

Supplementary Fig. 59. Ability of dC2_049 and dC2_050 to inhibit αCGRP-mediated cAMP production at the CGRPR in COS-7 cells. Concentration-response curves of αCGRP are concentration-dependently right shifted by **a** dC2_049 or **b** dC2_050 binders at COS-7 cells transiently expressing CGRPR. Data shown are mean ± s.e.m., n=4 biological replicates. Data fit to the Gaddam-Schild equation in Prism to determine functional estimates for dC2_049 are pA_2 of 8.30 ± 0.29 (5.05 nM) and slope of 1.36 ± 0.36 and for dC2_050 pA_2 of 8.33 ± 0.19 (4.72 nM) and slope of 1.01 ± 0.18.

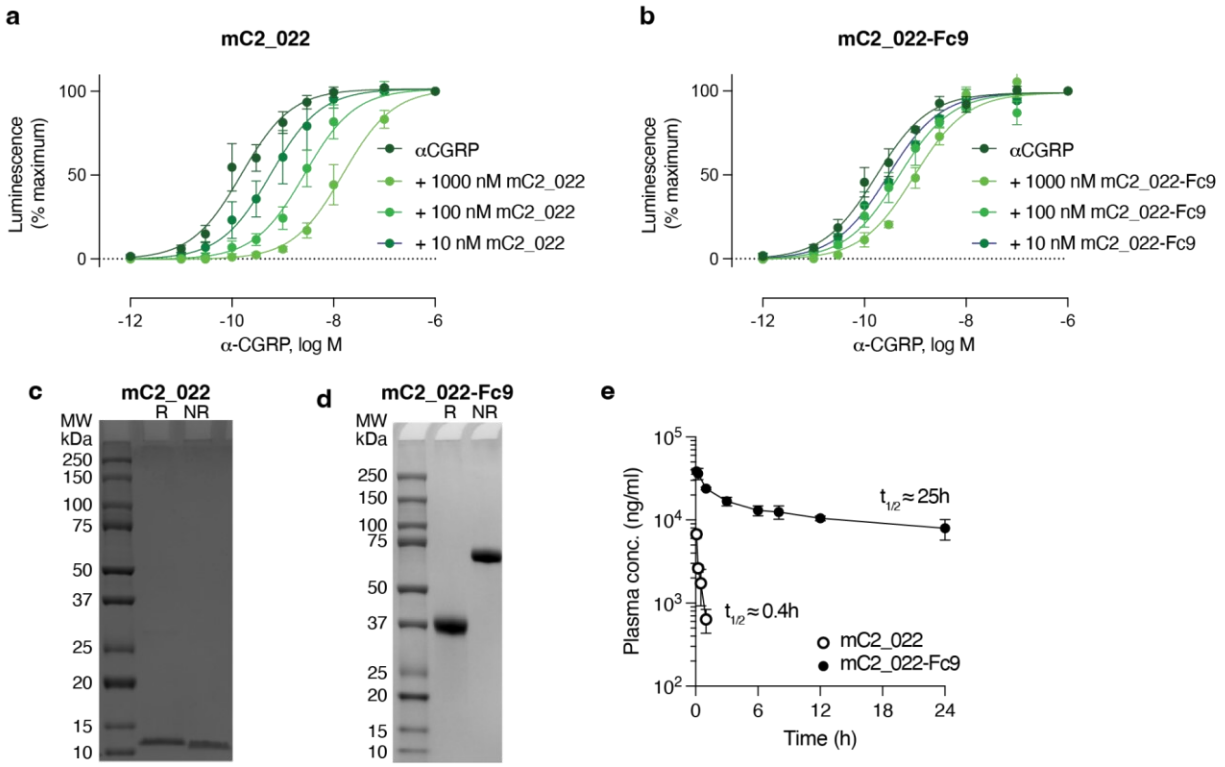

Supplementary Fig. 60. Pharmacokinetics study of the mC2_022 miniprotein CGRPR antagonist. a, b Concentration-response curves (Schild plots) of αCGRP with the unmodified miniprotein mC2_022 (a) and the Fc-fused miniprotein mC2_022-Fc9 (b) in CHO-K1/CRE/CGRPR cells. Functional estimates (mean ± s.e.m.,, n=4 biological replicates (mC2_022) or n=3 biological replicates (mC2_022-Fc9) are *p*A2 = 8.5 ± 0.4 (3.4 nM) and slope 0.90 ± 0.34 for mC2_022, and *p*A2 = 7.4 ± 0.2 (43 nM) and slope 0.55 ± 0.11 for mC2_022-Fc. **c** SDS-PAGE of mC2_022 and **d** mC2-022-FC9, R: reduced, NR: non-reduced. Shown are uncropped gels. **e** Plasma concentrations of the cM2_022 (open symbols) and cM2_022-Fc9 (closed symbols) were measured in mice following a single intravenous dose of 3 mg/kg. Sample sizes per time point (mean ± s.e.m.) were as follows — Fc-fused: 0.083 h (n=3 mice), 0.25 h (n=4 mice), 1 h (n=3 mice), 3 h (n=4 mice), 6 h (n=3 mice), 8 h (n=4 mice), 12 h (n=3 mice), 24 h (n=4 mice); Unmodified: 0.083 h (n=4 mice), 0.25 h (n=4 mice), 0.5 h (n=3 mice), 1 h (n=3 mice). The unmodified miniprotein exhibited rapid systemic clearance, with plasma levels declining sharply and approaching baseline by 6 hours post-dose; its estimated half-life was 0.4 hours. In contrast, the Fc-fused miniprotein demonstrated prolonged systemic exposure, with detectable plasma levels throughout the sampling period and an estimated half-life of 25 hours.

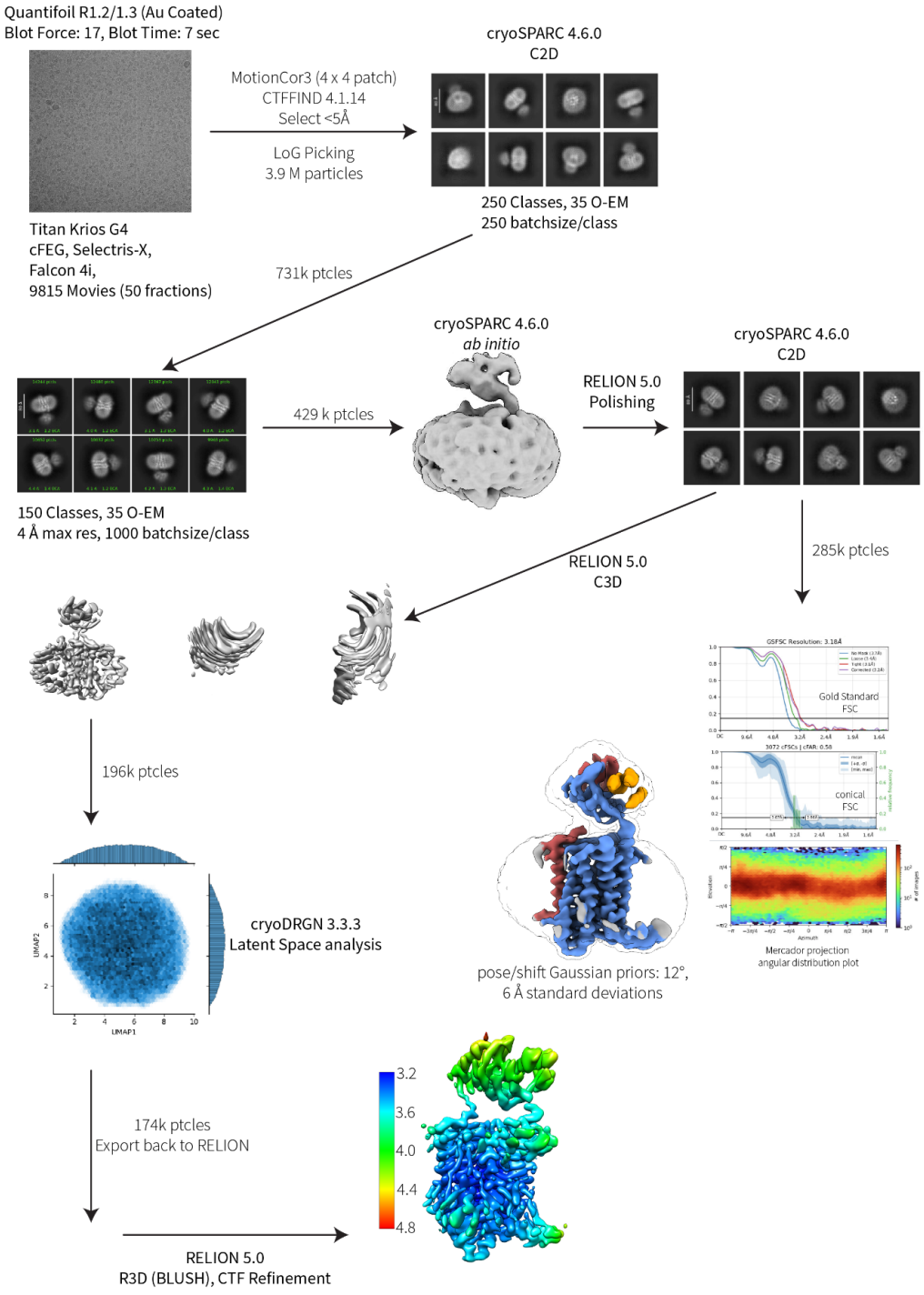

Supplementary Fig. 61. Processing overview for dC2_049/CGRPR. The representative micrograph has a field of view of 307.2 nm^2.

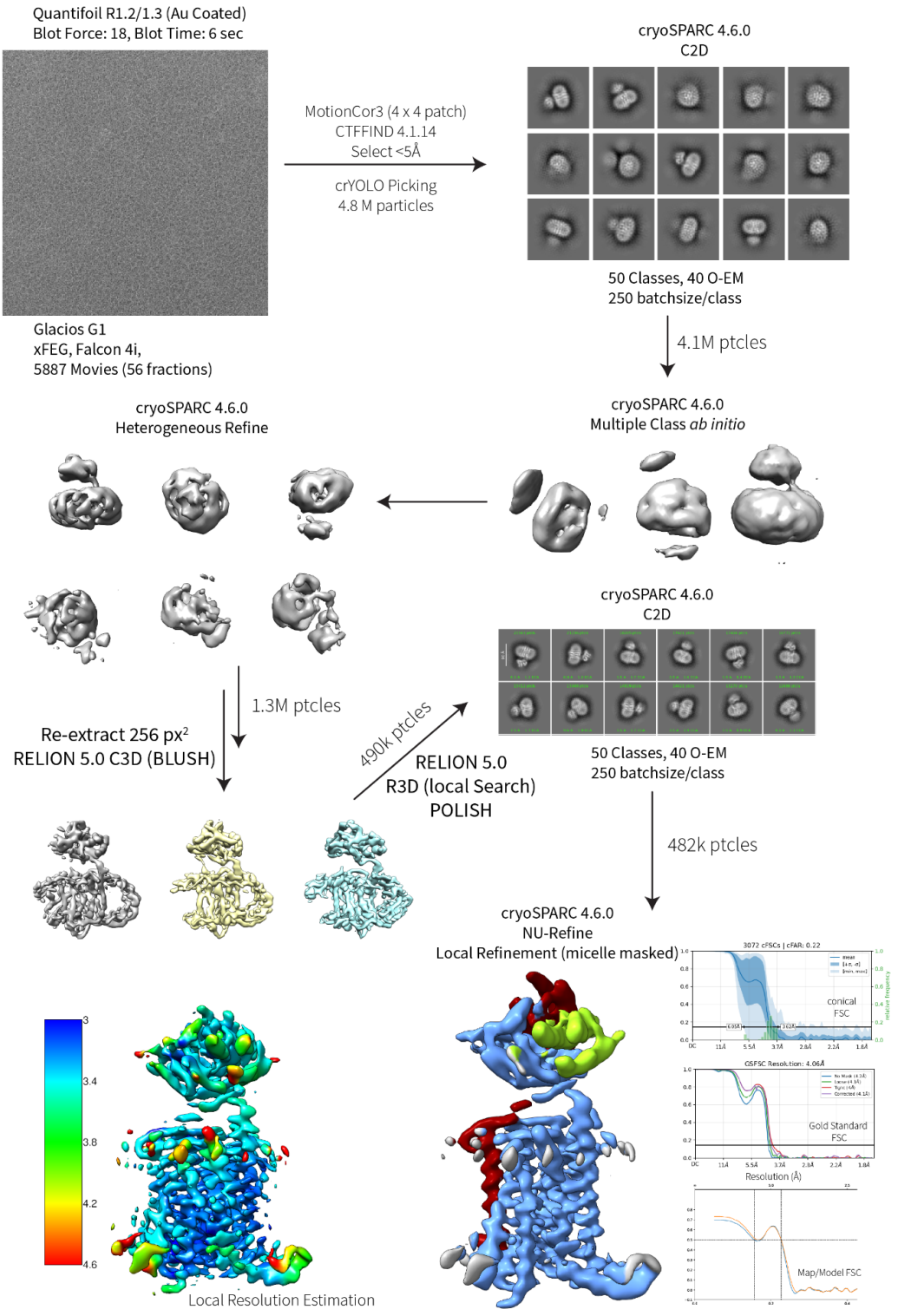

Supplementary Fig. 62. Processing overview for dC2_050/CGRPR. The representative micrograph has a field of view of 307.2 nm^2.

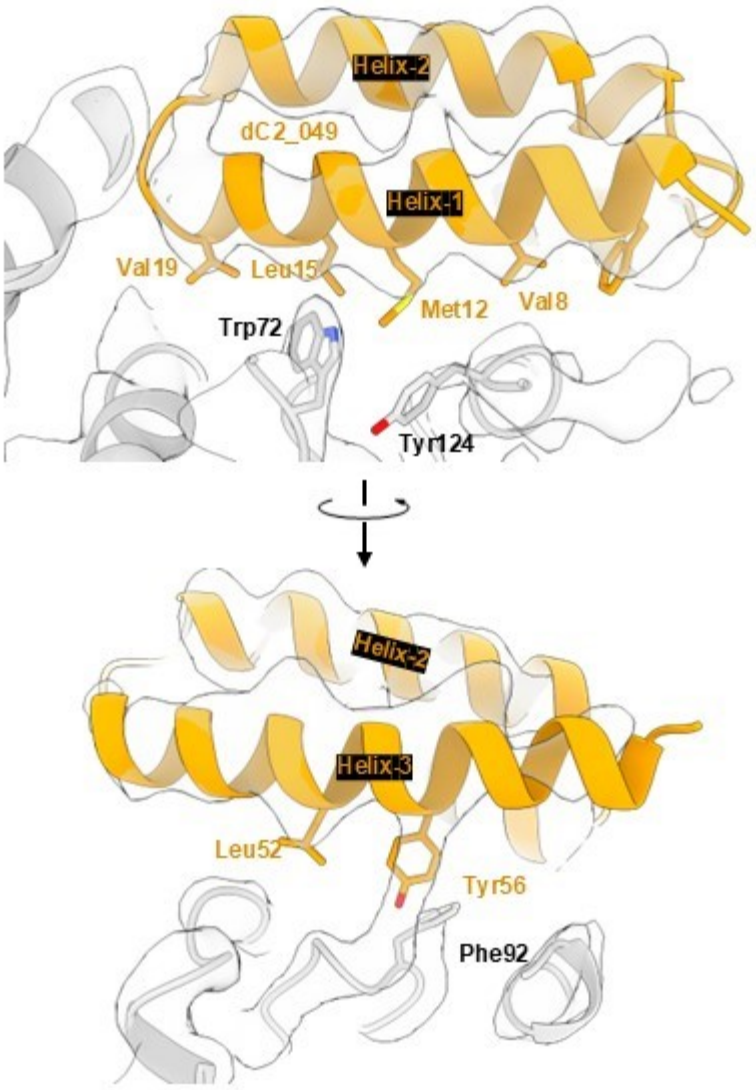

Supplementary Fig. 63. Map to model figures showing the miniprotein dC2_049 and receptor interface with selected residues labeled. The map, dC2_049, and CGRPR, are depicted as translucent, gold, and gray, respectively.

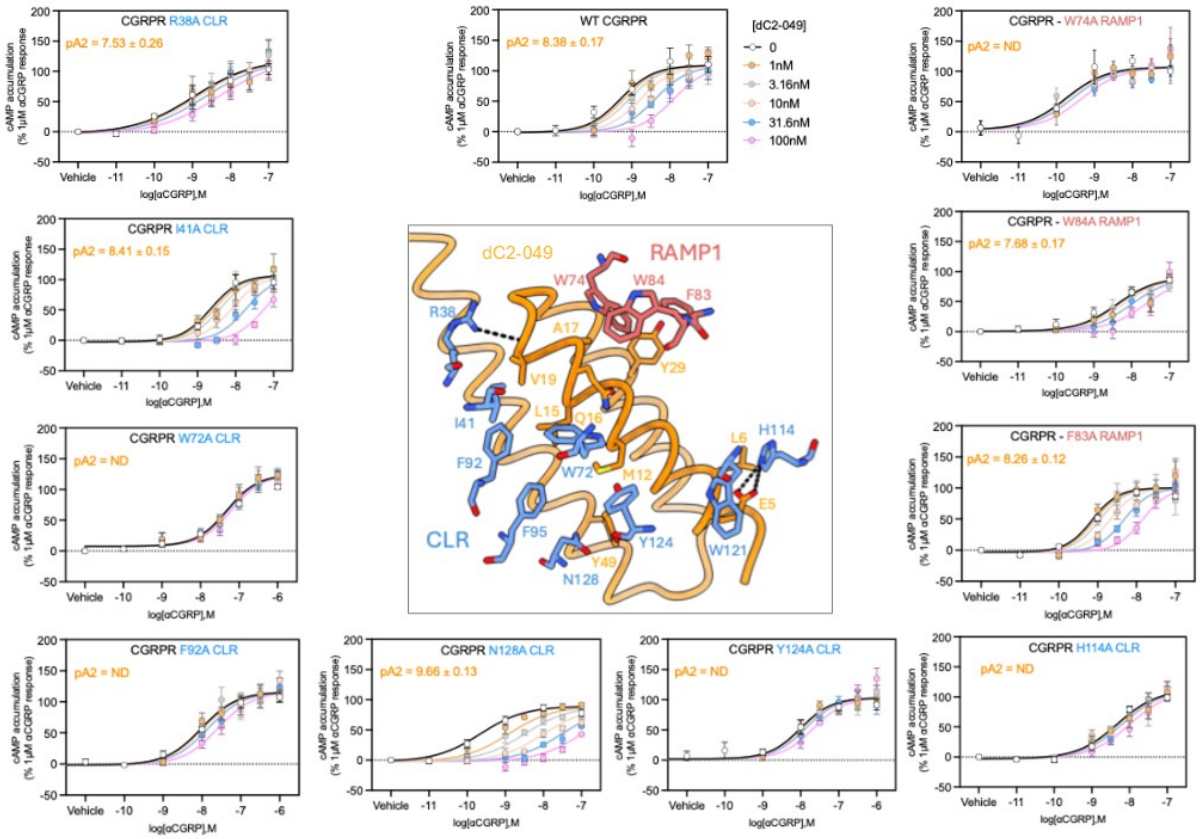

Supplementary Fig. 64. CGRPR mutagenesis to confirm binding of dC2_049. Middle Panel: Residues within CLR (blue) and RAMP1 (coral) that interact or are in close proximity to dC2_049 (orange). Surrounding panels: The ability of dC2_049 to inhibit cAMP accumulation mediated by αCGRP at the WT CGRPR (top middle) and alanine mutants of interacting residues in RAMP1 or CLR. Data are the mean ± s.e.m, n=5 or n=6 biological replicates (see Source data for exact n values). Data fit to a Gaddam-Schild equation in Prism to determine functional estimates of affinity for dC2_049 at each receptor (*p*A2). ND indicates where a confident pA2 value could not be obtained due to no detectable inhibition or inhibition only at the highest concentration of dC2_049 assessed. F95A and Y124A were also assessed but only mediated responses to αCGRP at the highest concentration assessed (1 μM) and therefore quantification of the inhibition by dC2_049 could not be determined.

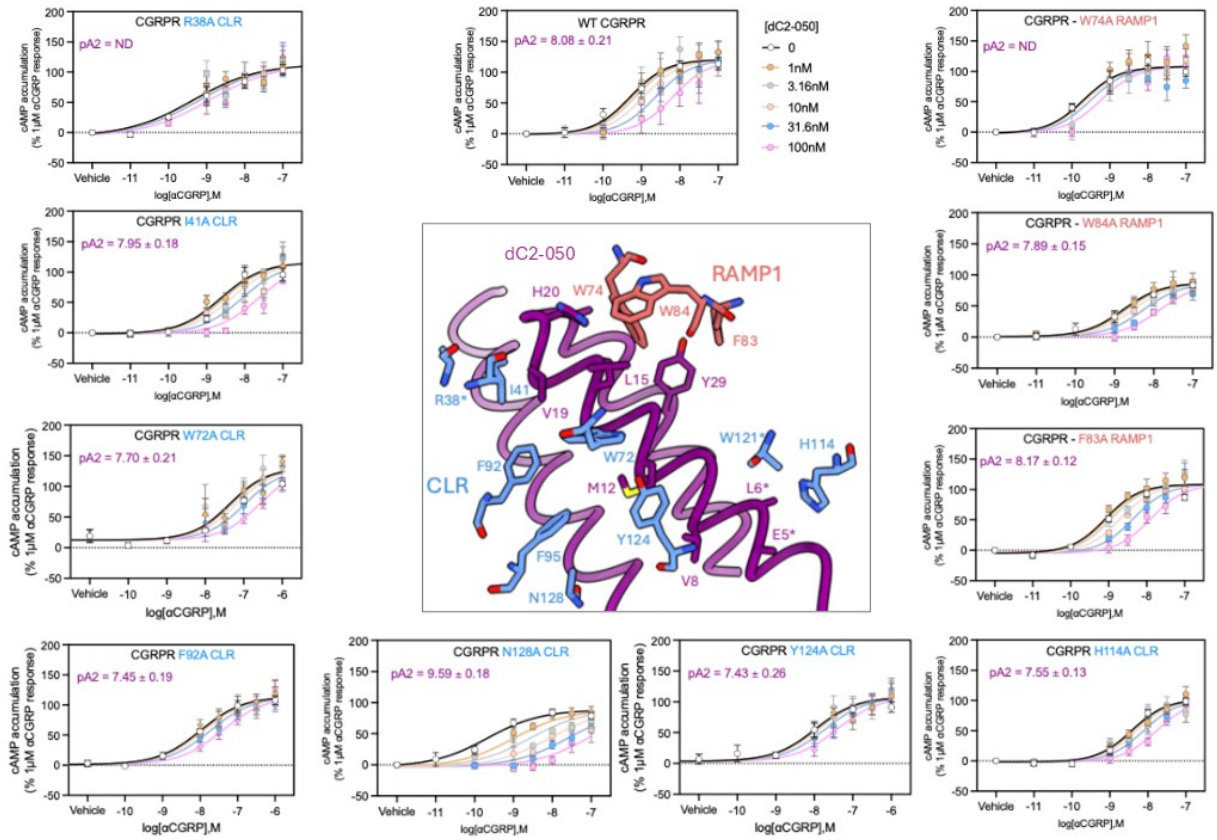

Supplementary Fig. 65. CGRPR mutagenesis to confirm binding of dC2_050. Middle Panel: Residues within CLR (blue) and RAMP1 (coral) that interact or are in close proximity to dC2_050 (purple). Side chains for residues with a star are not visible as they were stubbed in the model deposited in the pdb due to weak density in the cryo-EM map. Surrounding panels: The ability of dC2_050 to inhibit cAMP accumulation mediated by αCGRP at the WT CGRPR (top middle) and alanine mutants of interacting residues in RAMP1 or CLR. Data are the mean ± s.e.m., n=5 or n=6 biological replicates (see Source data for exact n values). Data fit to a Gaddam-Schild equation in Prism to determine functional estimates of affinity for dC2_050 at each receptor (*p*A2). ND indicates where a confident *p*A2 value could not be obtained due to no detectable inhibition or inhibition only at the highest concentration of dC2_050 assessed. F95A and Y124A were also assessed but only mediated responses to αCGRP at the highest concentration assessed (1 μM) and therefore quantification of inhibition by dC2_050 could not be determined.

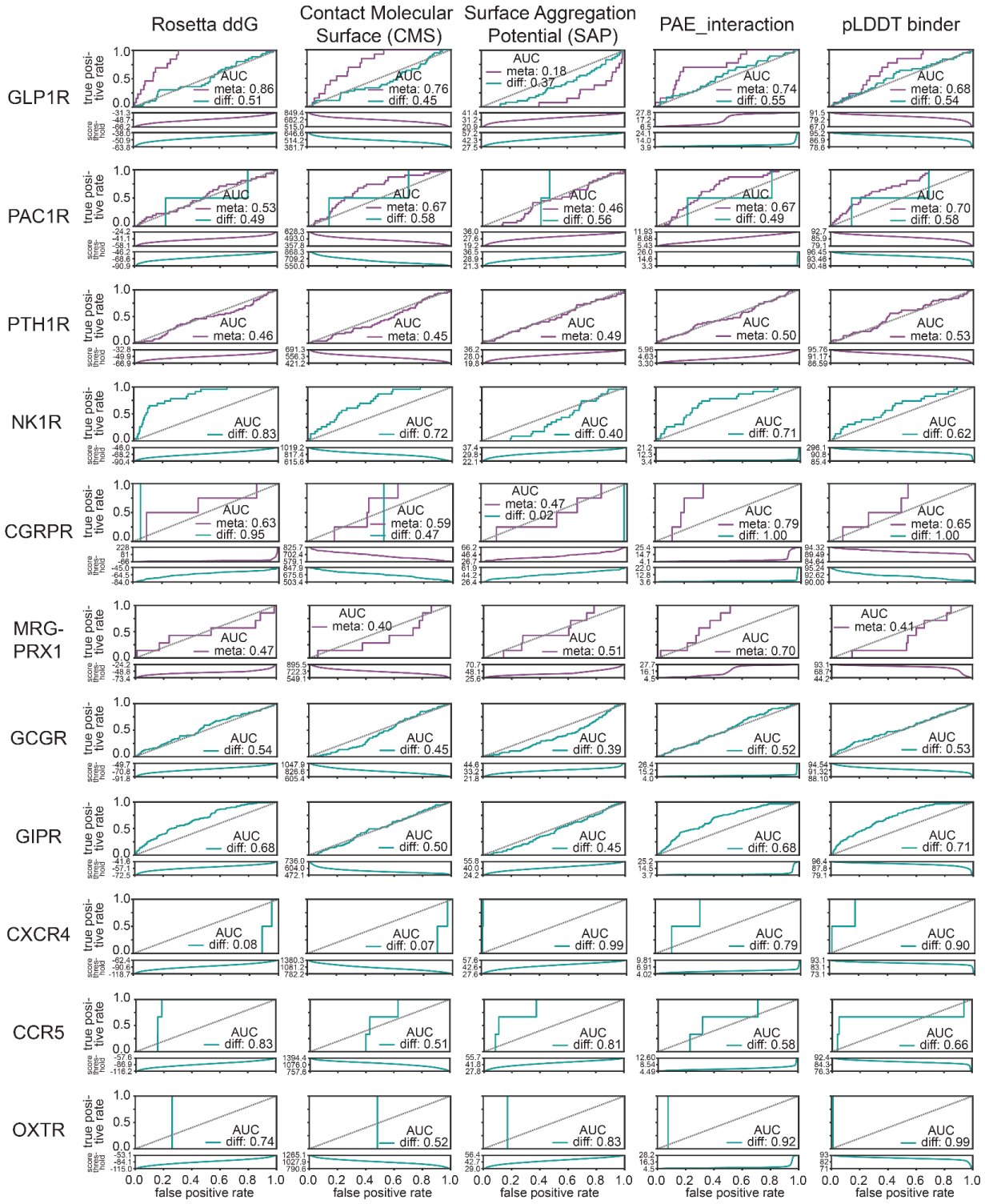

Supplementary Fig. 66. Retrospective analysis of computational scoring metrics across receptor targets and design methods. Receiver Operating Characteristic (ROC) curves comparing the ability of each computational metric to discriminate experimentally confirmed binders from non-binders across the design sets tested. Each column shows a different metric-Rosetta interface ΔΔG (ddG), contact molecular surface (CMS), surface aggregation propensity (SAP), AlphaFold-Multimer predicted aligned error at the

interface (PAE_interaction), and AlphaFold average per-residue pLDDT of the binder chain (pLDDT binder). Each row corresponds to a distinct receptor target. Within each panel, curves are shown separately for MetaGen (purple) and RFdiffusion (teal) design methods, and the legend reports the corresponding area under the ROC curve (AUC). Hit identification came from functional assays for MRGPRX1, OXTR, CXCR4, CCR5, and CGRPR, from yeast cell surface display for GLP1R, SPR for PTH1R, and yeast cell surface display and SPR for GIPR, GCGR, and PAC1R.

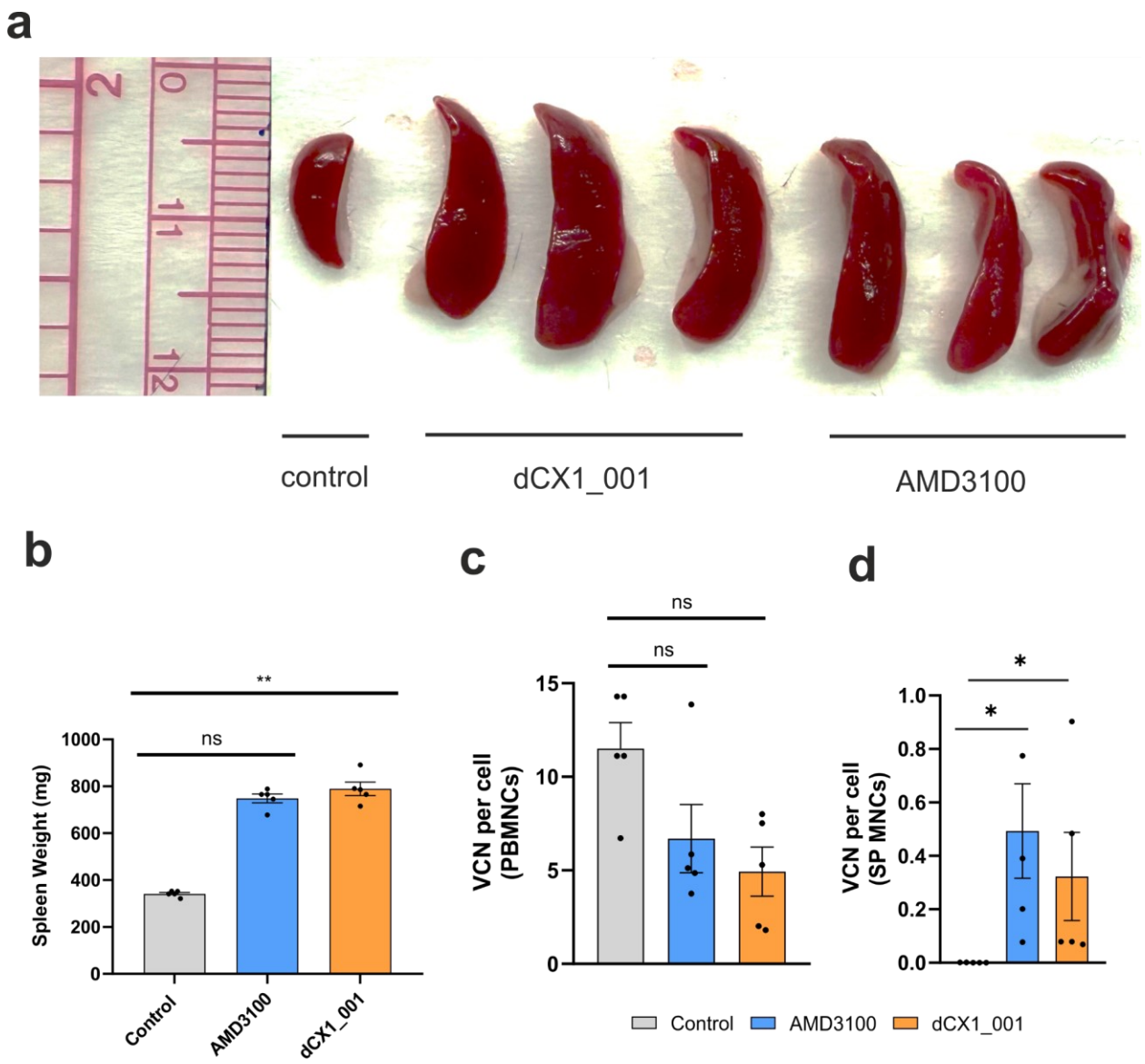

Supplementary Fig. 67. Mobilization of HSPCs by dCX1_001 and AMD3100. a The splenomegaly was observed at 72 h after PBS, AMD3100, or dCX1_001 injection, consistent with mobilized cells returning to the spleen. **b** Spleen weight after mobilization at 72 h after PBS, AMD3100, or dCX1_001 injection showed 2-fold increase in spleen weight. Spleen size and spleen weight increased at 72 h after mobilization, consistent with rehoming of hematopoietic cells. Each symbol represents an individual animal. Data represent mean ± s.e.m., n=5 mice per group. Statistical analysis was performed using two-sided Kruskal Wallis followed Dunn's multiple comparisons test. Asterisks denote significant values, $^{**}p \leq 0.01$, ns, not significant. **c-d** *In vivo* HSPC transduction after AMD3100 or dCX1_001 mobilization. Vector copy number per cell in **c** peripheral blood mononuclear cells (PBMCs) and **d** spleen mononuclear cells (MNCs). Each symbol represents an individual animal. Data are mean ± s.e.m., n=5 mice per group. Statistical analysis was performed using two-sided Kruskal Wallis followed Dunn's multiple comparisons test. Asterisks denote significant values, $^{*}p \leq 0.05$, ns, not significant. Exact *p* values and detailed statistical analysis are provided in the Source data. Statistics were performed only for indicated comparisons; other comparisons were not analyzed statistically.

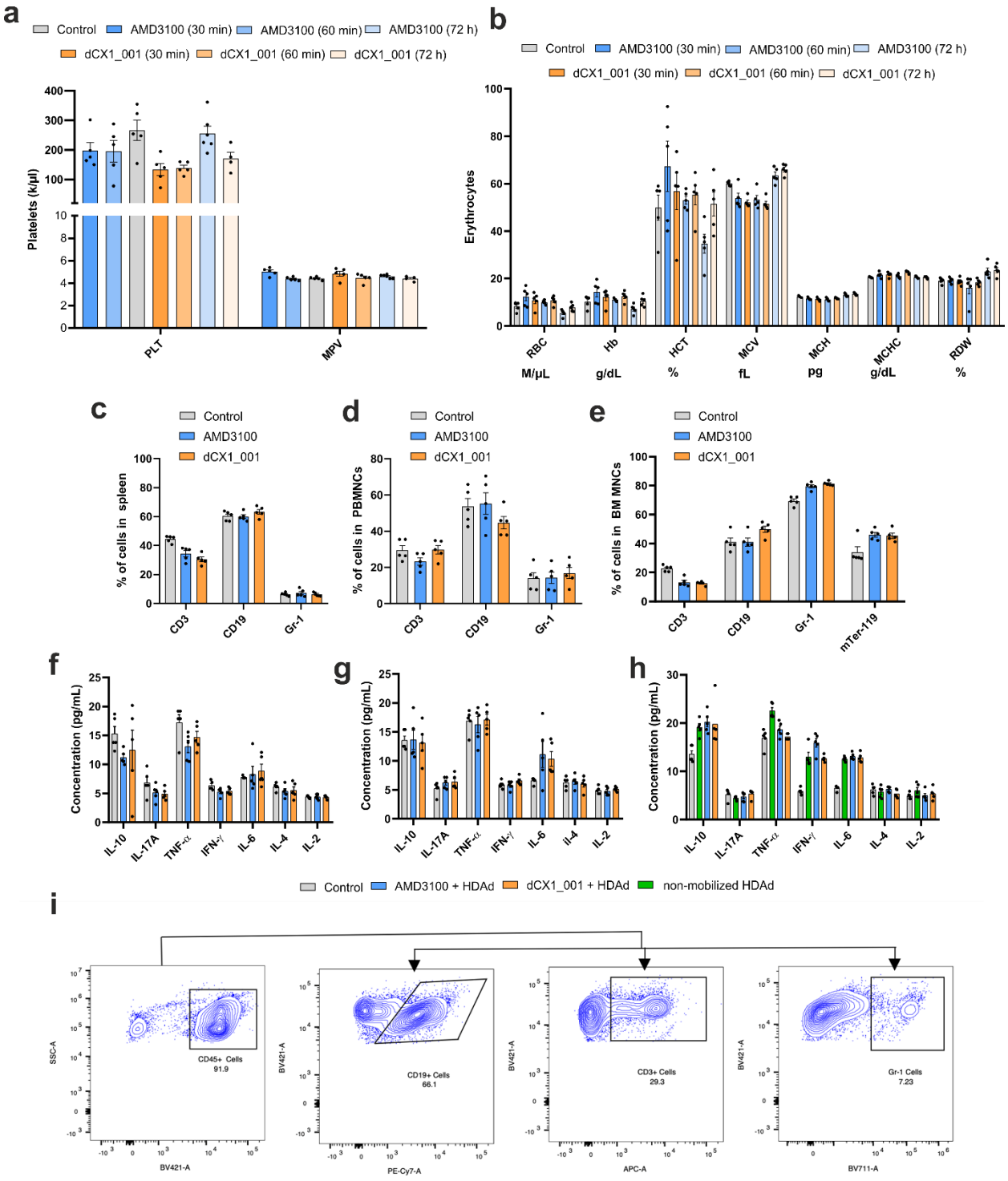

Supplementary Fig. 68. Hematological parameters after mobilization with dCX1_001 and AMD3100. **a** Blood samples were taken from mice injected subcutaneously with PBS (control), AMD3100, or dCX1_001 at 30 min, 60 min and 72 h and their effects on platelets analyzed on a HemaVet 950FS. Each dot represents an individual animal. Error bars represent mean ± s.e.m., n=4, n=5 or n=6, mice per group (see Source data for exact n mice). dCX1_001 does not cause changes in platelets. Mean platelet volume (MVP). **b** Erythroid parameters at 30 min, 60 min, and 72 h after PBS (control), AMD3100 or dCX1_001 injection. dCX1_001 does not cause hemolysis and has no effect on erythropoiesis. Red blood cells RBC);

Hemoglobin (Hb); Hematocrit (HCT); mean corpuscular volume (MCV); mean corpuscular hemoglobin (MCH); mean corpuscular hemoglobin concentration (MCHC); Red cell distribution width (RDW). Each symbol represents an individual animal. Error bars represent mean ± s.e.m., n=5 mice per group. Effect of mobilization on cell lineage composition in **c** spleen mononuclear cells **d** peripheral blood mononuclear cells (PBMCs) and **e** bone marrow (BM) mononuclear cells (MNCs) 72 h after injection**.** Analyzed were T-cells (CD3+), B-cells (CD19+), granulocytes (Gr-1+) and erythroid bone marrow cells (Ter-119+). No effect of AMD3100 or dCX1_001 mobilization on PBMC and spleen lineages was observed. Each symbol represents an individual animal. Error bars represent mean ± s.e.m, n=5 mice per group. Serum cytokine levels at **f** 1 h and **g** 6 h after mobilization or **h** after mobilization/HDAd injection measured using cytometric bead array. Mobilization with dCX1_001 or AMD3100 does not trigger elevated cytokines. Cytokines are released upon uptake of HDAd by mobilized cells, neutrophiles and lymphocytes. Each symbol represents an individual animal. Error bars represent mean ± s.e.m., n=5 mice per group. i Representative gating strategy used to gate CD19-B cells, CD3-T cells and Gr-1 macrophage lineage cells. PBMNCs were initially gated based on forward scatter (FSC) and side scatter (SSC) (P1). $CD45^+$ cells were then selected, from which $CD3^+$ T cells, $CD19^+$ B cells, and $Gr\text{-}1^+$ cells were analyzed. This gating strategy was used for **c-e**.

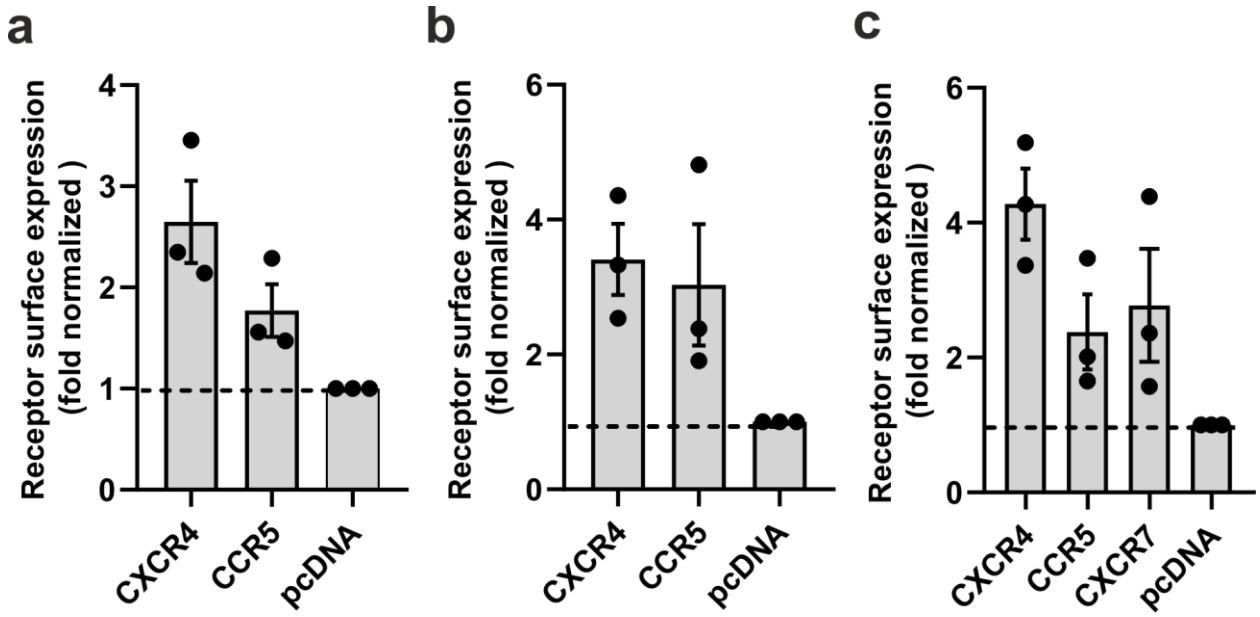

Supplementary Fig. 69. Surface expression of CXCR4, CCR5 and CXCR7. A representative example of the receptor surface expression corresponding to **a** cAMP, **b** G protein dissociation and **c** β-arrestin-1 recruitment assay which was quantified and normalized relative to mock-transfected cells. Data are shown as mean ± s.e.m., n=3 biological replicates.

Supplementary Table 1. Z-prime values for OPS-RD for seven GFP-fused GPCRs.

Target	Z prime
CXCR4	0.85
SMO	0.63
MRGPRX2	0.49
MC4R	0.47
LPAR1	0.43
PAR2	0.29
FZD4	0.13

Z prime values were computed using simulated averaging over 100 single-cell replicates per binder. Positive controls (C5-oligomerized, 0.7 nM KDEL-fused anti-GFP-nanobody) and negative controls (KDEL-fused GFP-miniprotein) were used.

Supplementary Table 2. Binding data of PAC1R miniprotein binders identified by yeast display.

Analyte	k_a ($M^{-1}s^{-1}$)	k_d (s^{-1})	K_D (M)	R_{max} (RU)
mPA1_005	1.4E+06	1.7E-01	1.2E-07	66
mPA1_006	7.3E+05	9.0E-02	1.2E-07	66
mPA1_007	1.0E+06	2.5E-01	2.5E-07	73
mPA1_008	2.6E+06	2.4E-01	9.3E-08	80
mPA1_010	1.5E+05	1.9E-02	1.3E-07	76
mPA1_011	3.3E+05	2.9E-01	8.9E-07	74
mPA1_013	3.6E+03	3.6E-03	1.0E-06	75
mPA1_014	1.4E+06	9.5E-02	6.7E-08	79
mPA1_015	1.4E+06	3.5E-02	2.6E-08	65
mPA1_016	5.6E+05	1.2E-02	2.2E-08	72
mPA1_017	1.2E+06	7.4E-02	6.3E-08	72
mPA1_019	2.4E+09	1.8E+01	7.3E-09	77
mPA1_022	1.2E+06	1.1E-01	9.2E-08	80
mPA1_023	3.0E+05	5.1E-04	1.7E-09	n.a
mPA1_025	5.5E+05	4.7E-01	8.6E-07	55
mPA1_027	1.0E+06	7.5E-02	7.4E-08	69
mPA1_029	2.9E+05	2.6E-01	9.0E-07	46
mPA1_030	4.6E+03	2.0E-02	4.4E-06	70
mPA1_032	1.1E+06	1.1E-01	1.0E-07	76
mPA1_033	5.3E+05	8.7E-02	1.7E-07	80
mPA1_036	1.2E+04	1.6E-02	1.4E-06	63
mPA1_038	9.7E+05	2.8E-02	2.9E-08	83
mPA1_040	4.5E+05	1.1E-02	2.5E-08	70
mPA1_043	2.8E+05	1.4E-02	4.9E-08	66
mPA1_044	5.7E+05	3.8E-02	6.7E-08	66
mPA1_046	1.3E+05	6.0E-02	4.7E-07	97
mPA1_048	3.8E+05	1.2E-01	3.2E-07	73
mPA1_051	1.3E+06	1.2E-01	9.4E-08	74
mPA1_052	1.0E+06	3.9E-02	3.8E-08	73
mPA1_053	6.5E+05	1.4E-01	2.1E-07	67
mPA1_055	4.7E+05	1.3E-02	2.7E-08	71
mPA1_056	3.3E+05	2.9E-02	9.0E-08	75

SPR measurements were carried out against PAC1R soluble ECD in a single experiment (n=1). n.a. = not applicable

Supplementary Table 3. Binding data of PAC1R miniprotein binders identified by OPS-RD.

Analyte	k_a (M^{-1s-1})	k_d (s^{-1})	K_D (M)	R_{max} (RU)
mPA1_006	5.6E+05	2.4E-02	4.2E-08	63.9
mPA1_014	1.3E+06	7.2E-02	5.5E-08	69.0
mPA1_022	1.1E+06	5.9E-02	5.3E-08	71.3
mPA1_023	1.5E+05	1.4E-03	8.8E-09	68.0
mPA1_032	1.0E+04	2.5E-04	2.4E-08	81.6
mPA1_033	1.6E+04	4.2E-06	2.7E-10	69.7
mPA1_044	4.6E+05	1.5E-02	3.1E-08	60.0
mPA1_059	6.6E+05	8.5E-03	1.3E-08	54.2
mPA1_060	7.4E+04	1.4E-02	1.9E-07	44.3
mPA1_061	8.6E+03	5.0E-03	5.8E-07	19.6
mPA1_062	1.8E+06	5.1E-02	2.8E-08	63.1
mPA1_064	1.2E+04	7.6E-02	6.2E-06	65.0
mPA1_068	9.9E+03	1.8E-01	1.8E-05	n.a.
mPA1_071	1.1E+04	3.1E-02	2.9E-06	35.0
mPA1_072	8.7E+03	9.2E-02	1.1E-05	n.a.
mPA1_073	4.4E+05	5.8E-02	1.3E-07	60.8
mPA1_074	2.1E+03	1.0E-01	5.0E-05	n.a.
mPA1_076	1.5E+04	1.1E-02	7.9E-07	66.3
mPA1_078	4.1E+04	2.0E-01	4.8E-06	57.2
mPA1_079	1.2E+06	2.2E-01	1.8E-07	74.6
mPA1_080	2.0E+05	1.2E-01	5.8E-07	67.0
mPA1_084	2.2E+03	1.6E-01	7.2E-05	n.a.
mPA1_086	1.1E+04	3.1E-02	3.0E-06	29.0
mPA1_087	9.5E+04	6.4E-02	6.7E-07	65.5
mPA1_088	1.2E+06	1.9E-01	1.6E-07	70.0
mPA1_089	1.5E+05	1.9E-01	1.3E-06	n.a
mPA1_090	1.9E+04	8.7E-01	4.7E-05	n.a.
mPA1_092	3.5E+05	1.9E-01	5.2E-07	61.1
mPA1_093	1.1E+03	7.0E-01	6.3E-04	2147.4
mPA1_097	1.5E+04	3.4E-01	2.3E-05	n.a.
mPA1_098	2.0E+06	1.4E+01	6.9E-06	n.a.
mPA1_104	3.9E+05	4.4E-01	1.1E-06	61.7
mPA1_105	5.0E+03	9.7E-01	2.0E-04	65.0
mPA1_106	4.3E+05	9.6E-02	2.3E-07	57.8
mPA1_107	5.9E+03	4.1E-01	7.0E-05	n.a.
mPA1_109	3.5E+05	1.3E-01	3.8E-07	62.8
mPA1_110	5.1E+05	3.6E-01	7.0E-07	54.3
mPA1_111	2.9E+04	2.8E-03	9.6E-08	56.0

mPA1_113	5.0E+02	6.9E-02	1.4E-04	n.a.
mPA1_114	2.8E+05	1.6E-01	5.8E-07	54.0
mPA1_115	4.9E+02	4.3E-01	8.7E-04	995.5
mPA1_116	7.7E+05	4.3E-01	5.5E-07	49.2
mPA1_117	1.9E+05	1.2E+00	6.5E-06	65.0
mPA1_122	3.5E+04	3.1E-03	8.8E-08	75.6
mPA1_123	1.1E+05	1.3E-01	1.2E-06	n.a.
mPA1_124	5.5E+03	6.6E-02	1.2E-05	n.a.
mPA1_127	8.3E+04	2.1E-01	2.5E-06	n.a.
mPA1_128	9.5E+01	2.6E-03	2.7E-05	n.a.
mPA1_129	2.5E+03	1.0E+00	4.3E-04	6196.1
mPA1_132	2.8E+05	1.1E+00	3.9E-06	n.a.
mPA1_133	3.7E+04	2.5E-01	6.8E-06	n.a.
mPA1_135	6.1E+03	2.2E-06	3.6E-10	81.5

SPR measurements were carried out against PAC1R soluble ECD in a single experiment (n=1). n.a. = not applicable

Supplementary Table 4. Pharmacological data of MRGPRX1 binders

Ligand	Hill slope	Potency EC_{50} (M)	$p(EC_{50})$	E_{max} (%)
mM1_011	2.7	3.1×10^{-6}	5.5	101
mM1_034	2.7 ± 0.1	$1.0 \pm 0.1 \times 10^{-6}$	6.0 ± 0.0	99 ± 1
mM1_059	1.8	1.3×10^{-6}	5.9	117
mM1_060	11.0 ± 2.8	$1.4 \pm 0.2\ 10^{-6}$	5.9 ± 0.1	22 ± 2
mM1_063	2.1	3.2×10^{-6}	5.5	139
mM1_068	2.3 ± 0.1	$3.9 \pm 0.3 \times 10^{-7}$	6.4 ± 0.0	96 ± 2
mM1_084	2.9	3.9×10^{-6}	5.4	78
mM1_034_F12W_Y27F	2.6 ± 0.6	$4.2 \pm 0.7 \times 10^{-8}$	7.4 ± 0.1	85 ± 6
mM1_034_F12W_A58M	2.5 ± 0.4	$1.1 \pm 0.2 \times 10^{-7}$	7.0 ± 0.1	68 ± 3

Data are shown as mean ± s.e.m., n=3 biological replicates (mM1_060, mM1_068), n=4 biological replicates (mM1_034, mM1_034_F12W_27F), n=5 biological replicates (mM1_034_F12W_A58M) and mean of technical replicates from a single biological replicate (mM1_011, mM1_059, mM1_063, mM1_084). The EC_{50} of the native BAM (8-22) in the calcium mobilization assay was $3.0 \pm 0.2 \times 10^{-9}$ (M) (pEC$_{50}$ 8.5 ± 0.1, mean ± s.e.m., n=5 biological replicates).

Supplementary Table 5. Pharmacological data of NK1R agonists

Ligand	Potency EC_{50} (M)	$p(EC_{50})$	E_{max} (%)
dNK1_019	2.3 ± 0.4 x 10^{-9}	8.7 ± 0.1	27 ± 3
dNK1_022	2.3 ± 0.1 x 10^{-9}	8.7 ± 0.1	25 ± 2
dNK1_023	1.1 ± 0.1 x 10^{-8}	7.9 ± 0.1	24 ± 2
dNK1_024	6.6 ± 0.9 x 10^{-9}	8.2 ± 0.1	36 ± 4
dNK1_027	2.7 ± 0.5 x 10^{-9}	8.6 ± 0.1	70 ± 6
dNK1_028	1.4 ± 0.1 x 10^{-8}	8.0 ± 0.1	63 ± 5
dNK1_032	5.3 ± 0.5 x 10^{-9}	8.3 ± 0.1	45 ± 3
dNK1_035	2.4 ± 0.3 x 10^{-9}	8.6 ± 0.1	66 ± 3
dNK1_036	6.9 ± 1.2 x 10^{-9}	8.2 ± 0.1	37 ± 3
dNK1_037	1.1 ± 0.1 x 10^{-9}	8.9 ± 0.1	81 ± 7
dNK1_038	5.7 ± 0.8 x 10^{-9}	8.3 ± 0.1	60 ± 5
dNK1_039	6.0 ± 0.8 x 10^{-9}	8.3 ± 0.1	54 ± 6
dNK1_040	2.8 ± 0.4 x 10^{-9}	8.6 ± 0.1	51 ± 5
dNK1_042	3.0 ± 0.5 x 10^{-9}	8.5 ± 0.1	44 ± 6
dNK1_045	1.0 ± 0.1 x 10^{-9}	9.0 ± 0.1	35 ± 4
dNK1_054	1.6 ± 0.2 x 10^{-9}	8.8 ± 0.1	74 ± 8
dNK1_062	3.8 ± 1.5 x 10^{-8}	7.5 ± 0.1	27 ± 3
dNK1_069	5.2 ± 0.4 x 10^{-9}	8.3 ± 0.1	74 ± 3
dNK1_070	1.0 ± 0.1 x 10^{-9}	8.9 ± 0.1	91 ± 9
dNK1_071	2.3 x 10^{-7}	6.6	24

Data are shown as mean ± s.e.m., n=3 biological replicates except for dNK1_071, mean, n=2 biological replicates. The EC_{50} of the native Substance P in the cAMP assay was 0.6 ± 0.3 x 10^{-9} (M) (pEC_{50} 9.4 ± 0.2, mean ± s.e.m., n=3 biological replicates).

Supplementary Table 6. Contact list between MRGPRX1 and adducts at distance of < 5 Å.

BW Numbering	MRGPRX1	mM1_068	mM1_060
N-term	21(THR).		1(MET).
			4(ALA).
			5(PHE).
			30(MET).
			36(ILE).
			37(LYS).
			38(TYR).
N-term	22(LEU).		35(PHE).
			36(ILE).
			37(LYS).
N-term	23(CYS).		35(PHE).
1.32	27(THR).		35(PHE).
2.60	82(TYR).	45(PHE).	32(THR).
		48(PRO).	33(ASP).
			34(PRO).
			35(PHE).
2.64	86(SER).	52(LEU).	35(PHE).
ECL1	91(PRO).	11(LEU).	
ECL1	92(HIS).	8(GLU).	29(LEU).
		11(LEU).	32(THR).
		42(TYR).	33(ASP).
			36(ILE).
			44(GLU).
ECL1	93(THR).	42(TYR).	
3.25	95(SER).	42(TYR).	32(THR).
			33(ASP).
3.26	96(LYS).	42(TYR).	
3.28	98(LEU).	45(PHE).	
3.29	99(TYR).	41(LYS).	32(THR).
3.32	102(MET).	45(PHE).	
4.60	157(GLU).		28(LYS).
ECL2	167(GLY).	39(HIS).	25(TRP).
			48(LEU).
			49(ALA).
ECL2	168(ALA).		21(ARG).
			25(TRP).
			48(LEU).
5.32	169(ASP).	39(HIS).	21(ARG).
			25(TRP).
5.33	170(SER).	35(LYS).	21(ARG).
		36(ASP).	24(TYR).
		37(LYS).	25(TRP).

		38(ARG).	
		39(HIS).	
5.36	173(CYS).	38(ARG).	24(TYR).
		39(HIS).	25(TRP).
5.37	174(GLN).	38(ARG).	24(TYR).
5.40	177(ASP).	38(ARG).	24(TYR).
		41(LYS).	28(LYS).
6.54	235(GLN).		31(LEU).
6.55	236(PHE).	41(LYS).	31(LEU).
		44(LEU).	
		45(PHE).	
6.56	237(PHE).	38(ARG).	
6.58	239(PHE).		27(ARG).
6.59	240(LEU).	37(LYS).	24(TYR).
		38(ARG).	27(ARG).
		41(LYS).	28(LYS).
			31(LEU).
6.60	241(TRP).	38(ARG).	24(TYR).
6.61	242(ILE).		27(ARG).
ECL3	246(ARG).	30(TRP).	1(MET).
			2(ASN).
7.31	250(PHE).	44(LEU).	1(MET).
		47(TYR).	27(ARG).
		48(PRO).	30(MET).
7.32	251(CYS).		1(MET).
7.35	254(HIS).	44(LEU).	29(LEU).
			31(LEU).
			34(PRO).
7.36	255(LEU).		35(PHE).
7.39	258(ILE).		34(PRO).

Interactions determined using the contact program of the CCP4 suite[5]. BW - Ballesteros-Weinstein designation.

Supplementary Table 7. Pharmacological data of CXCR4, CCR5 and OXTR binders.

Ligand	**Potency IC_{50} (M)**	***p*(IC_{50})**
dCX1_001	$2.4 \pm 0.5 \times 10^{-8}$	7.6 ± 0.1
dCX1_002	$1.2 \pm 0.3 \times 10^{-7}$	6.9 ± 0.1
dCX1_003	$> 1 \times 10^{-5}$	> 5.0
dCX1_004	$> 1 \times 10^{-5}$	> 5.0
dCX1_005	$> 1 \times 10^{-5}$	> 5.0
dCC1_005*	$5.5 \pm 1.5 \times 10^{-7}$	6.3 ± 0.1
dCC1_042*	$1.5 \pm 0.3 \times 10^{-6}$	5.9 ± 0.2
dCX1_001_maxibinder	$9.4 \pm 1.2 \times 10^{-9}$	8.0 ± 0.1
dOX1_003	$3.3 \pm 0.8 \times 10^{-7}$	6.5 ± 0.1
Ligand	**Potency EC_{50} (M)**	***p*(EC_{50})**
dCC1_002**	$8.1 \pm 2.6 \times 10^{-7}$	6.3 ± 0.1

Values represent mean ± s.e.m., n=3 biological replicates (dCX1_002, dCC1_005, dCC1_042), n=4 biological replicates (dCX1_001, dCX1_003, dOX1_003), n=6 biological replicates (dCC1_002) and mean, n=2 biological replicates (dCX1_004, dCX1_005 and dCX1_001_maxibinder). The EC_{50} of the native CXCL12 was $8.8 \pm 0.7 \times 10^{-8}$ (M) (pEC_{50} 7.1 ± 0.1, mean ± s.e.m., n=4 biological replicates). The EC_{50} of the native oxytocin was $1.9 \pm 0.3 \times 10^{-9}$ (M) (pEC_{50} 8.7 ± 0.1, mean ± s.e.m., n=4 biological replicates). The EC_{50} of the native CCL5 was $13.6 \pm 6.7 \times 10^{-9}$ (M) (pEC_{50} 7.9 ± 0.2, mean ± s.e.m., n=6 biological replicates).

*In the β-arrestin-1 recruitment assay, the IC_{50} values for dCC1_005 and dCC1_042 miniproteins were $7.9 \pm 1.6 \times 10^{-7}$ (M) (pIC_{50} 6.1 ± 0.1, mean ± s.e.m., n=3 biological replicates) and $2.9 \pm 0.4 \times 10^{-7}$ (M) (pIC_{50} 6.6 ± 0.1, mean ± s.e.m., n=3 biological replicates), respectively.

**In the cAMP assay, an E_{max} value of dCC1_002 was 101 ± 2 %, mean ± s.e.m., n=6 biological replicates). In the G_{oA} dissociation assay, dCC1_002 displayed an EC_{50} value of $5.6 \pm 1.6 \times 10^{-7}$ (M) (pEC_{50} 6.3 ± 0.1, mean ± s.e.m., n=3 biological replicates).

Supplementary Table 8. Pharmacological data of GIPR and PTH1R binder antagonists.

Ligand	Potency IC_{50} (M)	$p(IC_{50})$
dGP1_015	$2.1 \pm 0.7 \times 10^{-8}$	7.7 ± 0.1
dGP1_032	$4.4 \pm 2.7 \times 10^{-8}$	7.6 ± 0.2
dGP1_033	$2.2 \pm 0.6 \times 10^{-8}$	7.7 ± 0.1
dGP1_035	$7.9 \pm 0.3 \times 10^{-9}$	8.2 ± 0.3
dGP1_040	$1.3 \pm 0.7 \times 10^{-8}$	8.1 ± 0.2
dGP1_043	$4.1 \pm 2.1 \times 10^{-8}$	7.6 ± 0.2
dGP1_046	$3.0 \pm 1.2 \times 10^{-8}$	7.7 ± 0.2
dGP1_055	$1.6 \pm 10 \times 10^{-7}$	7.0 ± 0.3
mGP1_096	$9.3 \pm 3.6 \times 10^{-8}$	7.1 ± 0.2
mPT1_003	$2.8 \pm 1.1 \times 10^{-7}$	6.6 ± 0.2
mPT1_084	$4.5 \pm 2.7 \times 10^{-10}$	8.6 ± 0.3
mPT1_085	$8.1 \pm 2.5 \times 10^{-7}$	6.2 ± 0.2
mPT1_094	$1.7 \pm 0.5 \times 10^{-7}$	6.8 ± 0.2

Values represent mean ± s.e.m., n=3 biological replicates (mPT1 miniproteins), n=4 biological replicates (dGP1 miniproteins). The EC_{50} of the native GIP (1-42) was 2.2×10^{-11} (M) (pEC_{50} 10.7 ± 0.2, mean ± s.e.m., n=4 biological replicates) in HEK293A transiently transfected with wild type GIPR and its EC_{80} was used to generate concentration response curves of antagonists to derive IC_{50} values. The EC_{50} of the native PTH1 was 8.4×10^{-11} (M) (pEC_{50} 10.1, mean of technical replicates from a single biological replicate) in CHO cells stably expressing PTH1R.

Supplementary Table 9. Binding data of PTH1R miniprotein binders.

Analyte	Binding late (RU)	off 30 s (R)	off 300 s (RU)	R_{max} (RU)	Retained binding off 30 s (%)
mPT1_001	280.4	45.8	13.9	783	16
mPT1_003	330	246.9	126	631	75
mPT1_004	132.9	52.6	-21.1	751	40
mPT1_005	73.5	43.7	5.3	637	59
mPT1_006	204	16.5	-5	711	8
mPT1_009	145.1	26.7	7.6	626	18
mPT1_010	126.6	36.8	23.3	640	29
mPT1_013	78	34	22.6	561	44
mPT1_016	65	31.2	10.5	641	48
mPT1_017	274	115.6	46	595	42
mPT1_018	231.7	165.1	95.9	686	71
mPT1_020	80.5	9.4	-7.3	735	12
mPT1_022	333.1	159.4	27.9	677	48
mPT1_023	172.1	93.4	17.7	777	54
mPT1_025	123.3	56	32.1	736	45
mPT1_027	369.9	193.7	85.5	667	52
mPT1_028	162.8	77.7	23.8	773	48
mPT1_030	97.6	43.8	25.1	637	45
mPT1_031	75.8	21.8	5.1	584	29
mPT1_033	166	88.3	27	685	53
mPT1_035	262.7	45.9	14.9	683	17
mPT1_036	289.6	153	61.9	534	53
mPT1_038	138	50.2	19	768	36
mPT1_039	141.4	6.2	-4	647	4
mPT1_042	141.8	39.7	16.6	729	28
mPT1_048	92.2	30.9	10.9	698	34
mPT1_049	342.7	136.9	62.4	728	40
mPT1_050	1345.1	952.9	647.5	748	71
mPT1_051	397.3	169	22	727	43
mPT1_052	99.7	24	-49.8	716	24

mPT1_053	69.7	30.6	-1.5	688	44
mPT1_054	426.8	212.4	86.8	711	50
mPT1_055	124.6	54.5	-4.4	685	44
mPT1_056	231.1	61.8	11.9	746	27
mPT1_057	254.4	72	26.2	610	28
mPT1_058	311.2	162.8	44.4	804	52
mPT1_059	232.2	75.8	40.3	758	33
mPT1_061	162.9	127.5	74.8	763	78
mPT1_064	415	188.4	93.3	795	45
mPT1_067	341.2	102.4	51.5	605	30
mPT1_068	267.3	92.9	25.7	587	35
mPT1_069	141	95.1	30	694	67
mPT1_073	134.6	21.6	10.4	636	16
mPT1_084	381.3	346.8	325.8	680	91
mPT1_085	207.5	180.4	169.6	723	87
mPT1_090	111.7	29.6	4.7	606	26
mPT1_093	177.3	121.3	39.4	702	68
mPT1_094	160.8	119.2	28.9	687	74
mPT1_095	153	57.1	11.2	706	37
mPT1_096	126.1	25.2	-3.8	611	20

PTH1R miniproteins were designed using the MetaGen approach and binding was tested in a single experiment (n=1).

Supplementary Table 10. Pharmacological data of CGRPR binder antagonists.

Ligand	Potency IC_{50} (M)	$p(IC_{50})$
mC1_023	$3.7 \pm 0.2 \times 10^{-8}$	7.4 ± 0.1
mC1_044	$> 1 \times 10^{-6}$	< 6
mC2_022	$4.2 \pm 0.6 \times 10^{-7}$	6.2 ± 0.1
dC1_021	$4.4 \pm 0.4 \times 10^{-7}$	6.4 ± 0.1
dC2_001	$4.4 \pm 0.6 \times 10^{-7}$	6.4 ± 0.1
dC2_007	$1.9 \pm 0.1 \times 10^{-7}$	6.7 ± 0.1
dC2_011	$1.5 \pm 0.6 \times 10^{-6}$	5.9 ± 0.2
dC2_019	$5.9 \pm 1.3 \times 10^{-7}$	6.3 ± 0.1
dC2_026	$3.0 \pm 0.7 \times 10^{-7}$	6.6 ± 0.1
dC2_030	$3.7 \pm 0.8 \times 10^{-8}$	7.3 ± 0.1
dC2_039	$4.0 \pm 1.0 \times 10^{-8}$	7.4 ± 0.1
dC2_042	$1.2 \pm 0.4 \times 10^{-7}$	7.0 ± 0.1
dC2_045	$1.2 \pm 0.3 \times 10^{-7}$	6.9 ± 0.1
dC2_049	$4.5 \pm 0.9 \times 10^{-9}$	8.5 ± 0.1
dC2_050	$1.3 \pm 0.1 \times 10^{-8}$	7.9 ± 0.1
dC2_052	$2.7 \pm 1.0 \times 10^{-7}$	6.7 ± 0.2
dC2_053	$3.3 \pm 0.6 \times 10^{-7}$	6.5 ± 0.1
dC2_055	$2.1 \pm 0.5 \times 10^{-7}$	6.7 ± 0.1
dC2_057	$2.4 \pm 0.7 \times 10^{-7}$	6.7 ± 0.2
dC2_058	$1.8 \pm 0.5 \times 10^{-7}$	6.8 ± 0.1
dC2_063	$3.4 \pm 1.3 \times 10^{-7}$	6.6 ± 0.2

dC2_065	$6.9 \pm 1.2 \times 10^{-7}$	6.2 ± 0.1
dC2_066	$4.2 \pm 1.0 \times 10^{-7}$	6.4 ± 0.1
dC2_067	$1.7 \pm 0.6 \times 10^{-7}$	6.8 ± 0.1

Data are mean ± s.e.m., n=3 biological replicates or n=4 biological replicates (see Source data for exact n values). The EC_{50} of the native CGRP was $1.3 \pm 0.1 \times 10^{-10}$ (M) (pEC_{50} 9.9 ± 0.1 in SK-N-MC and $3.9 \pm 0.9 \times 10^{-11}$ (M) (pEC_{50} 10.4 ± 0.1 in CHO-K1/Cre-Luc/CGRPR.

Supplementary Table 11. Sequences of functional GPCR binders extensively characterized in pharmacological assays.

Design	Receptor	Sequence
mM1_034	MRGPRX1	MPIEELVGRIRFAERAAWFAGLDPVEYTKEYIKEEFSEEEREKLLKA QKEGDPRMTPAQKEALKEL
mM1_060	MRGPRX1	MNEAFERALEEAVRAGMPRERAEYWARKLMLTDPFIKYEDLVKEL KKLA
mM1_068	MRGPRX1	MSFEELAEEALEALKAGDKEKAKKLVEKLWEIAEKDKRHMKYFLFL YPFFELGLK
dNK1_037	NK1R	MTNEELRAKISPRLLERIKKRLGVNEEEAIEIAKLMSEKMFVAPGMSI STMIDTAYKKLKEEKAKA
dNK1_069	NK1R	SEEEKEKIIEEIKKLLEEGKKREAVKLLIEKLGVFVAPGMSVNQLYDI AKNYVKKEEEKREEEKK
dNK1_070	NK1R	EEKKRKILEEIIREHVFVAPGQSLRTIVSLIMEKYKNLSEEEIIAKLKE QNPEAAEEFKKRLEELKKE
mM1_034_F12W _Y27F and	MRGPRX1	MPIEELVGRIRWAERAAWFAGLDPVEFTKEYIKEEFSEEEREKLLK AQKEGDPRMTPAQKEALKEL
mM1_034_F12W _A58M	MRGPRX1	MPIEELVGRIRWAERAAWFAGLDPVEYTKEYIKEEFSEEEREKLLK AQKEGDPRMTPMQKEALKEL
dCX1_001	CXCR4	MVLKAVSMPTGIYSKLKKEYGEEIEKKAKELGVKISYGYRNGEMLIG FSGKKEEVDKLVKYVKKIVTEISRKRN
dCX1_002	CXCR4	MVLKSVAAYTGVFTELMKKYGEEIKKRAKELGVKLSYGYRNGLRLL GFSGEEEKVNELVEYVKKLVTEVSRERN
dCX1_001_maxi binder	CXCR4	MVLKAVSMPTGIYSKLKKGAGKKIEEKAKELGVKISYGYRNGEMLIG FSGKKVEVDLLVNMVKAIVELIEQGMSAEEAYKKAEEAAKEIVEAAG GDEKLIAEACEIVKKLVKEGKSAYEAMKEAAEKVKAKVEASGGK
dOX1_003	OXTR	KEELLARVLARLEERFASNAYLTEIAKAVARDVFAGNKRITVPARRN PLTDAALAGNALLVVKKLIAEEEAKR
dOX2_003	OXTR	DEEIREKVKEEVTKRFADEPYLREIALNVVEAIFSGSPTVIVPARRHP LVDASLAGGMLLYVTKLIEEAKAES
dGl1_024	GLP1R	MAELKETINKLPPEYREKLERLLERYYIGAKIHPAFGVAGSIAIEEFA ATLPPELQKVAREALAHVNKLIAEE
mGl1_008	GLP1R	MLSTRDILYAHIATREVSAAYGIDPDSPKAQAILEALLEAAREGVKRF DELLDIAEEMAAQ
dGP1_035	GIPR	GEKEKLRKEALEKAKELGLDVESFYKAAVALGTIEAVLGAIIYYKLIK DPSISPEELKILLKVLEAIEKRLKAQ
dGP1_040	GIPR	AEREEILARAEEVVASVTEEQLTELALNARTLEEYVGALLIYRAKFD PSVTVAELVDENPEAVAAGVELAEKTLG

mPT1_084	PTH1R	MEKEIEELMKTFGVKREDIEAGLDAGAKNMAEIVALLKAWGDISDE TFVEALHWLKK
mPT1_094	PTH1R	SILDEFNEIKEKLDAGEATDEEVYEAVVLAIEAAKKGEISGEEAEELL QYVSGTHQAHTS
dC2_049	CGRPR	DTNFELGVEYFMLGLQALVHGDYDNAIKYFNKAIEYFKKSSDKEKA AKYIALAQKYIDEAKKLKAEKEA
dC2_050	CGRPR	NDNDELAVQYYMDGLLAYVHGDYEGAIKYFNKAIEYAKKGTNEKV RTSVISNSKKYIEEAKKLLAEKEA
mC1_023	CGRPR	QELEVRENARFVYQTLHYLGPLPLEKLKKILGLTDEQLEAALEYLKK LGRIKIEETPEKKVVSLV
mC2_022	CGRPR	EEEEAMEELLAAKGDCEKMAEALARVLEVGDVGTQRLAYLYVHYT HPECSAKADEVVAKHY
mC2_022-Fc9	CGRPR	MARAWIFFLLCLAGRALAEEEEAMEELLAAKGDCEKMAEALARVLE VGDVGTQRLAYLYVHYTHPECSAKADEVVAKHYGGSGSGGSGSG SGGSEPKSSDKTHTCPPCPAPELLGGPSVFLFPPKPKDTLMISRTP EVTCVVVDVSHEDPEVKFNWYVDGVEVHNAKTKPREEQYNSTYR VVSVLTVLHQDWLNGKEYKCKVSNKALPAPIEKTISKAKGQPREPQ VYTLPPSRDELTKNQVSLTCLVKGFYPSDIAVEWESNGQPENNYK TTPPVLDSDGSFFLYSKLTVDKSRWQQGNVFSCSVMHEALHNHYT QKSLSLSPGK

MRGPRX1 = Mas-related G protein-coupled receptor 1
NK1R = Neurokinin 1 receptor
CXCR4 = C-X-C chemokine receptor type 4
OXTR = oxytocin receptor
GLP1R = glucagon-like peptide 1 receptor
GIPR = gastric inhibitory polypeptide receptor
PTH1R = parathyroid hormone 1 receptor
CGRPR = calcitonin gene-related peptide receptor

References

1. van Kempen, M., Kim, S.S., Tumescheit, C. *et al.* Fast and accurate protein structure search with Foldseek. *Nat. Biotechnol.* 42, 243–246 (2024).
2. Olsen, R. H. J. *et al.* TRUPATH, an open-source biosensor platform for interrogating the GPCR transducerome. *Nat. Chem. Biol.* **16**, 841–849 (2020).
3. Gillis, A. *et al.* Low intrinsic efficacy for G protein activation can explain the improved side effect profiles of new opioid agonists. Sci. Signal. eaaz3140, 1-18 (2020).
4. Muratspahić, E. *et al.* Design and structural validation of peptide–drug conjugate ligands of the kappa-opioid receptor. *Nat. Commun.* **14**, 8064 (2023).
5. Agirre, J. *et al.* The CCP4 suite: integrative software for macromolecular crystallography. *Acta Crystallogr. Sect. Struct. Biol.* **79**, 449–461 (2023).